

DEVELOPMENT OF HIGH FRACTURE TOUGHNESS HARD COATINGS

A THESIS SUBMITTED TO  
THE GRADUATE SCHOOL OF NATURAL AND APPLIED SCIENCES  
OF  
MIDDLE EAST TECHNICAL UNIVERSITY

BY

BURÇİN KAYGUSUZ

IN PARTIAL FULFILLMENT OF THE REQUIREMENTS  
FOR  
THE DEGREE OF DOCTOR OF PHILOSOPHY  
IN  
MICRO AND NANOTECHNOLOGY

SEPTEMBER 2021



Approval of the thesis:

**DEVELOPMENT OF HIGH FRACTURE TOUGHNESS HARD COATINGS**

submitted by **BURÇİN KAYGUSUZ** in partial fulfillment of the requirements for the degree of **Doctor of Philosophy in Micro and Nanotechnology, Middle East Technical University** by,

Prof. Dr. Halil Kalıpçılar  
Dean, Graduate School of **Natural and Applied Sciences**

Prof. Dr. Almıla Güvenç Yazıcıoğlu  
Head of the Department, **Micro and Nanotechnology**

Assoc. Prof. Dr. Sezer Özerinç  
Supervisor, **Micro and Nanotechnology, METU**

Prof. Dr. M. Kürşat Kazmanlı  
Co-Supervisor, **Metallurgical and Materials Eng., İTÜ**

**Examining Committee Members:**

Assoc. Prof. Dr. Yiğit Karpat  
Industrial Engineering, Bilkent University

Assoc. Prof. Dr. Sezer Özerinç  
Micro and Nanotechnology, METU

Assoc. Prof. Dr. Ender Yıldırım  
Mechanical Engineering, METU

Assist. Prof. Dr. Orkun Özşahin  
Mechanical Engineering, METU

Assist. Prof. Dr. Erkan Konca  
Metallurgical and Materials Engineering, Atılım University

Date: 02.09.2021

**I hereby declare that all information in this document has been obtained and presented in accordance with academic rules and ethical conduct. I also declare that, as required by these rules and conduct, I have fully cited and referenced all material and results that are not original to this work.**

Name Last name : Burçin Kaygusuz

Signature :

## **ABSTRACT**

### **DEVELOPMENT OF HIGH FRACTURE TOUGHNESS HARD COATINGS**

Kaygusuz, Burçin  
Doctor of Philosophy, Micro and Nanotechnology  
Supervisor : Assoc. Prof. Dr. Sezer Özerinç  
Co-Supervisor: Prof. Dr. M. Kürşat Kazmanlı

September 2021, 124 pages

Improving the machining performance of cutting tools is critical for increasing product quality and decreasing production cost and time. For this purpose, hard coatings on cutting tools are widely utilized in the industry. These hard coatings increase the lifetime of cutting tools by improving their wear resistance and allow higher cutting speeds. One of the primary drawbacks of these hard coatings is their brittle nature, which occasionally results in premature failure. This thesis investigated a solution to this problem through the development of new generation hard coatings. For this purpose, W and Mo alloying additions were made to conventional coating compositions such as AlTiN and AlCrN, based on the predictions of density functional theory calculations (DFT). The thesis study considered two different coating methods: magnetron sputtering (MS), suitable for lab-scale studies, and cathodic arc evaporation (CAE), suitable for industrial purposes. X-ray Diffraction, Scanning Electron Microscopy, and Energy Dispersive X-ray Spectroscopy characterized the coatings and nanoindentation measurements provided the hardness and fracture toughness values. In addition, new generation fracture toughness measurements based on microcantilever bending tests were employed for more accurate quantification of the fracture behavior. Lastly, selected coatings were subjected to drilling and ball-on disc tests to clarify their performance

in actual working conditions. The results show that especially W additions provide at least an order of magnitude increase in fracture toughness combined with dramatic increases in tool lifetime. Therefore, the thesis results demonstrated an effective route to the development of new high-performance coatings for wear resistance applications. Future studies on optimizing the process parameters for cathodic arc evaporation will enable the wider utilization of the developed coatings in industry.

Keywords: Hard coatings, Fracture toughness, Wear resistance, Nanoindentation, Cutting tools

## ÖZ

### YÜKSEK KIRILMA TOKLUĞUNA SAHİP SERT KAPLAMALARIN GELİŞTİRİLMESİ

Kaygusuz, Burçin  
Doktora, Mikro ve Nanoteknoloji  
Tez Danışmanı: Doç. Dr. Sezer Özerinç  
Ortak Tez Danışmanı: Prof. Dr. M. Kürşat Kazmanlı

Eylül 2021, 124 sayfa

Talaşlı imalatta kullanılan kesici uçların metal işleme performanslarını artırmak, ürün kalitesini yükseltmek ve üretim maliyetlerini ve sürelerini düşürmek açısından büyük önem taşır. Bu amaçla kesici uçların üzerine sert kaplama uygulaması endüstride sıklıkla kullanılır. Bu kaplamalar hem aşınma dayanımını artırarak kesici uçların ömrünü uzatır hem de daha yüksek hızda ve kuru işlemeye olanak tanır. Mevcut sert kaplamaların önemli bir dezavantajı kırılma olmaları ve buna bağlı performans sorunlarıdır. Bu tez çalışması, bu sorunun üstesinden gelebilmek için, AlTiN ve AlCrN gibi geleneksel kaplamalara alaşım eklemeleri yapılması fikrini deneysel olarak araştırmıştır. Literatürdeki yoğunluk fonksiyonel teori (YFT) hesaplamaları ışığında bu amaca yönelik en uygun elementler olarak W ve Mo denenmiştir. Kaplama işlemi için laboratuvar ölçeğindeki çalışmalara uygun olan magnetron saçırma (MS) ve endüstriyel ölçekteki uygulamalara yönelik katodik ark buharlaştırma (KAB) yöntemleri uygulanmıştır. Üretilen kaplamaların karakterizasyonu X-ışınları kırınımı ve taramalı elektron mikroskobu gibi yöntemlerle gerçekleştirilmiş, sertlik ve kırılma tokluğu değerleri ise nanosertlik ölçümleri ile tespit edilmiştir. Ayrıca mikrokiriş eğme yöntemini baz alan yeni nesil mikrokırılma ölçümleri de gerçekleştirilerek kırılma davranışı ile alakalı daha detaylı bilgiler elde edilmiştir. Son olarak delme deneyleri ve aşınma deneyleri aracılığıyla

kaplamaların gerek alıřma kořullarındaki performansı incelenmiřtir. zellikle W alařım eklemeleri ile 10 katı ařan kırılma tokluęu artıřı ve buna baęlı olarak ilgili kesici takımlarda nemli oranda mr artıřı saęladıęı ortaya konmuřtur. Dolayısıyla tez kapsamında gerekleřtirilen refrakter element eklemelerinin, yeni nesil yksek performanslı kaplamaların geliřtirilmesi iin etkili bir yaklařım olduęu kanıtlanmıřtır. Gelecekteki endstriyel lekteki kaplama parametrelerin optimizasyonu alıřmaları aracılıęıyla, bu yeni nesil kaplamaların yaygın olarak kullanılması mmkn hale gelecektir.

Anahtar Kelimeler: Sert kaplamalar, Kırılma tokluęu, Ařınma dayanımı, Nanosertlik lmleri, Kesici takımlar ve ular



Dedicated to my family

## ACKNOWLEDGMENTS

This thesis would not be possible without the support of many people in my life. It was quite an enjoyable and memorable experience that I worked with nice and intelligent people. Thus, I take this chance to acknowledge each of them who have helped and supported me in this study.

I would like to express my gratitude to my supervisor, Assoc. Prof. Dr. Sezer Özerinç for his guidance, advice, support, encouragement, and valuable suggestions throughout the studies.

Secondly, I would like to thank my co-advisor, Prof. Dr. M.Kürşat Kazmanlı, for his guidance and experience-sharing, especially in the tribology studies and characterization of worn specimens.

I am grateful to Servet Şehirli and Yusuf Yıldırım for sharing their experiences, thoughts, and advice. Thanks to all my friends in the Nanomechanics Laboratory at the Department of Mechanical Engineering, METU, especially Mehmet Kepenekci, Roozbeh Neshani, and Ali Bagheri Behboud friendship and helpful discussions on the experiments of the thesis. Additionally, I am grateful to Can Okuyucu and Büşra Yartaşı for their help and support.

I would like to thank Dr. Amir Motallebzadeh for helping me do some of the experiments. I am also grateful to METU Central Laboratory staff and Bilkent UNAM staff for their technical help.

I would like to thank S.Serdar Özbay, Erkan Kaçar and İ. Göksel Hızlı to help for magnetron sputtering, wear tests and some characterization in İTU.

Finally, I would like to thank all my family members, especially my elder brothers Yasin and Yalçın, for their endless support, encouragement, motivation, and advice. Without my family, this thesis would not have been possible.

This work is funded by The Scientific and Technological Research Council of Turkey (TÜBİTAK) through an ARDEB 1001 project under grant #118M201 and Council of Higher Education (YÖK) through the 100/2000 priority fields doctoral scholarship.

## TABLE OF CONTENTS

ABSTRACT.....	v
ÖZ.....	vii
ACKNOWLEDGMENTS.....	x
TABLE OF CONTENTS.....	xi
LIST OF TABLES.....	xiv
LIST OF FIGURES.....	xv
LIST OF ABBREVIATIONS.....	xx
LIST OF SYMBOLS.....	xxi
CHAPTERS	
1 INTRODUCTION.....	1
1.1 Metal Nitride Hard Coatings.....	2
1.2 Production of Hard Coatings.....	5
1.3 Mechanical Characterization Techniques.....	7
1.3.1 Nanoindentation.....	7
1.3.2 Micro and Nanoscratch Testing.....	10
1.3.3 Microcantilever Bending.....	11
1.4 Wear Measurements.....	13
2 MAGNETRON-SPUTTERED COATINGS.....	17
2.1 Experimental Details.....	17
2.1.1 Sample Preparation.....	17
2.1.2 Microstructural Characterization.....	21
2.1.2.1 X-ray Diffraction (XRD).....	21

2.1.2.2	Scanning Electron Microscopy (SEM) & Energy Dispersive X-ray Spectroscopy (EDS) .....	22
2.1.2.3	Wavelength Dispersive Spectroscopy (WDS) .....	24
2.1.2.4	X-ray Photoelectron Spectroscopy (XPS).....	24
2.1.3	Mechanical Characterization .....	25
2.1.3.1	Nanoindentation .....	25
2.1.3.2	Fracture Toughness Measurement .....	25
2.2	Results and Discussion .....	26
2.2.1	Microstructure .....	26
2.2.2	Mechanical Characterization .....	33
2.3	Conclusions .....	45
3	CATHODIC ARC EVAPORATED COATINGS .....	47
3.1	Experimental Details .....	47
3.1.1	Sample Preparation.....	47
3.1.2	Microstructural Characterization.....	51
3.1.2.1	X-ray Diffraction (XRD).....	51
3.1.2.2	Scanning Electron Microscopy (SEM) & Energy Dispersive X-ray Spectroscopy (EDS) .....	51
3.1.2.3	X-ray Photoelectron Spectroscopy (XPS).....	52
3.1.3	Mechanical Characterization .....	52
3.1.3.1	Nanoindentation .....	52
3.1.3.2	Microcantilever Bending.....	53
3.1.3.2.1	Chemical Etching.....	55
3.1.3.2.2	Fabrication of Microcantilevers.....	57

3.1.3.3	Ball-on Disc Test .....	62
3.1.3.4	Drilling Tests .....	64
3.2	Results and Discussion .....	65
3.2.1	Microstructure .....	65
3.2.2	Mechanical Characterization .....	79
3.3	Conclusions .....	108
4	CONCLUSIONS AND FUTURE WORK .....	111
5	REFERENCES .....	113
	CURRICULUM VITAE .....	123

## LIST OF TABLES

### TABLES

Table 1. Characteristics of popular hard coatings. ....	4
Table 2. Coating parameters for magnetron sputtering. ....	19
Table 3. Details of samples produced by magnetron sputtering. (Ref. means reference sample (without W)). ....	20
Table 4. The calculated grain size of the magnetron sputtered samples. ....	30
Table 5. EDS and WDS results of the magnetron sputtered samples. ....	31
Table 6. Summary of mechanical properties of samples after nanoindentation.....	38
Table 7. Fracture toughness measurement results for all specimens.....	45
Table 8. Sample details of routine hard coatings by Ionbond Turkey.....	48
Table 9. Experimental details for nonroutine hard coatings.....	50
Table 10. Experimental details of the etching procedure. ....	56
Table 11. Details of produced micro-cantilevers. ....	59
Table 12. Details of the ball-on-disc test.....	63
Table 13. Calculated grain size values of routine hard coatings. ....	71
Table 14. Calculated crystalline size of nonroutine hard coatings.....	72
Table 15. EDS results of routine hard coatings.....	76
Table 16. EDS result of nonroutine hard coatings. ....	77
Table 17. XPS results of selected MS and CAE hard coatings. (MS: 5050-ref., CAE: Al <sub>50</sub> Ti <sub>50</sub> samples). ....	79
Table 18. Summary of mechanical evaluation of routine hard coatings. ....	80
Table 19. Nanoindentation results for all nonroutine Ionbond Samples. ....	81
Table 20. Calculated fracture toughness for routine hard coatings. ....	82
Table 21. Calculated fracture toughness of nonroutine hard coatings. ....	85
Table 22. Micro-cantilever bending results.....	89
Table 23. Comparison of calculated fracture toughness using two different methods.....	89
Table 24. The friction coefficient of nonroutine coatings. ....	93

## LIST OF FIGURES

### FIGURES

Figure 1. G/B and $C_{12}$ - $C_{44}$ values of different coatings (Sangiovanni et al., 2012)..	3
Figure 2. Schematic drawing of magnetron sputtering (Abboud, 2018). .....	6
Figure 3. Schematic view of cathodic arc evaporation technique.....	7
Figure 4. The schematic of a load-displacement curve of Nanoindentation (Abboud, 2018). .....	8
Figure 5. SEM image of cracks after nanoindentation.....	10
Figure 6. SEM image and schematic of scratch tested surface of a specimen (Nanomechanical Instruments for SEM/TEM, n.d.).....	11
Figure 7. Schematic representation of the micro-cantilever bending geometry (Sebastiani et al., 2015).....	12
Figure 8. The load-displacement curve for Si wafer (Maio & Roberts, 2005).....	12
Figure 9. Schematic of the pin on and ball on disc tests (Tribonet, 2019). .....	14
Figure 10. Wear mechanism according to cutting speed, b) types of wear mechanism (Bouzakis et al., 2012b). .....	15
Figure 11. Vaksis Magnetron Sputterer in ODTÜ and in-house manufactured Magnetron Sputterer in İTU.....	18
Figure 12. Samples for first magnetron sputtering trials. $Al_{67}Ti_{33}N$ on SS substrate (left) and $Al_{50}Ti_{50}N$ on Si(100) substrate (right).....	19
Figure 13. The interaction between the incident electron beam and the surface of the sample (Goldstein et al., 1992). .....	23
Figure 14. XRD results of $Al_{50}Ti_{50}$ based specimens. 5050-ref. means $Al_{50}Ti_{50}N$ (without W), 5050-1, 5050-2, and 5050-3 are $(Al_{50}Ti_{50})WN$ with different W amounts. ....	27
Figure 15. XRD results of AlCr based specimens. AlCr-ref. means without W, AlCr-1, and AlCr-2 are $(Al_{50}Cr_{50})WN$ which have different W amounts.....	28
Figure 16. XRD results of $Al_{67}Ti_{33}$ based specimens. 6733-ref. means $Al_{67}Ti_{33}N$ (without W), 6733-1, and 6733-2 are $(Al_{67}Ti_{33})WN$ with different W amounts. ...	29

Figure 17. SEM images of a) surface b) cross-section view of 5050-ref. sample, c) surfaced) cross-section view of 6733-ref. sample, e) surface f) cross-section view of AlCr-ref. sample.....	32
Figure 18. SEM images of a) AlCr-ref, b) AlCr-2 samples. ....	33
Figure 19. a) Load-displacement, (b) Hardness-depth, (c)Elastic modulus-depth curves of 5050-ref. sample. ....	35
Figure 20. a) H and E vs. W amount and b) H/E and H3/E2 vs. W amount for Al <sub>50</sub> Ti <sub>50</sub> based coatings. (data for 5050-ref., 5050-1, 5050-2, and 5050-3, respectively.)....	39
Figure 21. a) H and E vs. W amount, and b) H/E and H3/E2 vs. W amount for Al <sub>67</sub> Ti <sub>33</sub> based coatings (data for 6733-ref., 6733-1, and 6733-2, respectively). ....	40
Figure 22. a) H and E vs. W amount and b) H/E and H3/E2 vs. W amount for Al <sub>50</sub> Cr <sub>50</sub> based coatings. (data for AlCr-ref., AlCr-1 and AlCr-2, respectively.) .....	40
Figure 23. An example of crack size measurements (in μm) for Al <sub>50</sub> Ti <sub>50</sub> based sample and a representative SEM image.....	41
Figure 24. SEM images of a) 5050-ref, 5050-1, 5050-3, b)6733-ref, 6733-1, 6733-2, c) AlCr-ref, AlCr-1, AlCr-2 (from left to right) after nanoindentation. ....	42
Figure 25. a) The load-displacement curve for 6733-1 sample, b) zoomed region to show pop-out parts in the load-displacement curve. ....	44
Figure 26. Photograph of a) Hauzer RTC 850 Cathodic arc evaporation systems and b) TiAlW alloy cathodes. ....	49
Figure 27. Selected samples with different geometries for fracture toughness testing at the small scale: (a) single cantilever bending, (b) clamped beam bending, (c) Double Cantilever bending, and (d) pillar splitting. All samples were prepared with FIB on Si(100) (Jaya et al., 2015). e)Schematic representation of the micro-cantilever bending geometry (Lawn et al., 1980).....	54
Figure 28. The schematic representation of the chemical etching procedure. ....	55
Figure 29. SEM image of coated Si (100) substrate to see free-standing areas after chemical etching. (Al <sub>50</sub> Ti <sub>50</sub> )N hard coating produced by cathodic arc evaporation was used.....	56



Figure 30. (a) A photograph of the focused ion beam located in Bilkent University-UNAM. (b) Schematic description of the FIB milling process. ....	57
Figure 31. An SEM image of the microcantilever after FIB milling. ....	58
Figure 32. SEM images of prepared microcantilevers using FIB milling. ....	60
Figure 33. Schematic representation of beam bending (Beam Deflection Formulas, n.d.). ....	61
Figure 34. Produced HSS a) pins and b) discs for tribology tests. ....	63
Figure 35. a) Vertical machining center, b) image and properties of AISI 4140 Steel during the test. ....	65
Figure 36. XRD results of AlTi based routine hard coatings. ....	66
Figure 37. XRD results of AlCr based routine hard coatings. ....	67
Figure 38. Example XRD data from the literature (Fan et al., 2017; Joo et al., 2009). ....	67
Figure 39. XRD Results of W- added AlTi based hard coatings. ....	68
Figure 40. XRD patterns of Mo-added AlTi based hard coatings. ....	69
Figure 41. XRD results of Mo-added AlCr based hard coatings. ....	69
Figure 42. An example XRD pattern and strain-size plot for Al <sub>50</sub> Ti <sub>50</sub> -W-1 sample. ....	71
Figure 43. Cross-section SEM images of a) Al <sub>50</sub> Ti <sub>50</sub> , b) maxAl <sub>50</sub> Ti <sub>50</sub> , c) maxAl <sub>67</sub> Ti <sub>33</sub> and d) Al <sub>64</sub> Cr <sub>36</sub> routine hard coatings. ....	73
Figure 44. Surface SEM images of a) Al <sub>50</sub> Ti <sub>50</sub> , b) maxAl <sub>50</sub> Ti <sub>50</sub> , c) maxAl <sub>67</sub> Ti <sub>33</sub> and d) Al <sub>64</sub> Cr <sub>36</sub> routine hard coatings. ....	74
Figure 45. SEM images of nonroutine hard coatings. a) Al <sub>50</sub> Ti <sub>50</sub> , b) Al <sub>50</sub> Ti <sub>50</sub> -W-1, c) Al <sub>50</sub> Ti <sub>50</sub> -W-2, d) Al <sub>67</sub> Ti <sub>33</sub> , e) Al <sub>67</sub> Ti <sub>33</sub> -Mo-1, f) Al <sub>67</sub> Ti <sub>33</sub> -Mo-2, g) Al <sub>64</sub> Cr <sub>36</sub> , h) Al <sub>64</sub> Cr <sub>36</sub> -Mo-1. ....	75
Figure 46. XPS results of a) Al <sub>50</sub> Ti <sub>50</sub> routine (cathodic arc evaporation) and b) 5050-ref. (magnetron sputtering) samples. Both of them have (Al <sub>50</sub> Ti <sub>50</sub> )N composition. ....	78
Figure 47. SEM images of routine hard coatings after nanoindentation. a) Al <sub>50</sub> Ti <sub>50</sub> , b) maxAl <sub>50</sub> Ti <sub>50</sub> , c) Al <sub>67</sub> Ti <sub>33</sub> , d) maxAl <sub>67</sub> Ti <sub>33</sub> , e) Al <sub>50</sub> Cr <sub>50</sub> , e) Al <sub>64</sub> Cr <sub>36</sub> . ....	83

Figure 48. SEM images after cube corner nanoindentation a) Al <sub>67</sub> Ti <sub>33</sub> , b) Al <sub>64</sub> Cr <sub>36</sub> , c) Al <sub>50</sub> Ti <sub>50</sub> -W-1, d) Al <sub>50</sub> Ti <sub>50</sub> -W-2, e) Al <sub>67</sub> Ti <sub>33</sub> -Mo-1, f) Al <sub>67</sub> Ti <sub>33</sub> -Mo-2.....	84
Figure 49. a) K <sub>IC</sub> vs. at.% W and b) K <sub>IC</sub> vs. at.% Mo.....	86
Figure 50. The load-displacement curve of cantilever no.1. ....	87
Figure 51. Load-Displacement measurement and prediction of linear elastic displacement equation for Cantilever No.1 .....	88
Figure 52. SEM images of example fracture surfaces after cantilever bending test. ....	90
Figure 53. The friction coefficient of a) Al <sub>67</sub> Ti <sub>33</sub> , b) Al <sub>64</sub> Cr <sub>36</sub> , c) Al <sub>50</sub> Ti <sub>50</sub> W-1, d) Al <sub>50</sub> Ti <sub>50</sub> -W-2, e) Al <sub>67</sub> Ti <sub>33</sub> Mo-1, f) Al <sub>64</sub> Cr <sub>36</sub> Mo-1 against 440C SS ball.....	91
Figure 54. The Friction coefficient of a) Al <sub>67</sub> Ti <sub>33</sub> , b) Al <sub>64</sub> Cr <sub>36</sub> , c) Al <sub>50</sub> Ti <sub>50</sub> W-1, d) Al <sub>50</sub> Ti <sub>50</sub> -W-2, e) Al <sub>67</sub> Ti <sub>33</sub> Mo-1, f) Al <sub>64</sub> Cr <sub>36</sub> Mo-2 against Alumina ball.....	92
Figure 55. Wear ratio of samples. ....	94
Figure 56. Analysis of uncoated disc after test: a) 3D profile against Al <sub>2</sub> O <sub>3</sub> balls, b) 3D profile against 440C SS balls, c) 2D profile against Al <sub>2</sub> O <sub>3</sub> balls, d) 2D profile against 440C SS balls, e) SEM images of uncoated discs against Al <sub>2</sub> O <sub>3</sub> balls. f) SEM images of uncoated discs against 440C SS balls. ....	95
Figure 57. Analysis of Al <sub>67</sub> Ti <sub>33</sub> coated disc after test: a) 3D profile against Al <sub>2</sub> O <sub>3</sub> balls, b) 3D profile against 440C SS balls, c) 2D profile against Al <sub>2</sub> O <sub>3</sub> balls, d) 2D profile against 440C SS balls, e) SEM images of Al <sub>67</sub> Ti <sub>33</sub> coated discs against Al <sub>2</sub> O <sub>3</sub> balls. f) SEM images of Al <sub>67</sub> Ti <sub>33</sub> coated discs against 440C SS balls.....	96
Figure 58. Analysis of Al <sub>64</sub> Cr <sub>36</sub> coated disc after test: a) 3D profile against Al <sub>2</sub> O <sub>3</sub> balls, b) 3D profile against 440C SS balls, c) 2D profile against Al <sub>2</sub> O <sub>3</sub> balls, d) 2D profile against 440C SS balls, e) SEM images of Al <sub>64</sub> Cr <sub>36</sub> coated discs against Al <sub>2</sub> O <sub>3</sub> balls. f) SEM images of Al <sub>64</sub> Cr <sub>36</sub> coated discs against 440C SS balls.....	97
Figure 59. Analysis of Al <sub>50</sub> Ti <sub>50</sub> -W-1 coated disc after test: a) 3D profile against Al <sub>2</sub> O <sub>3</sub> balls, b) 3D profile against 440C SS balls, c) 2D profile against Al <sub>2</sub> O <sub>3</sub> balls, d) 2D profile against 440C SS balls, e) SEM images of Al <sub>50</sub> Ti <sub>50</sub> -W-1 coated discs against Al <sub>2</sub> O <sub>3</sub> balls. f) SEM images of Al <sub>50</sub> Ti <sub>50</sub> -W-1 coated discs against 440C SS balls.....	98

Figure 60. Analysis of Al<sub>50</sub>Ti<sub>50</sub>-W-2 coated disc after test: a) 3D profile against Al<sub>2</sub>O<sub>3</sub> balls, b) 3D profile against 440C SS balls, c) 2D profile against Al<sub>2</sub>O<sub>3</sub> balls, d) 2D profile against 440C SS balls, e) SEM images of Al<sub>50</sub>Ti<sub>50</sub>-W-2 coated discs against Al<sub>2</sub>O<sub>3</sub> balls. f) SEM images of Al<sub>50</sub>Ti<sub>50</sub>-W-2 coated discs against 440C SS balls. .... 99

Figure 61. Analysis of Al<sub>67</sub>Ti<sub>33</sub>-Mo-1 coated disc after test. a) 3D profile against Al<sub>2</sub>O<sub>3</sub> balls, b) 3D profile against 440C SS balls, c) 2D profile against Al<sub>2</sub>O<sub>3</sub> balls, d) 2D profile against 440C SS balls, e) SEM images of Al<sub>67</sub>Ti<sub>33</sub>-Mo-1 coated discs against Al<sub>2</sub>O<sub>3</sub> balls. f) SEM images of Al<sub>67</sub>Ti<sub>33</sub>-Mo-1 coated discs against 440C SS balls. .... 100

Figure 62. Analysis of Al<sub>64</sub>Cr<sub>36</sub>-Mo-1 coated disc after test: a) 3D profile against Al<sub>2</sub>O<sub>3</sub> balls, b) 3D profile against 440C SS balls, c) 2D profile against Al<sub>2</sub>O<sub>3</sub> balls, d) 2D profile against 440C SS balls, e) SEM images of Al<sub>64</sub>Cr<sub>36</sub>-Mo-1 1 coated discs against Al<sub>2</sub>O<sub>3</sub> balls. f) SEM images of Al<sub>64</sub>Cr<sub>36</sub>-Mo-1 coated discs against 440C SS balls. .... 101

Figure 63. High resolution macro-objective images of a) Al<sub>67</sub>Ti<sub>33</sub>, b) Al<sub>64</sub>Cr<sub>36</sub>, c) Al<sub>50</sub>Ti<sub>50</sub>W-1, d) Al<sub>50</sub>Ti<sub>50</sub>W-2, e) Al<sub>67</sub>Ti<sub>33</sub>-Mo-1, f) Al<sub>64</sub>Cr<sub>36</sub>-Mo-1, g) Al<sub>67</sub>Ti<sub>33</sub>-Mo-2, and h) Al<sub>64</sub>Cr<sub>36</sub>-Mo-2. .... 103

Figure 64. The number of drilled holes before failure for each coating scenario. 104

Figure 65. Dimension of cutting tool, test details, and workpiece material after the test. .... 105

Figure 66. SEM and EDS analyzes of Al<sub>50</sub>Ti<sub>50</sub>-W-2 coated cutting tools after opening of 100 holes. .... 107

Figure 67. SEM images of coated cutting tools after 100 holes a) Al<sub>67</sub>Ti<sub>33</sub>-Mo-1, b) Al<sub>64</sub>Cr<sub>36</sub>-Mo-1, c) Al<sub>67</sub>Ti<sub>33</sub>-Mo-2, and d) Al<sub>64</sub>Cr<sub>36</sub>-Mo-2. .... 108

## LIST OF ABBREVIATIONS

### ABBREVIATIONS

BSE	Back Scattered Electron
CAE	Cathodic Arc Evaporation
CSM	Continous Stiffness Measurement
CVD	Chemical Vapor Deposition
DFT	Density Functional Theory
DLF	Differential Load Feed
EDS	Energy-Dispersive X-Ray Spectroscopy
FIB	Focused Ion Beam
FWHM	Full width half maximum
KOH	Potassium Hydroxide
HF	Hydrofluoric Acid
MS	Magnetron Sputtering
PVD	Physical Vapor Deposition
SEM	Scanning Electron Microscopy
SE	Secondary Electron
TMAH	Tetramethylammonium hydroxide
404C SS	Stainless Steel
WDS	Wavelength-Dispersive X-Ray Spectroscopy
XRD	X-ray Diffraction
XPS	X-ray Photoelectron Spectroscopy

## LIST OF SYMBOLS

### SYMBOLS

$G/B$	ratio of shear modulus to bulk modulus
$C_{12}-C_{44}$	cauchy pressure
$\sigma_y$	yield strength
$\sigma_0$	the yield strength of a single crystal structure
$D$	grain size
$P$	load
$H$	hardness
$E$	elastic modulus
$H/E$	plasticity index
$H^3/E^2$	resistance against the plastic deformation
$A_p$	projected area
$d$	spacing between planes
$\lambda$	wavelength of the incident x-ray beam
$\Theta$	angle between the atomic planes and incident X-ray beam
$n_d$	diffraction order
$hkl$	crystalline plane
$B$	peak width
$n$	integer known
$L$	crystalline size
$K$	shape factor

$h$	total displacement
$h_c$	contact depth
$h_s$	displacement of the contact perimeter
Lc	critical load
$S$	stiffness

## CHAPTER 1

### INTRODUCTION

Metal cutting machining or metal machining is one of the important methods in the manufacturing industries to shape a particular product. Turning, milling, drilling, and grinding are the most common traditional machining processes. In these techniques, cutting tools are used to shape and produce the components. Product quality, production time, and cost are important parameters for the machining industry in the world and our country. To improve the mentioned properties of the cutting tools, a hard coating is frequently used in the machining industry. These hard coatings increase the lifetime of cutting tools by improving their wear resistance and allowing higher speed dry cutting. Therefore, the development of higher performance insert coatings is of paramount importance in terms of both production economy and environmental impact.

One of the main disadvantages of metal nitride hard coatings is their brittle nature. The low ductility increases the likelihood of crack formation and subsequent failure. Coatings need to possess high fracture toughness to minimize this problem. Recent density functional theory calculations show that refractory element additions (such as W, Mo, Nb, Zr, Ta) to hard coatings dramatically improve the fracture toughness of the coatings (Leyland & Matthews, 2000). This theoretical prediction needs experimental investigation for the potential application of the alloying additions for industrial use. However, as far as we know, there is no significant systematic study to date in the literature that investigates the effect of these alloying additions on fracture toughness. Especially experimental investigations of fracture toughness of the W and Mo added AlTiN and AlCrN had not been studied in the literature.

In the proposed project, refractory elements were added to widely utilized coatings such as AlTiN and CrAlN. The effect of these additions on the mechanical

properties, wear resistance, and machining performance was investigated with a special emphasis on fracture toughness. W and Mo additions are the main focus of the study as density functional theory calculations suggest that W and Mo are the most effective element addition for improving the toughness. First, reactive Magnetron sputtering at a laboratory scale system was utilized to prepare various coatings. These coatings were analyzed in detail, and then an industrial scale cathodic arc deposition system was used to get hard coatings. This allowed the assessment of the performance of the coatings towards applications through microstructural analyses, mechanical measurements, and machining experiments.

## **1.1 Metal Nitride Hard Coatings**

In 1980, TiN became the first coating to be applied in the industry. Pure TiN coatings are brittle, and there have been enormous efforts to increase the toughness of these coatings while retaining an optimum hardness. Generally, a second metal is added during the deposition of metal nitride coatings to increase the toughness of the coatings. Nine years later, TiAlN followed. Other applied materials are CrN, CrAlN, TiB<sub>2</sub>, ZrN, and carbon coatings such as diamond or DLC (Kataria et al., 2012). The common tool coatings and their properties are presented in Table 1 below. TiAlN, CrAlN, and ZrAlN are the most common and used as wear-resistant protective coatings for various tools and components to improve performance (Bobzin, 2017). Among them, Ti-Al-N coatings are the most widely used to reduce tool wear. The crystal structure and mechanical properties of Ti-Al-N depend on the Al content. Single-phase cubic Ti-Al-N films with high Al contents exhibit excellent mechanical properties, age-hardening, and oxidation resistance (Chen et al., 2011).

Density functional theory studies support that the addition of refractory elements changes the mechanical properties of the hard coatings. It has been known that materials with a low shear modulus to volumetric modulus ratio ( $G/B$ ) and positive Cauchy pressure (elastic constant difference,  $C_{12}-C_{44}$ ) offer higher fracture toughness (Pettifor, 1992; Pugh, 1954). In recent years, it has been possible to



systematically examine the G/B and Cauchy pressure properties of different hard coating alloys with density functional theory calculations (Music et al., 2016). These studies have shown that adding high refractory elements (such as Ta, W, Nb, Zr) to coatings such as TiAlN and CrAlN can significantly increase fracture toughness. Figure 1 shows the slip modulus vs. Cauchy pressure graph from the literature (Sangiovanni et al., 2012).

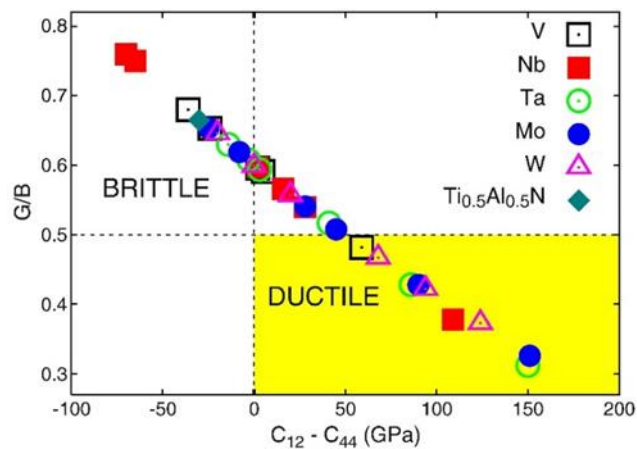


Figure 1. G/B and  $C_{12}$ - $C_{44}$  values of different coatings (Sangiovanni et al., 2012).

Experimental examination of these theoretical calculation-based predictions is essential for developing new-generation hard and ductile coatings in light of this information. Experimental studies in this area are quite limited but promising as the findings mentioned above are promising.

In the literature, 2, 5, and 10 at.% W addition to TiAlN improved surface quality of cathodic arc evaporated samples. Generally, mechanical and thermal properties were improved as the amount of W increases. Wear properties improved with increasing of the  $H^3/E^2$  (the resistance against the plastic deformation), and the friction coefficient did not change ( $\sim 1$ ) (Glatz, Bolvardi, et al., 2017). Another study for Mo addition to TiAlN shows 2, 5, and 10 at.% Mo changes the mechanical behavior of the metal nitrides. For 10 at.% Mo, wear rate was too small to be detectable.

Molybdenum oxides formation decreases the wear rate by three at.% (Glatz, Koller, et al., 2017). They claimed that there are no detailed studies on arc evaporated TiAlWN, too.

In the literature, Nb additions to TiAlN coatings did not change the hardness but reduced the modulus of elasticity from 440 GPa to 360 GPa. Accordingly, it is known that increasing the hardness-elastic modulus ratio (H/E) reduces the brittleness of coatings (Leyland & Matthews, 2000). Similarly, nanoindentation experiments on Mo-added VN coatings determined that Mo additions increase fracture toughness (Kindlund et al., 2013). Although fracture toughness data are not available, a significant increase in wear resistance has been observed with Zr additions to TiN coatings (Knotek & Leyendecker, 1987). These and similar findings (Seidl et al., 2018; Yang et al., 2017) indicate that refractory metal additions can increase the fracture toughness of hard coatings in practice, increasing the wear resistance.

Table 1. Characteristics of popular hard coatings.

<b>Valuation</b>	<b>Chemical stability</b>	<b>Oxidation stability</b>	<b>Hardness at RT</b>	<b>Hot hardness</b>
++	Al <sub>2</sub> O <sub>3</sub>	Al <sub>2</sub> O <sub>3</sub>	TiC	Al <sub>2</sub> O <sub>3</sub>
+	TiAlN	TiAlN	TiCN	TiAlN
0	TiN	TiN	Al <sub>2</sub> O <sub>3</sub>	TiN
-	TiCN	TiCN	TiAlN	TiCN
--	TiC	TiC	TiN	TiC

Improvement of different ternary nitride coatings has been significant research for the machining industry in the last few years to get advanced film properties such as high hardness, wear-resistance, corrosion protection, melting point. A small amount

of addition of the elements changes the morphology, mechanical and thermal behavior, and structure (Chauhan & Rawal, 2014).

MNs, also called hard coatings, increase the lifetime of cutting tools by improving their wear resistance and allowing higher speed dry cutting. The cutting edge of a tool can reach very high temperatures during machining; therefore, the hardness and fracture toughness of a coating at elevated temperatures is critical for the wear resistance performance of a coating.

Coated tools are widely used for metal cutting applications. In dry machining, the tool is charged with high friction, mechanical and thermal load. New coatings with superior properties have to be developed to increase the efficiency of tools for dry cutting. The main requirements for advanced coating systems are (Cremer & Neuschütz, 2001):

- Good oxidation resistance under conditions of dry machining or high-speed cutting,
- High surface quality, which ensures an improved tribological behavior and damage resistance, increases the tool life and reduces friction and, thus, the need for coolants and lubricants,
- Increased surface hardness, which ensures the desired resistance against wear.

## **1.2 Production of Hard Coatings**

Two main methods are used to coat hard materials to any tools: Chemical vapor deposition (CVD) and physical vapor deposition (PVD). There is generally a simple rule of thumb: turning requires thicker CVD coatings due to their larger wear volume when choosing a coating technology. On the other hand, thinner PVD coatings are more suitable for milling due to the residual compressive stress and sharper cutting edges (Bobzin, 2017).

One of the most common techniques to prepare thin films is physical vapor deposition (PVD) (Mehran et al., 2018). The target material is evaporated into a vacuum chamber where the substrate is placed. Nanostructured materials in the form of thin films can be fabricated using this technique.

Magnetron sputtering is the most commonly used PVD technique for research purposes. This method relies on magnetically accelerated inert gas ions to knock out atoms of a target material, sputter them into a vacuum chamber, and cause them to eventually condense onto a substrate (Kelly & Arnell, 2000). The ion bombardment of the surface of the target material generates secondary electrons, which in turn results in a continuous plasma in the chamber. Figure 2 below shows the mechanism of magnetron sputtering.

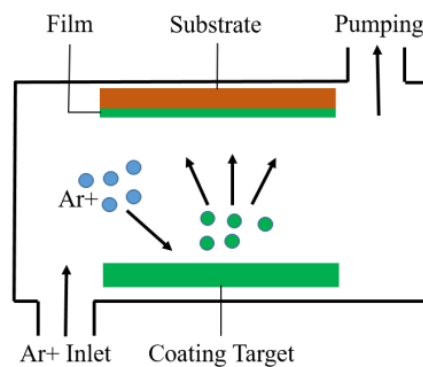


Figure 2. Schematic drawing of magnetron sputtering (Abboud, 2018).

Magnetron sputtering is used to produce hard, wear-resistant coatings, low friction coatings, corrosion-resistant coatings, decorative coatings, and coatings with specific optical or electrical properties (Kelly & Arnell, 2000).

Another PVD technique to coat cutting tools is cathodic arc evaporation (CAE). This technique works at low-voltage and high-current plasma discharge, and particles evaporate from cathode target material and condense on a substrate surface in a vacuum ambient. In the absence of magnetic fields applied to the cathode, arc spots

move randomly over the cathode surface (Deng et al., 2020). Figure 3 shows a schematic view of a cathodic arc evaporation system.

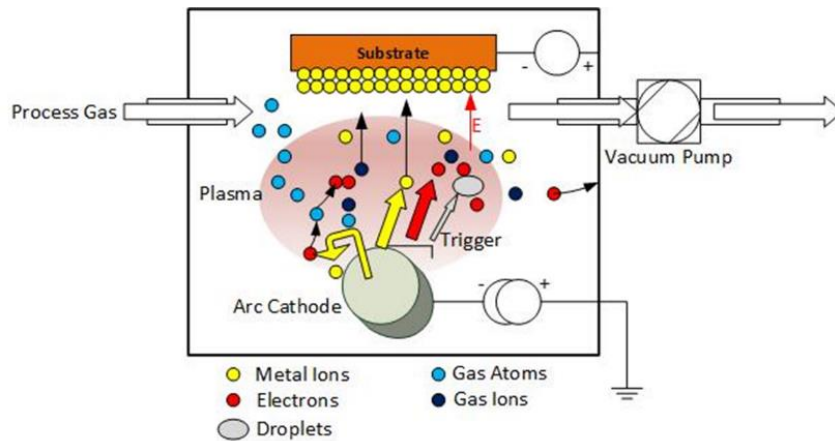


Figure 3. Schematic view of cathodic arc evaporation technique.

Coated surfaces can be obtained by magnetron sputtering smoother, and the working temperature is lower than cathodic arc evaporation. However, the low ionization ratio of traditional magnetron sputtering limits its industrial application (Wei et al., 2002).

### 1.3 Mechanical Characterization Techniques

#### 1.3.1 Nanoindentation

Nanoindentation is a small-scale mechanical test to obtain hardness and elastic modulus. Nanoindentation utilizes a diamond tip such as Berkovich tip, spherical tip, and cube corner tip to penetrate the sample surface. A nanoindentation device equipped with force and displacement sensors generated the load-displacement curve of the test (Allsopp & Hutchings, 2001; Sveen et al., 2013). Hardness and elastic

modulus is commonly determined by the Oliver-Pharr method developed in 1992 (Oliver & Pharr, 1992). The hardness is then calculated as the force applied divided by the projected area of the contact surface between the tip and the sample. Figure 4 shows the schematic of a typical load-displacement curve.

Besides hardness and elastic modulus, storage and loss modulus, strain rate sensitivity, yield strength, strain hardening coefficient, residual stress, the adhesive strength of coatings, and fracture toughness can be determined by this technique (Lawn et al., 1980).

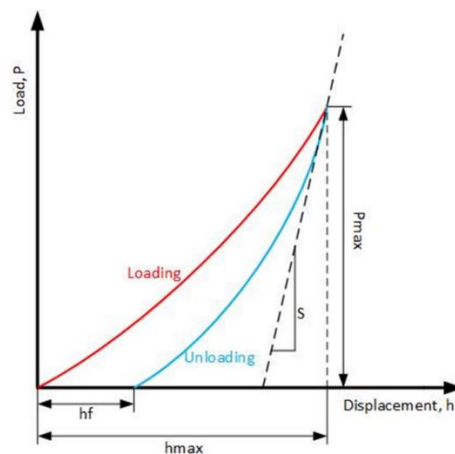


Figure 4. The schematic of a load-displacement curve of Nanoindentation (Abboud, 2018).

Application areas of the nanoindentation can be listed as:

1. Small samples or thin films (thickness <math>< 5 \mu\text{m}</math>) cannot be tested by traditional macro-scale mechanical tests due to the substrate effect.
2. A sample is large, but the mechanical behavior of the specimen at the microscale is of main interest.
3. Samples are not suitable for a high-loaded test such as powder or nonhomogeneous composition (Fischer-Cripps, 2002; Oliver & Pharr, 1992).

Some crucial parameters such as surface roughness, the shape of tips, the ratio between film thickness and substrate, vibration, and thermal drift significantly affect the reliability of the results of Nanoindentation tests. The surface of specimens should be clean and polished before performing the Nanoindentation test as any surface irregularity will change the mechanical response and result in an error. Moreover, diamond tips are not perfectly sharp, and they can also get dirty and experience some wear and become dull. The stress field below the indenter tip can remain significant at depths up to ten times the indentation depth. Thermal drift would cause erroneous results; therefore, the temperature should be maintained at a stable level in the room. Since mechanical vibrations are not desirable during the tests, nanoindenters are usually placed on a basement floor (S. Chen et al., 2005; Gamonpilas & Busso, 2004; Tsui et al., 1999).

Film thicknesses are generally 1-5  $\mu\text{m}$ , and traditional mechanical tests are unsuitable for these thin-film specimens; therefore, fracture toughness measurement on thin films is quite tricky. Nanoindentation is used to create cracks at the neighboring areas of the indents after the test to tackle this issue and calculate the fracture toughness of thin-film specimens. After Nanoindentation, these cracks are observed by Scanning Electron Microscopy (SEM), then the fracture toughness can be measured using these cracks dimensions and equation (1) (Sebastiani et al., 2015).

$$K_{IC} = \alpha \left( \frac{E}{H} \right)^{1/2} \times \left( \frac{P}{c^{3/2}} \right) \quad (1)$$

Where  $\alpha$  is the tip geometry constant,  $E$  is elastic modulus,  $H$  is hardness,  $P$  is the maximum load, and  $c$  is the crack size.

Microstructural features (e.g., grain size and distribution, defect density, and the substrate/coating interface) further contribute to the complexity of fracture toughness measurement (Sebastiani et al., 2015).

Indentation-based methods with sharp pyramidal indenters have been widely used as they are relatively easy to use in testing and make the sample preparation phase easier. Figure 5 shows an SEM image after our nanoindentation test results, where cracks can be seen at the corner of the indent.

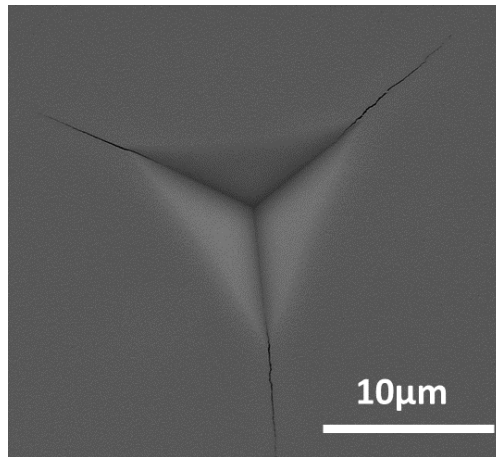


Figure 5. SEM image of cracks after nanoindentation.

### 1.3.2 Micro and Nanoscratch Testing

Mechanical characterization is an essential part of the design and development of novel PVD or CVD coatings. Especially, understanding the coating/substrate deformation mechanism is the main focusing area for wear applications. The micro or nano scratch is the standard test of tribology test. In this method, a Rockwell diamond tip (radius of 200  $\mu\text{m}$ ) is moved across the coated surface of the specimen at a constant velocity while a steadily increasing normal force is applied. The diamond causes stress between the thin film coating/substrate interface resulting in delamination or chipping of the coating. The normal force at which the first failure of the coating can be detected is termed the critical load  $L_c$ . Figure 6 represents an SEM image and schematic of the scratch test.



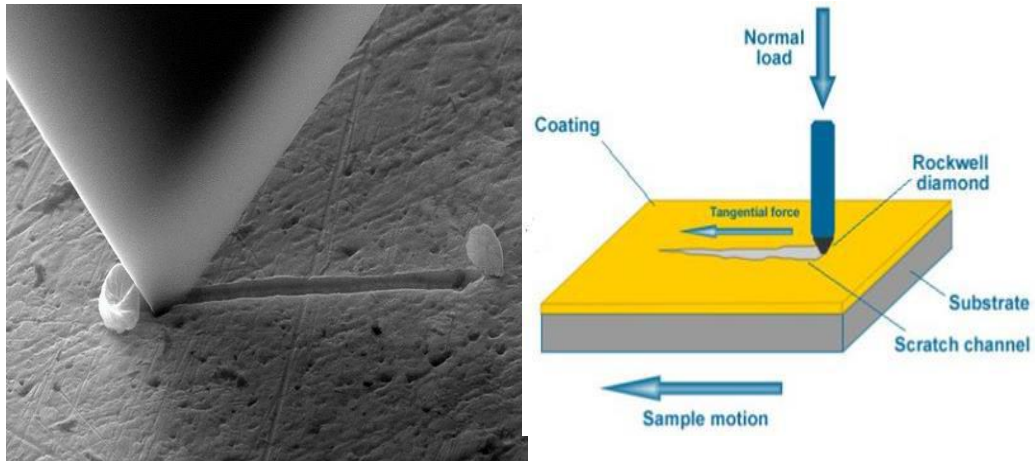


Figure 6. SEM image and schematic of scratch tested surface of a specimen (Nanomechanical Instruments for SEM/TEM, n.d.).

### 1.3.3 Microcantilever Bending

Another fracture toughness measurement technique is microcantilever bending. This technique is newer than the other fracture toughness measurement techniques, especially for thin films. This method has recently been developed to resolve some of the indentation-based fracture toughness measurements of films (Riedl et al., 2012; Ast et al., 2019). The methods generally use a nanoindentation system to apply force to and measure the displacement. The geometry of specimens was produced by focused ion beam (FIB) milling (Sebastiani et al., 2015). Figure 7 shows an example of single-cantilever beam specimens.

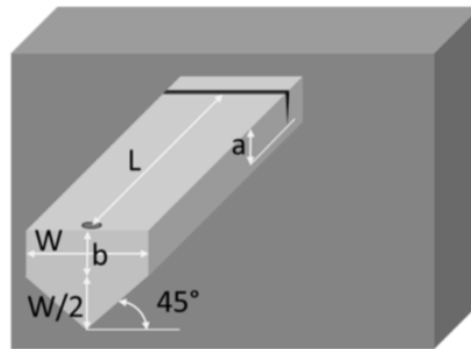


Figure 7. Schematic representation of the micro-cantilever bending geometry (Sebastiani et al., 2015).

Due to the small sample size, mechanical measurements should be tested using a device that applies mN force and nm displacement precision. For this purpose, a nanoindenter may be used. Spherical or Berkovich diamond tips are commonly used for nanoscale measurements. The force applied to the sample gradually increased, and the breaking point of the sample is determined by the nanoindenter (R. Hahn et al., 2016; Maio & Roberts, 2005). An example load-displacement curve obtained from the microcantilever bending test is shown in Figure 8.

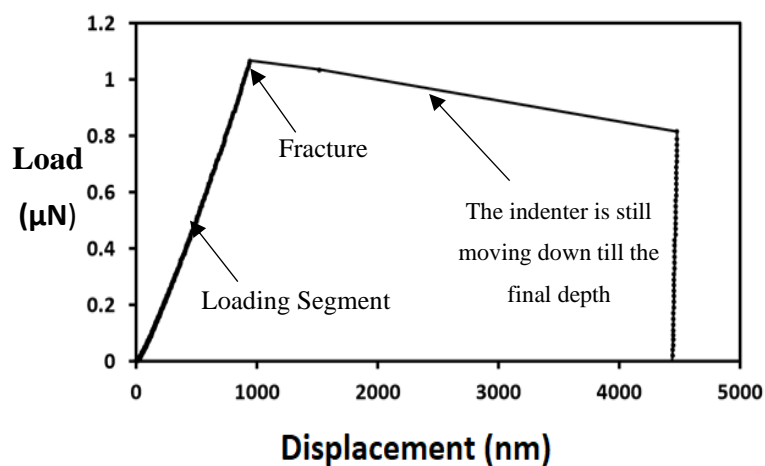


Figure 8. The load-displacement curve for Si wafer (Maio & Roberts, 2005).

After the bending test, the fracture toughness of hard coatings can be calculated by using equations (2) and (3) (R. Hahn et al., 2016).

$$K_{IC} = \frac{P_{max} l}{bw^{3/2}} f\left(\frac{a}{w}\right) \quad (2)$$

$$f\left(\frac{a}{w}\right) = 1.46 + 24.36 \left(\frac{a}{w}\right) - 47.21 \left(\frac{a}{w}\right)^2 + 75.18 \left(\frac{a}{w}\right)^3 \quad (3)$$

$P_{max}$  is the maximum load, and  $a$  is notch depth,  $l$  is cantilever length (from notch to loading point),  $b$  is cantilever width, and  $w$  is film thickness.

#### 1.4 Wear Measurements

Tribology is the science of investigating the interaction between contact surfaces. The major topics in tribology are wear, friction, and lubrication (Richard et al., 2015).

Wear means deformation of surface and loss of material because of motion between contacted surfaces. Friction can be defined as resistance to relative motion between contact surfaces. The market size of wear and friction is getting impressive, and improvement of it has started with cutting tools coating. It is known that high hardness and good wear and corrosion resistance materials are desired to improve tool life. TiN, CrN is the first hard coating to improve tool life in the industry, and then the ternary coating systems are attractive and popular due to excellent mechanical properties (Bobzin et al., 2007; Kılınç et al., 2014; Richard et al., 2015).

The performance of cutting tools is usually measured by tool life tests such as pin-on-disc, ball-on-disc test, or test with cutting tools (drilling, turning, or milling test). Pin-on disc/ball-on-disc test is a common method used to measure the wear

properties of the hard coatings. Depending on the relative hardness, wear takes place either on the ball, coating surface, or both. The wear resistance is expressed in terms of worn volume. The wear volume of chromium steel balls against coated high-speed steel disc was measured at a constant applied normal force (Bobzin et al., 2007; Mo & Zhu, 2008). Figure 9 shows a schematic view of pin-on and ball-on disc tests (tribonet, 2019).

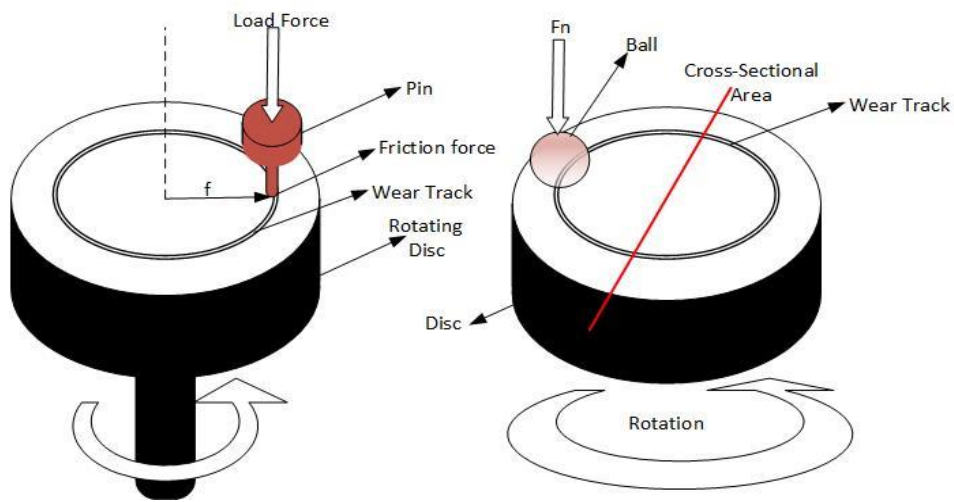


Figure 9. Schematic of the pin on and ball on disc tests (Tribonet, 2019).

The other common ball materials are Alumina ( $\text{Al}_2\text{O}_3$ ), Silicon nitride ( $\text{Si}_3\text{N}_4$ ), and stainless steel. The analysis of tribological contact partners included determining the coefficient of friction, wear rates and wear debris (Bobzin et al., 2007). The chemical structure of counterpart materials affects the test results. For instance,  $\text{Al}_2\text{O}_3$  is more inert than  $\text{Si}_3\text{N}_4$ , which tends to oxidize due to their chemical bonding (Alumina-ionic, Silicon nitride-covalent) (Raider et al., 1976).

Nominal load, rotational speed, substrate material, counterpart material, test temperature are determined parameters for tribology tests.

Having information about the machined material is not enough; selecting the right cutting tool and convenient coating on that tool is also essential. The non-convenient machining parameters such as the scrapped tools, faster wear, burning of coating material, and low surface quality of machined material can affect financial results. To understand and reduce these adverse effects on machining cost, some real performance tests can be done: drilling, milling, turning tests (Aydın et al., 2012; Zawada-Michałowska et al., 2020).

The friction coefficient and wear rate can be measured, and also wear behavior of coated tools can be analyzed using Scanning Electron Microscopy (SEM) or Energy Dispersive Spectroscopy (EDS). These are common analysis methods to understand wear types on the coated tools. Various wear mechanisms can be observed in the literature, such as adhesive, abrasive, and flank. These failure mechanisms can be changed due to cutting speed and temperature change due to the high speed of tools (Bobzin, 2017; Bouzakis et al., 2012a). Figure 10 shows wear types from the literature (Bouzakis et al., 2012b).

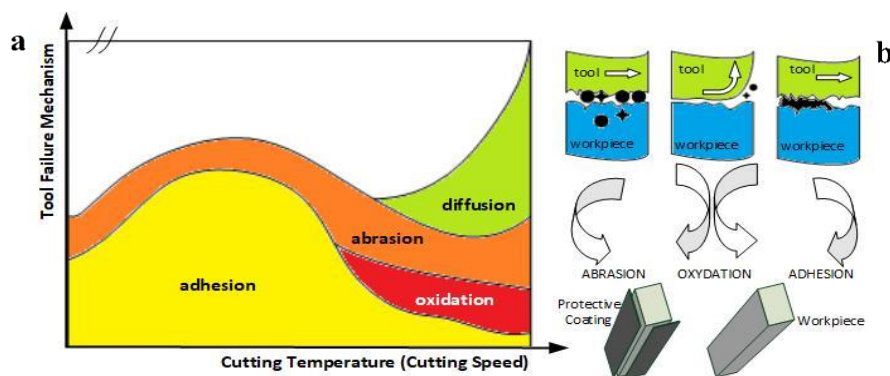


Figure 10. Wear mechanism according to cutting speed, b) types of wear mechanism (Bouzakis et al., 2012b).



## CHAPTER 2

### MAGNETRON-SPUTTERED COATINGS

#### 2.1 Experimental Details

##### 2.1.1 Sample Preparation

The reactive magnetron sputtering at a laboratory scale system was utilized to prepare various hard coatings. TiAl, CrAl, and W targets (2" diameter and 1/4" thickness elemental disks of 99.99% purity) which were produced by powder metallurgy and VAKSİS PVD Magnetron Sputterer (Vaksis, Turkey) with two guns devices, were used to coat samples on single crystal Si (100) wafer as a substrate. All sputtering targets were taken from Nanografi, Turkey. Substrates were cut by a diamond cutter and cleaned by ultrasonication with acetone and isopropyl alcohol, followed by drying with nitrogen. The prepared sample was taken into the chamber, and the chamber was pumped down for 4-5 hours at  $10^{-4}$  Pa. Hence, the availability of oxidation or other contamination was reduced to a minimum level. Figure 11 shows the Vaksis PVD magnetron in METU and PVD magnetron in İTÜ.

Optimum Nitrogen amount was studied to prevent target poisoning, which reduces the coating quality. A mass flow controller was used to give  $N_2$  to the system. Before sputtering, Ar plasma was used to clean the sample and chamber and better adhesion between coating material and substrate. Substrates were placed in a circular stage, and the stage was rotated around its center to obtain a homogeneous coating. During coating, Al-Cr or Al-Ti targets and W targets are put on the guns, working simultaneously. W additions were the main focus of the study as density functional theory calculations suggest that W is the most effective element addition for improving the toughness. The alloy compositions are obtained by adjusting the

power of the guns. 2%, 5%, and 10 at. % of W were desired. Other coating parameters were listed in Table 2. The bias voltage 80V was applied for the first experimental trials. In general, with the increase of the bias voltage, the coating hardness and adhesion between the substrate and films increases. This is due to the ion bombardment is explained by the dense internal structure. When the bias voltage rises above a certain value, the amount of increase in hardness decreases, and stress in the structure increases. Those coatings were not stable on the substrate (see Figure 12). It was observed that they began to remove from the surface after a short time. The high bias voltage can cause high stress at the surface of the substrate materials. Coated films were removed from surfaces of substrates which were Si(100) and stainless steel. Stainless steel was polished, and there was no heat treatment before using as a substrate. After these experiments, bias voltage was not applied in the coating system due to high stress on the surfaces and the adhesion problem of the films.



Figure 11. Vaksis Magnetron Sputterer in ODTÜ and in-house manufactured Magnetron Sputterer in İTU.





Figure 12. Samples for first magnetron sputtering trials.  $\text{Al}_{67}\text{Ti}_{33}\text{N}$  on SS substrate (left) and  $\text{Al}_{50}\text{Ti}_{50}\text{N}$  on Si(100) substrate (right).

Table 2. Coating parameters for magnetron sputtering.

Vacuum before sputtering	$1 \times 10^{-7}$ Torr
Vacuum during sputtering	$1 \times 10^{-4}$ Torr
Coating duration	1-2 hours
Power	100-200 W
Composition of Al: Ti target	50:50 and 67:33
Composition of Al: Cr target	50:50
Total film thickness	$\sim 2-4 \mu\text{m}$
Bias	None and 80 V

Table 3 shows details of coating parameters of samples produced by the Magnetron sputtering technique. The critical parameters are Nitrogen flow (sccm), pressure, and target power. Generally, target power is set to 200W to obtain Al-Ti /Al-Cr coatings. Different nitrogen-argon flows were tried to see the effect of nitrogen amount on nitride formation. Effects of these parameters were explained after structural characterization, which was mentioned below.

Table 3. Details of samples produced by magnetron sputtering. (Ref. means reference sample (without W)).

Sample Name	Content of Sample	Ar-N <sub>2</sub> (sccm)	Power (Watt)	Pressure (Pa)	Duration (min)	Thickness (μm)
5050-ref.	(Al <sub>50</sub> Ti <sub>50</sub> )N	100-60	200	0.7-0.75	120	3.1
5050-1	(Al <sub>50</sub> Ti <sub>50</sub> )WN	100-80			120	3.4
5050-2	(Al <sub>50</sub> Ti <sub>50</sub> )WN	100-40		0.6-0.69	110	2.5
5050-3	(Al <sub>50</sub> Ti <sub>50</sub> )WN	100-40			110	3.3
6733-ref.	(Al <sub>67</sub> Ti <sub>33</sub> )N	100-40		0.6-0.7	120	3.5
6733-1	(Al <sub>67</sub> Ti <sub>33</sub> )WN	60-40			105	3.5
6733-2	(Al <sub>67</sub> Ti <sub>33</sub> )WN	100-40			105	3.3
AlCr-ref.	(Al <sub>50</sub> Cr <sub>50</sub> )N	100-40			120	~3 *
AlCr-1	(Al <sub>50</sub> Cr <sub>50</sub> )WN				70	3.4
AlCr-2	(Al <sub>50</sub> Cr <sub>50</sub> )WN				70	3.3

\*measured coating thickness is not uniform everywhere of the specimen.

## 2.1.2 Microstructural Characterization

Several characterization techniques were used to understand the specimens' crystal structure, morphology, and elemental composition before evaluating their mechanical behavior. These analysis methods were X-Ray Diffraction (XRD), Scanning Electron Microscopy (SEM), Energy-Dispersive X-ray Spectroscopy (EDS/EDAX), X-ray photoelectron spectroscopy (XPS), Wavelength-Dispersive X-ray Spectroscopy (WDS), Focused Ion Beam (FIB). Each of these was briefly explained in this section.

### 2.1.2.1 X-ray Diffraction (XRD)

XRD is a powerful technique to understand the crystal structure (strain state, grain size, epitaxy, phase composition, preferred orientation, and defect structure) of materials. The method is not in contact with the sample surface; thus, it is nondestructive. Sample should not have unique properties to analyze such as conductive, extra thin, or bulk only sample top and bottom surface should be flat. Powder materials, polymeric or metallic materials, thin films, or bulk materials can be analyzed by XRD (Brabazon & Raffer, 2015).

The regular orientation of atoms in a crystalline material creates a 3D diffraction grating for waves with wavelengths around the distance between atoms. When waves enter a crystalline material, they are scattered by atoms in all directions. In specific directions, these waves can interfere destructively. In other directions, constructive interference will occur, leading to peaks in X-ray intensity. The resulting diffraction pattern is a map of the crystal's reciprocal lattice and can determine the crystal structure. Bragg's law is the basis for crystal diffraction:

$$n\lambda = 2d\sin\theta \quad (4)$$

Where  $n$  is an integer known as the order of diffraction,  $\lambda$  is the X-ray wavelength,  $d$  is the spacing between two consecutive scattering planes, and  $\theta$  is the angle between the atomic planes and the incident (and diffracted) X-ray beam (Brabazon & Raffer, 2015).

The grain size is calculated by using Scherrer Equation:

$$B(2\theta) = \frac{K\lambda}{L\cos\theta} \quad (5)$$

Where  $K$  is the shape factor (0.89-0.94),  $B$  is related to the peak width at half maximum (FWHM), and  $L$  is the crystallite size. When the crystallite size becomes smaller, the peak becomes wider. (Ingham & Toney, 2014; Langford & Wilson, n.d.).

A Rigaku Ultima-IV diffractometer (Central Laboratory in METU) was used for XRD analysis in grazing incidence mode at  $1^\circ$ . The grain size was measured using the Scherrer equation by using Jade software. Copper wavelength ( $K\alpha$ ) is  $1.5418 \text{ \AA}$ . In this study, XRD results were taken at the  $20\text{-}100^\circ$   $2\theta$  range for all prepared specimens, and they were compared with related ICDD PDF cards.

#### **2.1.2.2 Scanning Electron Microscopy (SEM) & Energy Dispersive X-ray Spectroscopy (EDS)**

Scanning electron microscopy has been used to understand the surface morphology (shape and size), topography (surface features), crystallographic information (atoms arrangement), and elemental composition of the samples since 1935. Bulk, thin-film, nanostructured, powder, or other forms of samples can be analyzed by this method. Focused electrons are sent to the sample surface at a spot of the specimen. Then after interaction between sample and electrons, all electrons are collected to take information about the samples. It is a semi-nondestructive and easy-to-use method.

It gives better resolution than light microscopy; however, samples should be conductive, it works under vacuum. Under high accelerating voltage (e.g., 30kV), well-aligned apertures, well-corrected astigmatism, small spot size (small probe current), and no sample charging, resolutions of 3nm can be obtained (Brabazon & Raffer, 2015; Rieth, 2003). Figure 13 shows the interaction between the incident electron beam and the sample's surface (Goldstein et al., 1992).

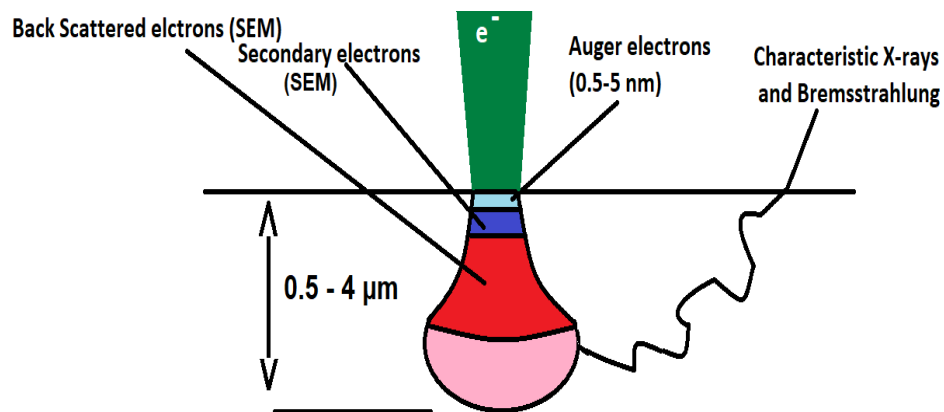


Figure 13. The interaction between the incident electron beam and the surface of the sample (Goldstein et al., 1992).

In this thesis, FEI Quanta 400F Field Emission scanning electron microscope (FESEM) performed surface imaging and EDS in METU Central Laboratory. 4-5 spot size, 20-30 kV accelerating voltage, and different magnification were applied to better see the specimens' surface.

### **2.1.2.3 Wavelength Dispersive Spectroscopy (WDS)**

Wavelength dispersive X-ray spectroscopy (WDS) is similar to EDS but analyses the diffraction patterns from the material–radiation interaction to identify one element at a time. WDS provides more reliable results than the EDS, especially Nitrogen amount, which is an essential element for metal nitrides. This technique has a better spectral resolution than the EDS (Brabazon & Raffer, 2015). In this thesis, all WDS analyses were done using the JEOL JXA – 8230 WDS device at 20 kV accelerating voltage in METU Central Laboratory. The N, Ti, Al, Cr, and W in the samples were defined after EDS analysis.

### **2.1.2.4 X-ray Photoelectron Spectroscopy (XPS)**

X-ray photoelectron spectroscopy (XPS) analyses electron emission of similar high energy. XPS can be used to measure the chemical or electronic state of surface elements, detect chemical contamination, or map the chemical uniformity of biomedical implant surfaces (Goldstein et al., 1992).

In this thesis, XPS analysis was used to understand the atomic structure, and chemical bonding of N, Ti, Al, Cr, and W. Thermo Fischer with Al K $\alpha$  X-ray monochromatized sourced XPS device Bilkent University-UNAM was used, and spot size was 400  $\mu\text{m}$ . Before the measurement, the coating surface was bombarded with argon ions with an energy of 500 eV for 2 minutes at a medium current. Thus, the surface is etched up to 10 nm, preventing possible contamination from affecting the results.

### **2.1.3 Mechanical Characterization**

As mentioned before, micromechanical properties such as hardness, elastic modulus, fracture toughness are measured and evaluated using the nanoindentation technique.

#### **2.1.3.1 Nanoindentation**

After the structural analysis, the mechanical properties were analyzed by the nanoindentation method. Nanoindentation and elasticity modules were measured with the Agilent G200 Nanoindenter device at Koç University Surface Technologies Research Center (KUYTAM) at room temperature with displacement control. Diamond Berkovich and cube corner tips were used in the measurements, and depth-related data were obtained through a continuous stiffness measurement technique (CSM). Hardness measurements for each sample were repeated at least at 15 different points. The obtained stiffness and elasticity modules were determined using the Oliver-Pharr method via the Nanosuite software (Oliver & Pharr, 1992).

#### **2.1.3.2 Fracture Toughness Measurement**

After the nanoindentation tests, the indents and cracks formed on the sample surface were first investigated with a Nikon E200 optical microscope in Nanomechanical Laboratory, METU. Then, SEM was used to determine crack size at the corner of the indents. Relevant crack sizes were measured using Image J software. Further details on fracture toughness calculated in the light of crack dimensions are given below parts.

## 2.2 Results and Discussion

### 2.2.1 Microstructure

All samples were firstly characterized structurally by XRD and SEM&EDS techniques. The details of the experiments were mentioned in this part. All structural characterization was done at Central Laboratory in METU.

Figure 14 shows XRD data of the Al<sub>50</sub>Ti<sub>50</sub> based specimens. Step scanning was 1 °/min, and scans were run between 20° to 100°. Structure data obtained by previous experimental were taken from the Inorganic crystal structure database (ICSD), and they were compared with the literature. Scherrer equation was applied by Jade MDI software to approximate the average crystal size in the films. The wavelength for Cu K $\alpha$  is 1.5418 Å at 22.85°C. The glancing angle mode where the angle between the incoming beam and the sample surface was 1°. At. % of W and other elements were mentioned in EDS results which were below.

All produced AlTiN-based coatings have narrow-angle peaks and show crystalline structure. The peak angles indicate the cubic structure and are consistent with similar coatings in the literature (Fan et al., 2017). With W to the AlTiN coatings, there was no significant change in the XRD data. Tungsten nitride (111) peak was observed for W-added nitrides. There were small shifts in the peak angles due to the variation in the mean interatomic distance experienced due to the different sizes of W atoms compared to Ti and Al atoms. It is also possible that said shifts are due to different residual stresses between the films. It can be said that the W atoms in these coatings are included in the coating in the form of a new phase (W<sub>2</sub>N) and do not exhibit any intermetallic forming or precipitation behavior.



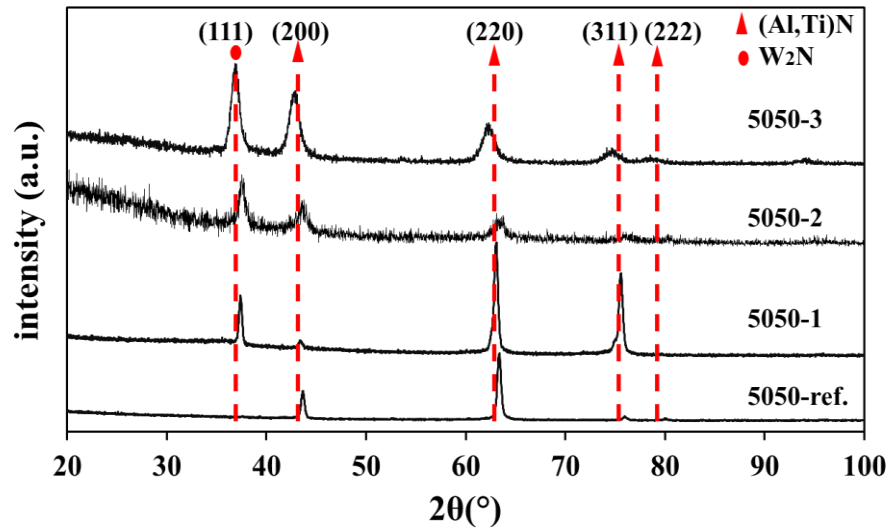


Figure 14. XRD results of  $\text{Al}_{50}\text{Ti}_{50}$  based specimens. 5050-ref. means  $\text{Al}_{50}\text{Ti}_{50}\text{N}$  (without W), 5050-1, 5050-2, and 5050-3 are  $(\text{Al}_{50}\text{Ti}_{50})\text{WN}$  with different W amounts.

Figure 15 shows XRD data of the  $\text{Al}_{50}\text{Cr}_{50}$  based specimens. All experimental details were the same for these samples. W additions did not add any new peaks in  $(\text{Al}_{50}\text{Cr}_{50})\text{N}$  coatings. There was a shift in the peak angles due to different sizes of W, Al, and Ti atoms. The widening of peaks shows distortion in the structure of the materials, and the crystal structure changed from crystalline to more amorphous. This change is in agreement with the literature (Yousaf et al., 2015)

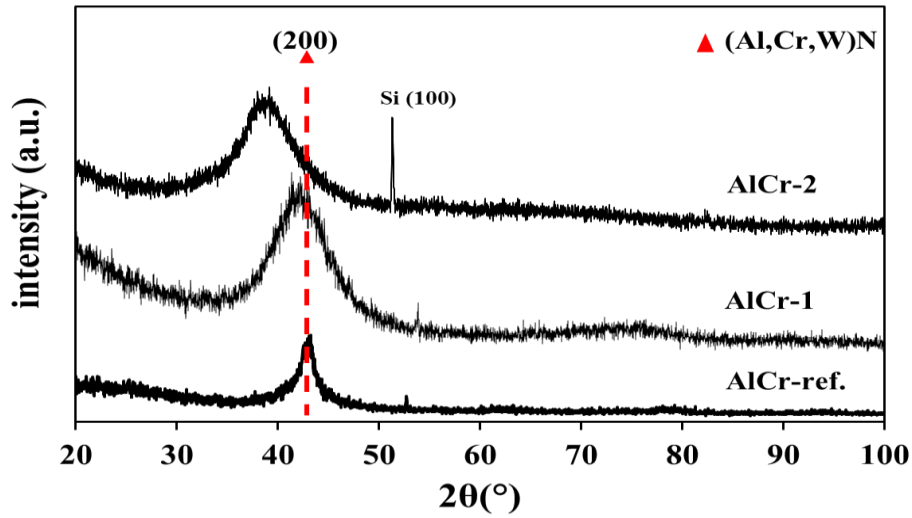


Figure 15. XRD results of AlCr based specimens. AlCr-ref. means without W, AlCr-1, and AlCr-2 are  $(Al_{50}Cr_{50})WN$  which have different W amounts.

Figure 16 shows XRD results of  $Al_{67}Ti_{33}$  based specimens. With W to the AlTiN coatings, there is no significant change in the XRD data. As the content of Al increases up to 67%, more high and broad peaks can be seen due to amorphous structure (Flink et al., 2008). Additionally, as the Al amount increases in the structure, X-ray diffraction data from (111) and (220) planes decreases (no (111) after 65 % Al), X-ray diffraction data from (200) plane increases (Mo & Zhu, 2008). In light of this information, it can be said that  $Al_{67}Ti_{33}$  based samples' XRD results agree with the literature.

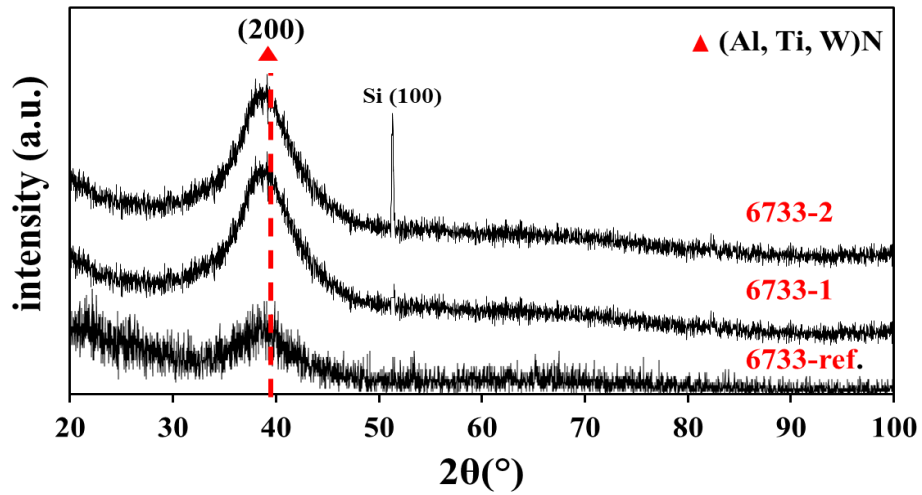


Figure 16. XRD results of  $\text{Al}_{67}\text{Ti}_{33}$  based specimens. 6733-ref. means  $\text{Al}_{67}\text{Ti}_{33}\text{N}$  (without W), 6733-1, and 6733-2 are  $(\text{Al}_{67}\text{Ti}_{33})\text{WN}$  with different W amounts.

XRD results were also used to calculate crystalline size by using the Scherrer equation. Table 4 shows calculated crystalline size by using the MDI Jade analysis program.  $K$  was taken 0.9,  $\lambda$  was  $1.54 \text{ \AA}$  for Cu  $K\alpha$ . The crystalline sizes were larger than the literature values, generally 5-15 nm (García-González et al., 2007). Crystalline size is an effective parameter on the mechanical properties of thin films. It will be mentioned in mechanical characterization Section 2.2.2.

Table 4. The calculated grain size of the magnetron sputtered samples.

<b>Sample name</b>	<b>2<math>\theta</math> (°)</b>	<b>Crystalline size (nm)</b>
5050-ref.	63.2	27
5050-1	63.3	26
5050-2	38.9	25
5050-3	38.9	27
6733-ref.	39	16
6733-1	38.9	16
6733-2	38.8	16
AlCr-ref.	43.3	29
AlCr-1	42.8	25
AlCr-2	42.4	26

After XRD analysis, the elemental composition was determined by using EDS and WDS. All analyses were done in Central Laboratory in METU. EDS analysis was done at the same time SEM and WDS were done in EPMA (Electron Probe Micro Analysis) device. This technique has more precision for counting most of the elements compared to EDS. EDS is also not enough to understand the amount of nitrogen, so WDS was used to get reliable data about the nitrogen amount. According to The EDS and WDS results, Al, Ti, Cr, and W amounts are close. W at.% were not at the desired level. Table 5 shows the EDS and WDS results of the samples.

Nitride formation was also lower than expected values for most of the samples. This low nitrogen amount will be adequate for the mechanical behavior of hard coatings. It can be said that there is a leak problem with the nitrogen flow system.

According to the flow of nitrogen amounts (see Table 3), for Al<sub>50</sub>Ti<sub>50</sub> based samples, increasing the N<sub>2</sub> flow from 40 to 80 sccm increases the at.% of N<sub>2</sub> in the specimens (40 sccm 5050-2 and 80 sccm for 5050-1). Pressure during the coating is also

important for nitride formation. Low pressure (sample 5050-3) showed a better effect on nitride formation.

Table 5. EDS and WDS results of the magnetron sputtered samples.

Sample Name	Sample Content	EDS (at%)				WDS (at%)			
		Al	Ti/Cr	W	N	Al	Ti/Cr	W	N
5050-ref.	Al <sub>50</sub> Ti <sub>50</sub> N	38	26	-	36	29	25	-	46
5050-1	Al <sub>50</sub> Ti <sub>50</sub> N-W	48	46	3.7	-*	29	27	3.5	40
5050-2	Al <sub>50</sub> Ti <sub>50</sub> N-W	52	44	4	-	38	35	4	23
5050-3	Al <sub>50</sub> Ti <sub>50</sub> N-W	52	40	8	-	23	21	5	51
6733-ref.	Al <sub>67</sub> Ti <sub>33</sub> N	57	21	-	22	47	20	-	33
6733-1	Al <sub>67</sub> Ti <sub>33</sub> N-W	66	30	4.2	-	43	20	3	34
6733-2	Al <sub>67</sub> Ti <sub>33</sub> N-W	68	27	5	-	44	21	4	31
AlCr-ref.	Al <sub>50</sub> Cr <sub>50</sub> N	49	43	-	8	42	42	-	16
AlCr-1	Al <sub>50</sub> Cr <sub>50</sub> N-W	50	47	2.5	-	41	41	1.5	16
AlCr-2	Al <sub>50</sub> Cr <sub>50</sub> N-W	52	44	3.5	-	40	40	3.5	16

\*N at% was not determined by EDS to obtain a satisfactory result for W at.%.

Another characterization technique is SEM to measure the thickness and to see the surface morphology of the specimens. All films were analyzed under high vacuum SEM, and they were coated with a few nm of Au-Pd to increase conductivity before surface imaging. Figure 17 shows SEM images of the surface and cross-section view of the films. Generally, there was no adhesion problem between the coated layer and substrate surface, and nonhomogeneous film thickness. Surface morphology was the same for Al<sub>50</sub>Ti<sub>50</sub>, Al<sub>67</sub>Ti<sub>33</sub>, and Al<sub>50</sub>Cr<sub>50</sub> based samples. However, there are small porous areas and can be related to the hard coatings' mechanical properties. It can be observed that the structure was like columnar for AlTi based samples (5050 and

6733), but AlCr structure was not like this. All images were taken at the same accelerating voltage (30 kV), spot size (4.0), and magnification (10000X).

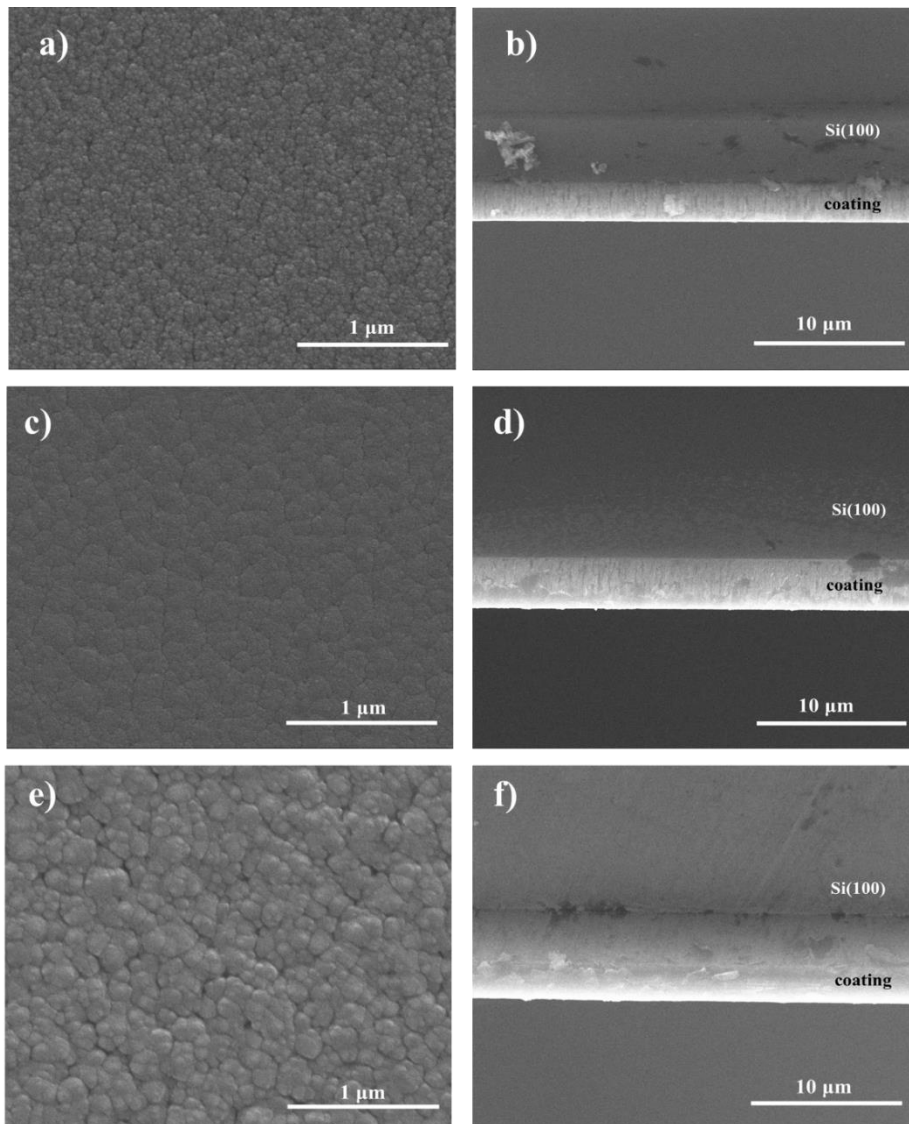


Figure 17. SEM images of a) surface b) cross-section view of 5050-ref. sample, c) surfaced) cross-section view of 6733-ref. sample, e) surface f) cross-section view of AlCr-ref. sample.

The addition of 3.5 at.% of W into the  $Al_{50}Cr_{50}$  based samples changed the structure to some columnar shape; however, it was not uniform. Figure 18 shows SEM images of AlCr-ref (without W) and AlCr-2 (3.5 at.% W) samples. These structural changes are in agreement with the literature. Xu et al., 2018 studied with  $Cr_{45}Al_{55}N$  and V added CrAlN films (film thicknesses are 2.9 and 3.1  $\mu m$ ), and columnar structure was observed in this study (Xu et al., 2018). Another study about the structure of hard coatings shows the same columnar structure for 3.1  $\mu m$  thickness of Ti-Cr-Al-N hard coatings (Xu et al., 2013).

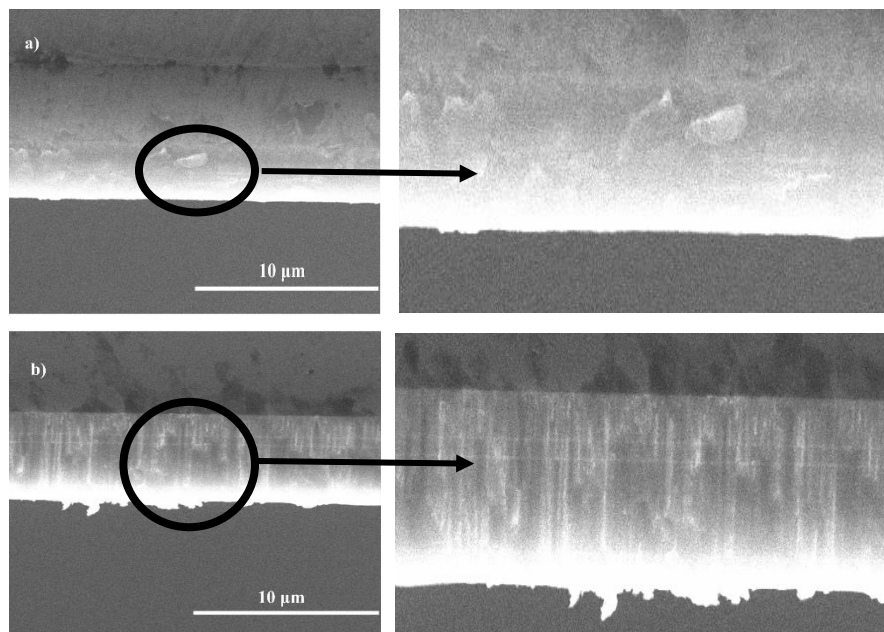


Figure 18. SEM images of a) AlCr-ref, b) AlCr-2 samples.

### 2.2.2 Mechanical Characterization

After microstructure analysis, mechanical properties were analyzed by the nanoindentation method. Nanoindentation data were measured with the Agilent G200 NanoIndenter device located in Koç University Surface Technologies

Research Center (KUYTAM). The diamond Berkovich tip in the measurements was obtained depending on the technical depth and continuous elasticity measurement [CSM]. Fifteen different examinations of hardness measurements were repeated in each detail. Figure 19 represents the nanoindentation result of 5050-ref. ((Al<sub>50</sub>Ti<sub>50</sub>)N), 6733-ref. ((Al<sub>67</sub>Ti<sub>33</sub>)N) and AlCr-ref. ((Al<sub>50</sub>Cr<sub>50</sub>)N). Each color is the result of a measurement performed at a different point. The agreement between the different measurements shows the repeatability of the experiments.

The stiffness and elasticity modules were determined through the Nanosuite analysis program using the Oliver-Pharr method. Each color is the result of the measurement at a separate point. It is seen that the hardness of the coating is quite low in the first 100 nm and then increases gradually. Data in the first 100 nm are often erroneous due to geometrical defects at the diamond tip. On the other hand, as the depth increases, the mechanical properties of the substrate begin to affect the results. Therefore, the hardness values in the relevant regions do not reflect reality. Since the results not affected by the substrate generally correspond to the first 10% depth of the coating, the hardness value for each sample was obtained by averaging the data in the range of 100-400 nm, depending on the film thickness.



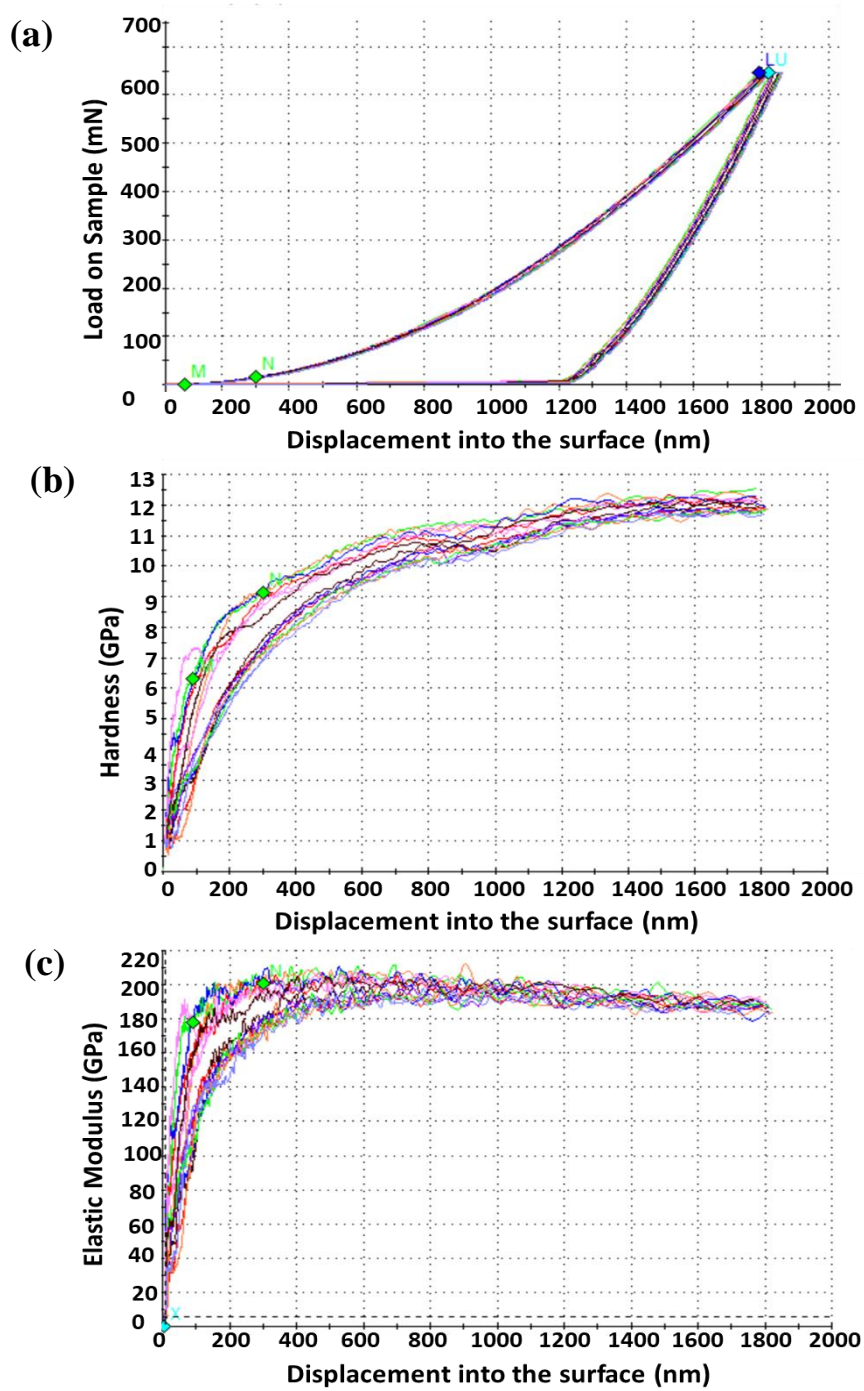


Figure 19. a) Load-displacement, (b) Hardness-depth, (c) Elastic modulus-depth curves of 5050-ref. sample.

Table 6 summarizes all mechanical properties of magnetron sputtering samples after the nanoindentation test. Berkovich tip in the continuous stiffness measurement model was used for the test. Generally, hardness values were lower than literature values (12-15 GPa). Hardness and elastic modulus values are lower than cathodic arc evaporation samples, as explained in the following chapter (3).

Hardness can be defined as the resistance to indentation by a tip. It is a simple definition of it. However, hardness is a very complex character. Surface roughness, grain boundaries, interfaces between coating and substrate material if the material is thin films can affect the hardness value (Rother & Dietrich, 1994). Nanoindentation results were evaluated with this information in mind.

For Al<sub>50</sub>Ti<sub>50</sub> based samples (5050-ref, 50505-1, 50505-2 and 3), hardness and elastic modulus values were getting higher as the amount of W increased. H/E ratio is related to the wear performance of thin films (Leyland & Matthews, 2004). Wear performance of these samples was better from 0 to 4 at. % of W. However, this value tends to decrease with increasing W content from 4 to 8 at. %. Another parameter related to the plastic deformation is  $H^3/E^2$ , which increases with increasing W amount. There are two important parameters: W content and nitride formation. According to nanoindentation results, the mechanical properties were improved with increasing W content. Unfortunately, these samples were not fully nitrated; thus, the mechanical properties of the hard coatings were not as desired due to the low percentage of nitride formation (see Table 5). Grain sizes were close to each other, and it can not say something about the role of grain size on mechanical properties.

For Al<sub>67</sub>Ti<sub>33</sub> based samples (6733-ref., 6733-1, 6733-2), hardness values did not change with increasing W amount, and elastic modulus first decreased from 0 to 4.% W and second increased again from 4 to 5 at.% W. This strange behavior was evaluated in detail for fracture toughness measurement. Generally, hardness and elastic modulus decreased after the addition of W. The best H/E and  $H^3/E^2$  values belonged to the 6733-1 sample, with four at.% W. When 5050 and 6733 samples were compared, Al amount increased, incredibly elastic modulus and  $H^3/E^2$

increased, too. The best wear performance and plastic deformation values belonged to 6733-1 sample, and increasing wear performance with increasing Al content agrees with the literature (Bobzin, 2017; Hörling et al., 2005; Leyland & Matthews, 2000; Xu et al., 2017).

For Al<sub>50</sub>Cr<sub>50</sub> based samples (AlCr-ref, AlCr-1, and AlCr-2), hardness and elastic modulus were getting better with the addition of W. According to Table 6, H/E and H<sup>3</sup>/E<sup>2</sup> values were also improved. ~3 at.% W increased wear performance by almost 1.3 and plastic deformation value 2.3 times. The best improvement belonged to AlCr based samples in all samples.

When all samples were compared, some parameters should be explained: The first one is Al amount in the materials. Ti-Al-N-based coatings have a limit for aluminum content, which is about 65%. Higher Al content results in the formation of hexagonal structure, which results in undesirable mechanical performance. However, for CrN-based coating, there is no change in the crystal structure due to the high aluminum amount. Due to this reason, AlCrN coatings can have better mechanical properties (Mo & Zhu, 2008).

The third parameter is the crystalline size of the coatings, as known hardness is defined as the resistance of a material to plastic deformation. Generally, plastic deformation is related to dislocation. If dislocation motion decreases, the hardness of the material will be better. It is called hardening. Several strengthening mechanisms are effective on the hardening ceramic coatings: (i) grain size refinement, (ii) grain boundary reinforcement, (iii) solid solution hardening, (iv) multilayer hardening (Musil, 2012; H. Hahn et al., 1997).

Crystalline size is almost the same for Al<sub>50</sub>Ti<sub>50</sub> and Al<sub>50</sub>Cr<sub>50</sub> based samples, but the crystalline size of Al<sub>67</sub>Ti<sub>33</sub> samples was lower than the others. The hardness of 6733-ref. The specimen is higher than the 5050-ref. and AlCr-ref. ones. It can also be explained by its smaller crystalline size.

The effect of crystalline size will also be mentioned in the next chapter, related to the production and characterization of hard coatings by the cathodic arc evaporation technique.

Table 6. Summary of mechanical properties of samples after nanoindentation.

<b>Sample Name</b>	<b>grain size (nm)</b>	<b>W (at. %)</b>	<b>H (GPa)</b>	<b>E (GPa)</b>	<b>H/E</b>	<b>H<sup>3</sup>/E<sup>2</sup></b>
5050-ref.	27	0	6.36	150.9	0.0421	0.0113
5050-1	26	3.5	6.97	157.1	0.0444	0.0137
5050-2	25	4	7.31	157.3	0.0464	0.0158
5050-3	27	8	10.7	260	0.0412	0.0181
6733-ref.	16	0	9.3	210	0.0429	0.0165
6733-1	16	4	8.8	185	0.0486	0.0213
6733-2	16	5	8.4	200	0.045	0.0182
AlCr-ref	29	0	6.7	190	0.0353	0.0083
AlCr-1	25	2.5	8	192	0.0417	0.0139
AlCr-2	26	3.5	9	195	0.0462	0.0192

Figures 20, 21, and 22 show the mechanical properties of the three different coatings: Al<sub>50</sub>Ti<sub>50</sub> based, Al<sub>67</sub>Ti<sub>33</sub> based, and Al<sub>50</sub>Cr<sub>50</sub> based. It can be seen that a small amount of W improved the mechanical properties of the hard coatings, although they were not fully nitrided coatings.

According to Figure 20, the highest hardness and elastic modulus belonged to 5050-3 samples which included the highest W amount for Al<sub>50</sub>Ti<sub>50</sub> based coatings. However, the best wear performance belonged to 5050-2 samples which have four at. % W due to best H/E (plasticity index).

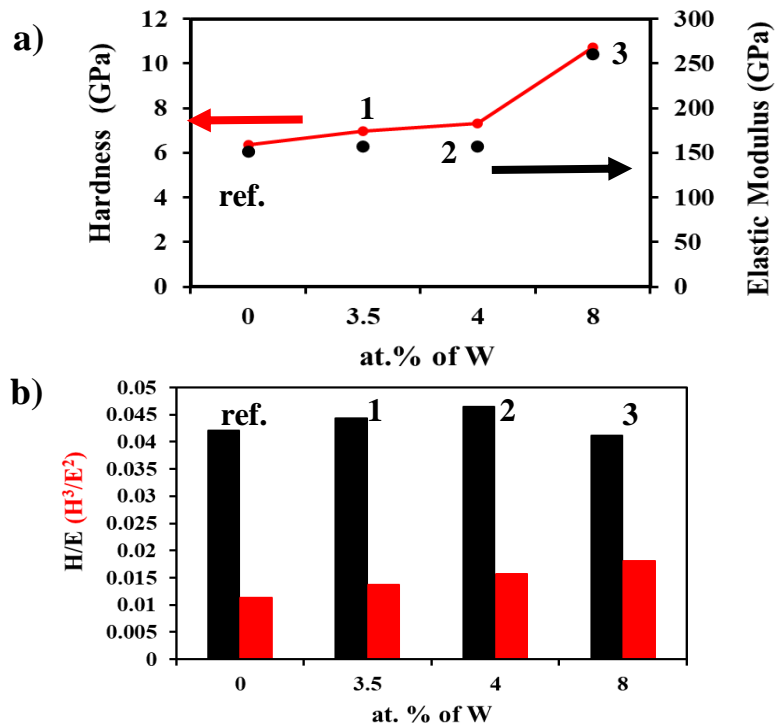


Figure 20. a) H and E vs. W amount and b) H/E and H<sup>3</sup>/E<sup>2</sup> vs. W amount for Al<sub>50</sub>Ti<sub>50</sub> based coatings. (data for 5050-ref., 5050-1, 5050-2, and 5050-3, respectively.)

According to Figure 21, it can be seen, 4 and 5 at % W were not effective on the hardness. However, 4 at% W showed the highest elastic modulus. The plasticity index (H/E) and plastic deformation (H<sup>3</sup>/E<sup>2</sup>) belonged to this sample 6733-1.

According to Figure 22, ~ 3 at. % W was effective on the hardness and elastic modulus. Additionally, H/E and H<sup>3</sup>/E<sup>2</sup> values are improved by a small amount of W.

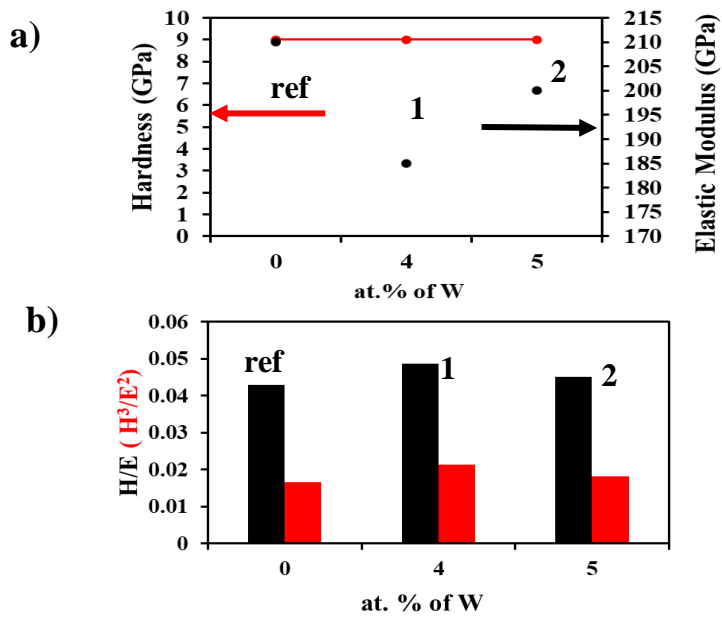


Figure 21. a) H and E vs. W amount, and b) H/E and H<sup>3</sup>/E<sup>2</sup> vs. W amount for Al<sub>67</sub>Ti<sub>33</sub> based coatings (data for 6733-ref., 6733-1, and 6733-2, respectively).

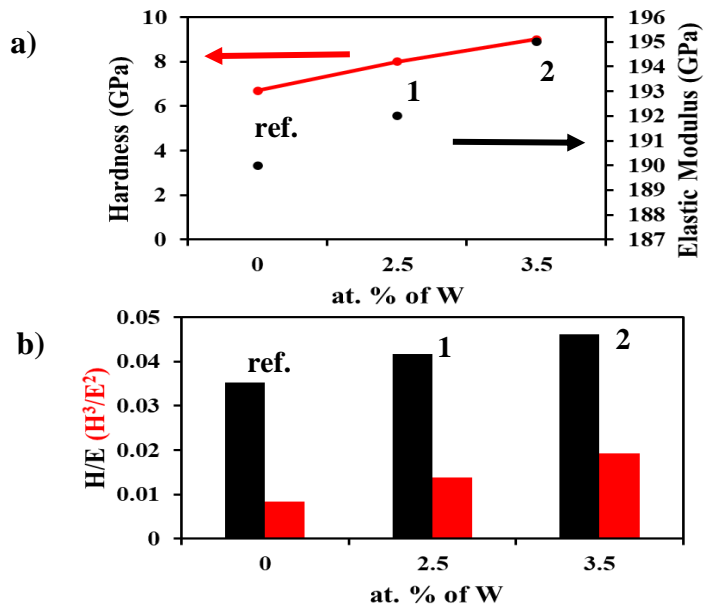


Figure 22. a) H and E vs. W amount and b) H/E and H<sup>3</sup>/E<sup>2</sup> vs. W amount for Al<sub>50</sub>Cr<sub>50</sub> based coatings. (data for AlCr-ref., AlCr-1 and AlCr-2, respectively.)

After nanoindentation, another mechanical property which is fracture toughness, was measured. The crack sizes were measured by using SEM and determined by the Image J software package. Figure 23 shows an example SEM image and associated crack sizes of Al<sub>50</sub>Ti<sub>50</sub> based sample (5050-ref).

C<sub>1</sub>, C<sub>2</sub>, and C<sub>3</sub> are cracks at the corner of the indents. All of them were measured for every sample. 15 nanoindentation tests are applied for every sample. It is difficult to see these cracks under SEM, and it takes so much time. Thus, all indents were not found under SEM; 10/15 indents were found for specimens. Fracture toughness was determined by using H, E, E/H, crack size, and Eq. 1.

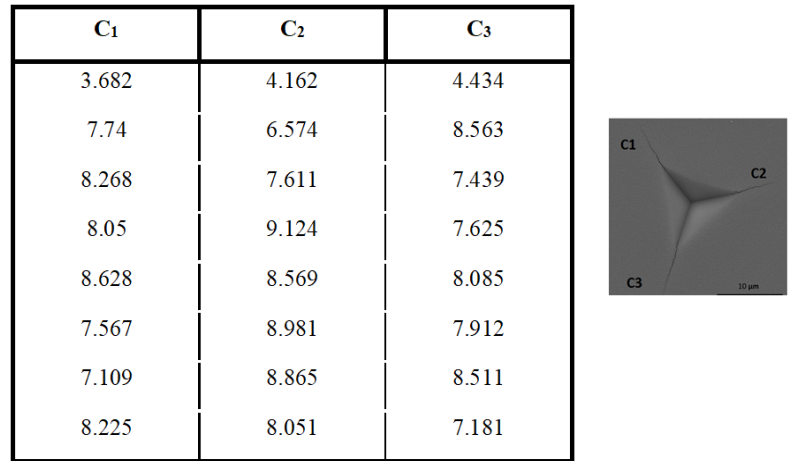


Figure 23. An example of crack size measurements (in μm) for Al<sub>50</sub>Ti<sub>50</sub> based sample and a representative SEM image.

Figure 24 shows SEM images of reference samples. Figure 24. (a) shows indentation images for 5050 based samples; a<sub>1</sub>) 5050-ref., a<sub>2</sub>) 5050-1, and a<sub>3</sub>) 5050-3, respectively. (b) shows for AlCr based samples; b<sub>1</sub>) AlCr-ref., b<sub>2</sub>) AlCr-1 and b<sub>3</sub>) AlCr-2, respectively. (c) shows for 6733 based samples; c<sub>1</sub>) 6733-ref., c<sub>2</sub>) 6733-1 and c<sub>3</sub>) 6733-2. First of all, a comparison between crack sizes of reference samples showed the biggest cracks belonged to Al<sub>50</sub>Ti<sub>50</sub> based coatings, and the smallest one

belonged to  $Al_{50}Cr_{50}$  based coatings. The largest crack size belonged to 5050-ref. sample and there is no crack for 5050-1 and 5050-2 samples (not shown SEM in figure 24), although they have 3.5 and 4 at.% W, respectively. However, 5050-3 samples, which includes 8 at.% W, had smaller cracks than 5050-ref. sample. Thus, we can conclude that crack size decreased due to W addition in the coatings.

SEM images of 6733 samples showed that cracks could be seen for every sample. However, when W amount increased from zero to 5 at.% crack sizes decreased, this is expected and desired results for the aim of the study.

However, AlCr based samples showed reversed results. Crack size increased due to W addition in the coatings. The numerical results for fracture toughness determination were discussed below.

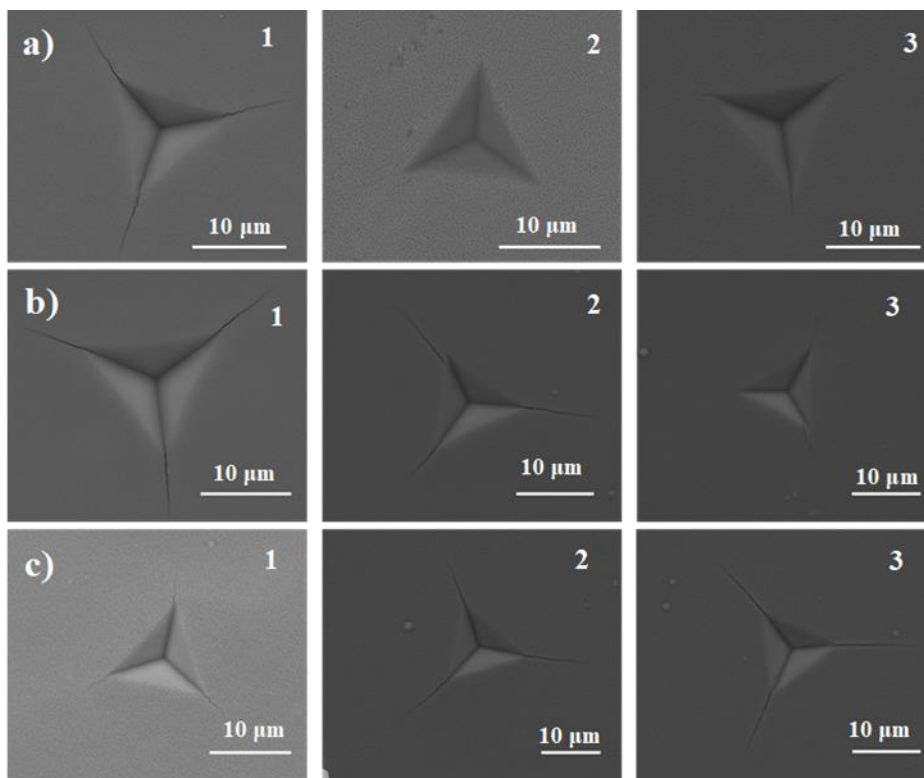


Figure 24. SEM images of a) 5050-ref, 5050-1, 5050-3, b)6733-ref, 6733-1, 6733-2, c) AlCr-ref, AlCr-1, AlCr-2 (from left to right) after nanoindentation.



The fracture toughness of all coatings was determined after nanoindentation and SEM analysis. Equation 1 was used to get these results. All of them were listed in Table 7. The general idea about this concept small crack size means high fracture toughness. For  $\text{Al}_{50}\text{Ti}_{50}$  based coatings, W improved the hardness and also fracture toughness. That means we simultaneously got high toughness and fracture toughness, although low nitride and low W amount. W addition increased the fracture toughness almost four times. These results were in agreement with theoretical studies. There are no detailed experimental studies about W-added AlTiN hard coatings that are produced by magnetron sputtering.

For  $\text{Al}_{67}\text{Ti}_{33}$  based coatings, 4 at.% W was a threshold value, and for higher W additions, fracture toughness decreased once again. For these samples, there may be a crack separation through the interface between the film and the substrate due to the limited adhesion between the coating and the substrate (Rother & Dietrich, 1994). Such behavior might have resulted in erroneous predictions of fracture toughness through indentation marks.

To gain further insight into the problem, load-displacement curves were closely examined. Some regions of the loading curve had pop-out parts (see figure 25) indicative of crack propagation. If there were no pop-out parts in load-displacement curves, Differential Load Feed (DLF) analysis would be applied to understand stress, adhesion behavior of the interface between coating and substrate (Rother & Kazmanli, 1998).

When it comes to the  $\text{Al}_{50}\text{Cr}_{50}$ -based coatings, the results were somewhat mixed. Hardness increased upon W additions. However, elastic remained the same. Overall, W additions resulted in a decrease in the fracture toughness. For ~3 at.% W, the fracture toughness decreased almost 11 times. This behavior might be attributed to the already high toughness of AlCr, and it can be speculated that the W additions distorted the lattice structure, and the lattice strains promoted cracking.

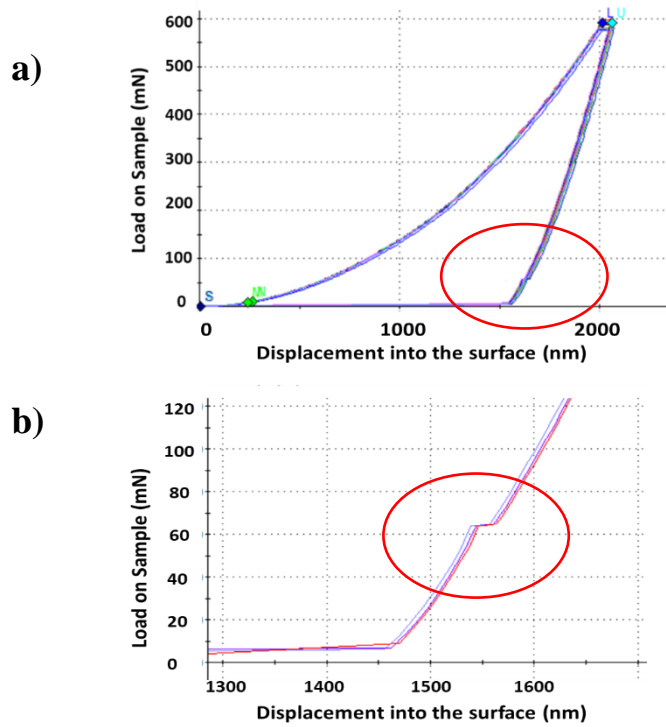


Figure 25. a) The load-displacement curve for 6733-1 sample, b) zoomed region to show pop-out parts in the load-displacement curve.

6733 based coatings showed almost the same hardness values after the test. Nanoindentation results were evaluated in detail. In Nanosuite program, raw nanoindentation data were analyzed to eliminate substrate effect on hardness values. CSM method was used to determine hardness and elastic modulus values. Indentation depth range was chosen at 100-300 nm to measure at a depth of 10% of film thickness which was  $\sim 3\mu\text{m}$ .

Table 7. Fracture toughness measurement results for all specimens.

Sample Name	W at.%	H (GPa)	E (GPa)	E/H	crack size ( $\mu\text{m}$ )	$K_{IC}$ $\text{MPa}\sqrt{\text{m}}$
5050-ref.	0	6.4	150.9	23.73	8.03	2.22
5050-1	3.5	6.9	157.1	22.54	No crack	-
5050-2	4	7.3	157.3	21.52	No crack	-
5050-3	8	10.7	260	24.29	3.43	8.03
6733-ref.	0	9.3	210	23.33	4.15	5.91
6733-1	4	8.8	185	20.56	8.8	1.80
6733-2	5	8.4	200	22.22	4.61	4.93
AlCr-ref	0	6.7	190	28.36	2.89	11.22
AlCr-1	2.5	8	192	24	11.24	1.34
AlCr-2	3.5	9	195	21.67	13.65	0.96

### 2.3 Conclusions

In this study, the production of hard coatings by using Magnetron sputtering and characterization of these thin films, both structural and mechanical, were explained. There is a gap about the refractory element, especially W added magnetron sputtering hard coatings and fracture toughness evaluation of these materials in the literature. The main research topic is this thesis fracture toughness improvement of refractory element (W) added hard coatings that produced magnetron sputtering.

Nitride formation is an essential parameter of the mechanical properties of hard coating materials. In this study, hard coatings were not fully nitrated due to some technical problems. However, it has been found that partially nitrated coatings are the subject of an increasing number of studies. In these structures, the nitride phase regions offer high hardness, while the metallic phases provide the desired high

ductility to the coating (Greczynski et al., 2016). The nanoindentation results of some nitrided samples showed lower hardness and elastic modulus values, as expected.

Using 2-8 at.% W alloyed metal nitrides showed different behavior.  $\text{Al}_{50}\text{Ti}_{50}$  based hard coating showed consistent results with the DFT studies, which are theoretical ones. The fracture toughness of these types of coatings showed the best fracture toughness improvement than the others, although they were not fully nitrided.  $\text{Al}_{67}\text{Ti}_{33}$  based hard coatings showed no interesting results. 5 at.% W was not enough amount to improve hardness, elastic modulus, and fracture toughness. Interestingly,  $\text{Al}_{50}\text{Cr}_{50}$  based material showed reversed results than the expected ones. Though W addition improved hardness and elastic modulus, fracture toughness was not improved.

## CHAPTER 3

### CATHODIC ARC EVAPORATED COATINGS

#### 3.1 Experimental Details

In this chapter, the industrial hard coatings coated using the cathodic arc evaporation technique were mentioned. These hard coatings were prepared by Ionbond Turkey (Bursa, Turkey) to compare with other hard coatings, which were coated by using Magnetron sputtering, and they were explained in the previous chapter. The company prepared two different types of hard coatings: (i) The routine (commercial) hard coatings and (ii) the nonroutine W/Mo added hard coatings.

These hard coatings were firstly characterized XRD, SEM, EDS, XPS. Then, Nnanoindentation was applied to get the hardness, elastic modulus, and fracture toughness of coatings. A novel mechanical test, a microcantilever bending test, was applied to get fracture toughness. Wear and drilling tests were used to understand these commercial and noncommercial hard coatings' wear behavior.

##### 3.1.1 Sample Preparation

The coating temperature was generally  $\sim 450^{\circ}\text{C}$  for the routine hard coatings. A Crosscut system was used for AlCrN based coatings, and maximizer and optimizer plus systems were used for AlTiN based coatings. The maximizer system is used to get thicker coatings. Optimizer plus and crosscut systems are standard systems for AlTi based and AlCr based coatings, respectively. However, the process details could not be explained due to the company policy, confidential information. Experimental details for routine hard coatings were listed in Table 8.

Table 8. Sample details of routine hard coatings by Ionbond Turkey.

<b>Sample Name</b>	<b>Composition of Sample</b>	<b>Coating system</b>	<b>Thickness (µm)</b>
Al50Ti50	(Al <sub>50</sub> Ti <sub>50</sub> )N	Optimizer plus	3
maxAl50Ti50	(Al <sub>50</sub> Ti <sub>50</sub> )N	maximizer	3.5
Al67Ti33	(Al <sub>67</sub> Ti <sub>33</sub> )N	Optimizer plus	3
maxAl67Ti33	(Al <sub>67</sub> Ti <sub>33</sub> )N	maximizer	3.5
Al50Cr50	(Al <sub>50</sub> Cr <sub>50</sub> )N	crosscut	3
Al64Cr36	(Al <sub>64</sub> Cr <sub>36</sub> )N	crosscut	2.5

Hauzer RTC 850 cathodic arc evaporation system was used to obtain nonroutine hard coatings. This system is more suitable than the standard systems such as optimizer plus, crosscut for non-routine ones. Figure 26 shows Huazer RTC 850 cathodic arc evaporation system in Ionbond Company and used TiAlW alloy cathodes. Nine cathodes are used in this system. The number of cathodes for main structure materials such as AlTi, AlCr decreased from nine to lower one to increase added refractory elements, which is Mo (3 pieces) in the main structure, for example; nine cathodes for reference sample (without Mo), eight cathodes for main structure (AlTi/AlCr) one cathode for Mo.

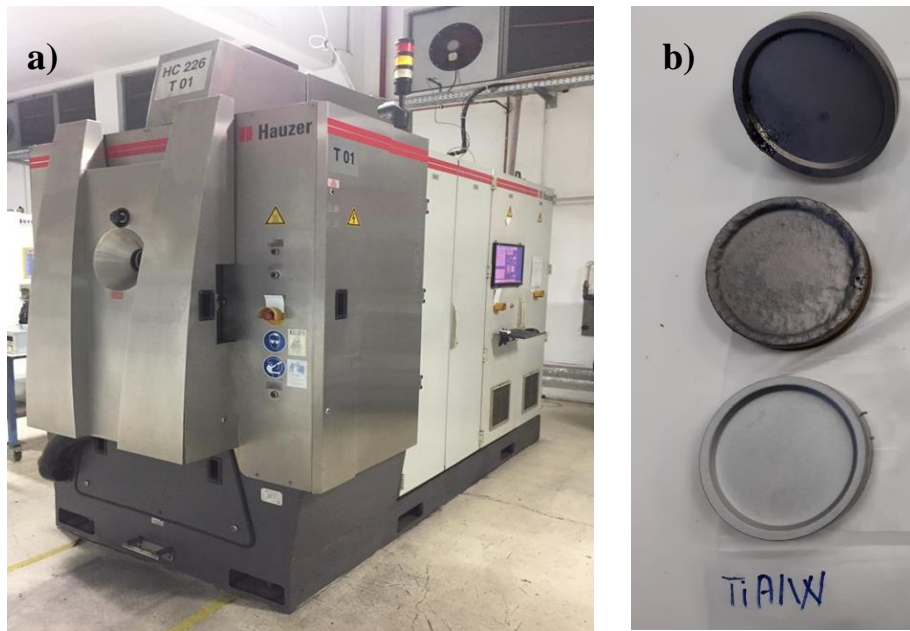


Figure 26. Photograph of a) Hauser RTC 850 Cathodic arc evaporation systems and b) TiAlW alloy cathodes.

Ti<sub>35</sub>Al<sub>35</sub>W<sub>30</sub> (at.%) alloy targets (3 pieces) were used for W-added hard coatings. Three of them were used at the same time to get desired W content in all W-added hard coatings' production processes. Process temperature was constant at 450°C. The duration was 101 minutes for AlCr based coatings, and Mo cathodes were run at the last 20 minutes of 101 minutes. The duration was 70 minutes for AlTi based coatings, and Ti<sub>35</sub>Al<sub>35</sub>W<sub>30</sub> cathodes were run at the last 20 minutes of 70 minutes. The used cathodes dimensions were 63 mm diameter and 15 mm thickness. Coating details of nonroutine hard coatings were listed in Table 9. 2 major structures were produced: AlTi based and AlCr based. AlTi based coatings have two different Al content. Ti<sub>35</sub>Al<sub>35</sub>W<sub>30</sub> cathodes were used to get (Al<sub>50-x</sub>Ti<sub>50-y</sub>W<sub>x+y</sub>)N and Al<sub>67</sub>Ti<sub>33</sub>, and pure Mo cathodes were used to get high Al content nitrides. Al<sub>64</sub>Cr<sub>36</sub> and pure Mo cathodes were used to get (Al<sub>64-x</sub>Cr<sub>36-y</sub>Mo<sub>x+y</sub>)N. There were some technical problems during the coatings. The evaporation of these refractory elements was more complex than the other elements due to high evaporation temperature. Generally, the surface

area of cathodes is wider than lab-scale coating systems for refractory elements due to high evaporation temperature and current values. Usually, the current values are 50-80 A to evaporate Zr, Nb, Ta. Additionally, increasing the cathode dimensions increases the cost of targets. The smaller cathodes are used in Hauzer RTC 850 systems, and coatings outcomes decrease. So, this system was chosen due to these reasons. However, Mo and especially W evaporation is new for the company, and they have no more experiences evaporation of W and Mo. Technical problems in the device were observed due to the ratio between high evaporation current and small cathodes surface area. The system shut itself down automatically due to these problems. Thus, both desired content of the element and thicker films could not be obtained.

Table 9. Experimental details for nonroutine hard coatings.

Sample Name.	Used cathodes	#of used cathodes	current (A)
Al <sub>50</sub> Ti <sub>50</sub>	Al <sub>50</sub> Ti <sub>50</sub>	9	60
Al <sub>50</sub> Ti <sub>50</sub> -W-1	Al <sub>35</sub> Ti <sub>35</sub> W <sub>30</sub>	6: AlTi	AlTi: 60, AlTiW: 110
Al <sub>50</sub> Ti <sub>50</sub> -W-2	Al <sub>35</sub> Ti <sub>35</sub> W <sub>30</sub>	3:AlTiW	
Al <sub>67</sub> Ti <sub>33</sub>	Al <sub>67</sub> Ti <sub>33</sub>	9	60
Al <sub>67</sub> Ti <sub>33</sub> -Mo-1	Al <sub>67</sub> Ti <sub>33</sub> and pure Mo	6: AlTi 3:Mo	AlTi: 60, Mo: 160
Al <sub>67</sub> Ti <sub>33</sub> -Mo-2	Al <sub>67</sub> Ti <sub>33</sub> and pure Mo	6: AlTi 3:Mo	AlTi: 60, Mo: 160
Al <sub>64</sub> Cr <sub>36</sub>	Al <sub>64</sub> Cr <sub>36</sub>	9	60
Al <sub>64</sub> Cr <sub>36</sub> -Mo-1	Al <sub>64</sub> Cr <sub>36</sub> and pure Mo	6: AlTi 3:Mo	AlCr: 60, Mo: 150
Al <sub>64</sub> Cr <sub>36</sub> -Mo-2	Al <sub>64</sub> Cr <sub>36</sub> and pure Mo		AlTi: 60, Mo: 160



### **3.1.2 Microstructural Characterization**

Several characterization techniques were used to understand the specimens' crystal structure, morphology, and elemental composition before evaluating their mechanical behavior. These analysis methods were X-Ray Diffraction (XRD), Scanning Electron Microscopy (SEM), Energy-Dispersive X-ray Spectroscopy (EDS/EDAX), X-ray photoelectron spectroscopy (XPS), Focused Ion Beam (FIB). Each of these was briefly explained in the previous chapter (2).

#### **3.1.2.1 X-ray Diffraction (XRD)**

This characterization method was also used to understand the routine and nonroutine hard coatings' crystal structure. A Rigaku Ultima-IV diffractometer (Central Laboratory in METU) was used for XRD analysis in grazing incidence mode at  $1^\circ$ . The grain size was measured using the Scherrer equation by using MDI Jade software. Copper wavelength ( $K\alpha$ ) is  $1.5418 \text{ \AA}$ .  $20-90^\circ$  was the  $2\theta$  range.

#### **3.1.2.2 Scanning Electron Microscopy (SEM) & Energy Dispersive X-ray Spectroscopy (EDS)**

Scanning electron microscopy is used to understand the surface morphology (shape and size), topography (surface features), crystallographic information (atoms arrangement), and elemental composition of the routine and nonroutine hard coatings. Elemental composition was determined by using EDS. All analyses were done in Central Laboratory in METU. All films were analyzed under high vacuum SEM, and they were coated with a few nm of Au-Pd to increase conductivity before surface imaging. All images were taken at the same accelerating voltage (30 kV), spot size (4.0), and magnification (10000X).

### **3.1.2.3 X-ray Photoelectron Spectroscopy (XPS)**

X-ray photoelectron spectroscopy (XPS) analyses electron emission of similar high energy. XPS can be used to measure the chemical or electronic state of surface elements, detect chemical contamination, or map the chemical uniformity of biomedical implant surfaces (Goldstein et al., 1992).

In this thesis, XPS analysis was used to understand the atomic structure and chemical bonding of N, Ti, Al, Cr, and W. Thermo Fischer with Al K $\alpha$  X-ray monochromatized sourced XPS device Bilkent University-UNAM was used, and spot size was 400  $\mu\text{m}$ . Before the measurement, the coating surface was bombarded with argon ions with an energy of 500 eV for 2 minutes at a medium current. Thus, the surface is etched up to 10 nm, preventing possible contamination from affecting the results.

### **3.1.3 Mechanical Characterization**

As mentioned before, micromechanical properties such as hardness, elastic modulus, fracture toughness are measured and evaluated using the nanoindentation technique. Additionally, micro-cantilever bending test and wear resistance test were applied for these coatings.

#### **3.1.3.1 Nanoindentation**

The mechanical properties were analyzed by the nanoindentation method. All steps were the same as Magnetron sputtering samples for routine and nonroutine hard coatings produced using cathodic arc evaporation.

### **3.1.3.2 Microcantilever Bending**

One of the novel parts of this thesis is measuring fracture toughness by a very new and unique method called micro-cantilever bending.

A new class of techniques has recently been developed to resolve some of the issues associated with indentation-based fracture toughness measurements of films. The methods generally use a nanoindentation system to apply force to and measure the displacements of micro-scale mechanical test specimens of various geometry produced by focused ion beam (FIB) milling. The specimen geometries used in these tests include single cantilever beams, clamped beams, double cantilever beams, membranes, and pillars. Different samples geometries for fracture toughness measurement were shown in Figure 27 (Jaya et al., 2015; Lawn et al., 1980).

It was mentioned before that the information related to the small-scale mechanical tests of hard coatings is quite limited (Roa et al., 2016). This is also true concerning fracture behavior of notched FIB-milled microcantilevers, one of this study's main subjects.

Fracture toughness measurement is a complex process, especially for thin films. Material properties, specimen preparation steps, specimen geometry, loading conditions are significant concerns for measuring fracture toughness. Critical load, crack dimensions, or fracture toughness value can be changed due to these reasons (Ast et al., 2019). Further complexities arise when considering the fracture process.

In the literature, there is no standard procedure for measuring fracture toughness of hard coatings in the micrometer range due to the lack of appropriate sample preparation and processing approaches. Standard methods can be classified as bending, buckling, indentation, scratching, and tensile testing. These methods are based on determining the critical applied stress where coating failure occurs, and in almost all of them, a coating/substrate compound is tested (Riedl et al., 2012).

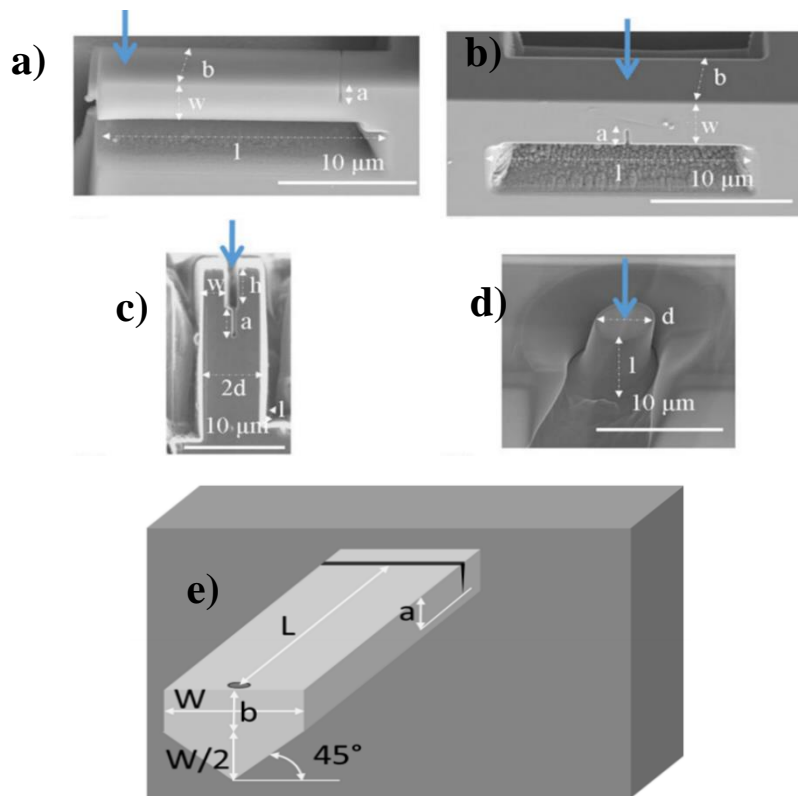


Figure 27. Selected samples with different geometries for fracture toughness testing at the small scale: (a) single cantilever bending, (b) clamped beam bending, (c) Double Cantilever bending, and (d) pillar splitting. All samples were prepared with FIB on Si(100) (Jaya et al., 2015). e) Schematic representation of the micro-cantilever bending geometry (Lawn et al., 1980).

Single cantilever bending (see Fig. 27(e)) is the most common fracture toughness test geometry that has been used at a small scale to date (Jaya et al., 2015). There are some steps to prepare a micro-cantilever:

1. Etching of coated Si (100) wafer with 30 wt% KOH to obtain free-standing coating regions.
2. FIB-milling to prepare cantilever as desired dimensions

These steps were explained in the following detailed parts.

### 3.1.3.2.1 Chemical Etching

Figure 28 shows a schematic representation of the chemical etching procedure. A single crystal (100) Si wafer was used as a substrate material. Specimens were etched in the cleanroom at The Center for Solar Energy Research and Applications (GÜNAM) in METU.

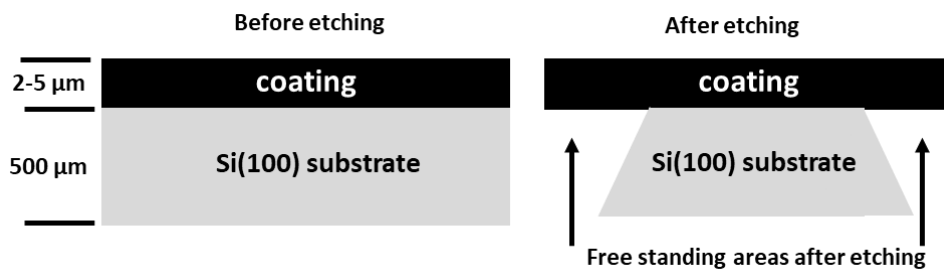


Figure 28. The schematic representation of the chemical etching procedure.

The chemical etching of silicon depends on crystal orientation, temperature, and concentration of the etchant. The geometry of the area to be etched also influences the etch rate owing to the different crystal planes encountered during the etching process. To decrease the effect of other chemicals on the etching mechanism, pure KOH solution has been preferred over several chemicals. KOH attracts the silicon preferentially in the  $\langle 100 \rangle$  plane producing an anisotropic V-etch with sidewalls that form a  $54.7^\circ$  angle with the surface (Alvi et al., 2008). Tetramethylammonium hydroxide (TMAH), potassium hydroxide (KOH), hydrofluoric acid (HF) are the most common etchants for Si and SiO<sub>2</sub> wafers. TMAH is more suitable for Complimentary Metal Oxide Semiconductor (CMOS) or Integrated circuits (IC), and HF is more dangerous and toxic than KOH (Rao et al., 2017). KOH was used as an etchant chemical for this study. Samples ( $\sim 1 \text{ cm} \times 1 \text{ cm}$  dimension) were kept in different potassium hydroxide (KOH) solutions in 15-minute steps for a total of 120 minutes. Then, samples were washed with deionized water, isopropyl alcohol,

deionized water, respectively. Finally, all samples were dried with nitrogen. An optical microscope was used for every step to see the surface of the specimen before and after the etching procedure.

Table 10 shows the details of the etching procedure. As a result of the experiments, The Si substrates were etched by 120 min in a 30 wt.% KOH solution heated to 60 °C. Figure 29 shows an SEM image of free-standing regions after the etching procedure. The shiny parts in the SEM image are free-standing regions.

Table 10. Experimental details of the etching procedure.

Trial	Duration (min)	Temperature(°C)	% wt. KOH
1	15, 20, 25	<b>60</b>	100
2	30, 60, 75, 90		60
3	45, 60, 75		<b>30</b>
4 & 5	60, 75, 90, <b>120</b>		30

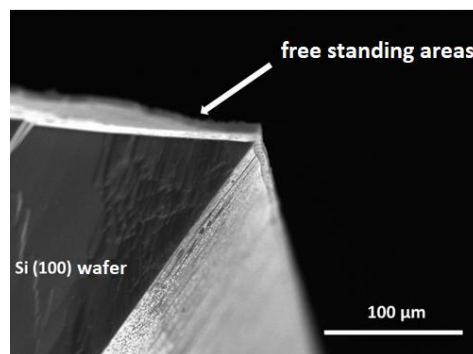


Figure 29. SEM image of coated Si (100) substrate to see free-standing areas after chemical etching. (Al<sub>50</sub>Ti<sub>50</sub>)N hard coating produced by cathodic arc evaporation was used.

### 3.1.3.2.2 Fabrication of Microcantilevers

Focused ion beam (FIB) milling is an attractive and new class technique to obtain micro/nanostructures for material science. It has been commercially available since the 1990s. Using this method, samples for Transmission electron microscopy (TEM) specimen for micro and nanomechanical tests or chip and semiconductor structures can be prepared. An accelerated  $\text{Ga}^+$  ion beam hits the sample surface and removes a small amount of the material from the surface. Spot size is generally 10 nm, and it works in a high vacuum ( $10^{-5}$  torr). There are several drawbacks of this FIB. The speed of this technique is quite low, and making a complex structure can take long hours by this technique, and it is expensive. However, the defects of the formed structures are few, and it is easy to obtain especially nano-sized structures by this technique. For mechanical evaluation, which is related to this thesis, microcantilevers and micropillars can be prepared by this method. Pt is generally used as a protection layer for sample preparation of crosssection or TEM applications. Figure 30 (a) shows a schematic of FIB milling (Munroe, 2009; Orloff, 2016; Yan & Takayama, 2020) and (b) shows a photograph of the focused ion beam located in Bilkent University-UNAM.

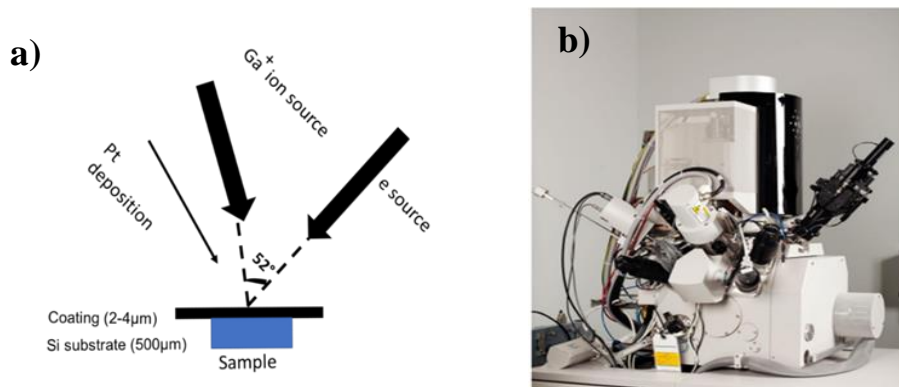


Figure 30. (a) A photograph of the focused ion beam located in Bilkent University-UNAM. (b) Schematic description of the FIB milling process.

It was mentioned before that a focused ion beam is used focused  $\text{Ga}^+$  ions to mill the material on the surface by scattering and provides the desired geometry with a resolution of up to 10 nm. The electron column on the device also acts as SEM and provides imaging without damaging the sample. Figure 31 shows an SEM image of the microcantilever after FIB milling.  $b$  is microcantilever thickness ( $\sim 2\text{-}4\ \mu\text{m}$ ),  $L$  is microcantilever length ( $\sim 10\text{-}20\ \mu\text{m}$ ), and  $a$  is the notch on the microcantilever.

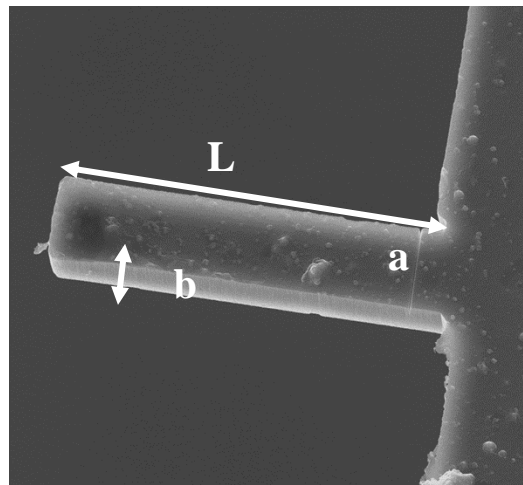


Figure 31. An SEM image of the microcantilever after FIB milling.

The FIB system provides currents ranging from 10 pA to about 50 nA, and the material processing speed is directly proportional to the current. On the other hand, as the current increases, focusing becomes more complex, and the processing precision decreases. For this reason, primarily rectangular areas were processed at currents around 10 nA. Between these rectangles, the beams are intended to remain. Then, the edges of the samples were smoothed with a beam at the level of 2-4 nA. Finally, a single line was machined on the upper surface of the coating using a current of 100 nA so that the notch needed for the fracture test was opened. Approximately one-fourth of the coating thickness is targeted for the depth of this notch. FIB trials were done either at Bilkent University UNAM or Hacettepe University Hunitek,



depending on the availability of the FIB equipment. Figure 32 shows some samples after FIB milling, and Table 11 lists the sample details shown in Figure 32. Sample No six was tested successfully. There were some reasons why the other test were not successfully: (i) Due to the high force applied by the nanoindentation device during the step of determining the sample height; all samples were broken in one go before they could be tested. (ii) During the first beam test, the device continued the displacement of the diamond tip with the sudden breaking of the beam. For this reason, the beams were repeatedly broken, so the obtained data was not significant. (iii) Micro-cantilevers were tested by remote control due to Pandemic; thus, it made the process difficult, and (iiii) some samples were broken during the shipment to İstanbul.

Table 11.Details of produced micro-cantilevers.

<b>Sample No</b>	<b>Material</b>	<b>FIB device</b>	<b>Width (µm)</b>	<b>Length (µm)</b>	<b>Thickness (µm)</b>
1	(Al <sub>50</sub> Ti <sub>50</sub> )N	Bilkent Uni.- UNAM	2	14	2
2	(Al <sub>50</sub> Ti <sub>50</sub> )N	Hacettepe Uni.-Hunitek	2	11.5	2
3	(Al <sub>50</sub> Ti <sub>50</sub> )N	Bilkent Uni.- UNAM	3	8	2
4	(Al <sub>50</sub> Cr <sub>50</sub> )N	Bilkent Uni.- UNAM	3-6	7	2
5	(Al <sub>50</sub> Ti <sub>50</sub> )N	Bilkent Uni.- UNAM	10	10	3
<b>6</b>	<b>(Al<sub>50</sub>Ti<sub>50</sub>)N</b>	<b>Bilkent Uni.- UNAM</b>	<b>5</b>	<b>25</b>	<b>3</b>

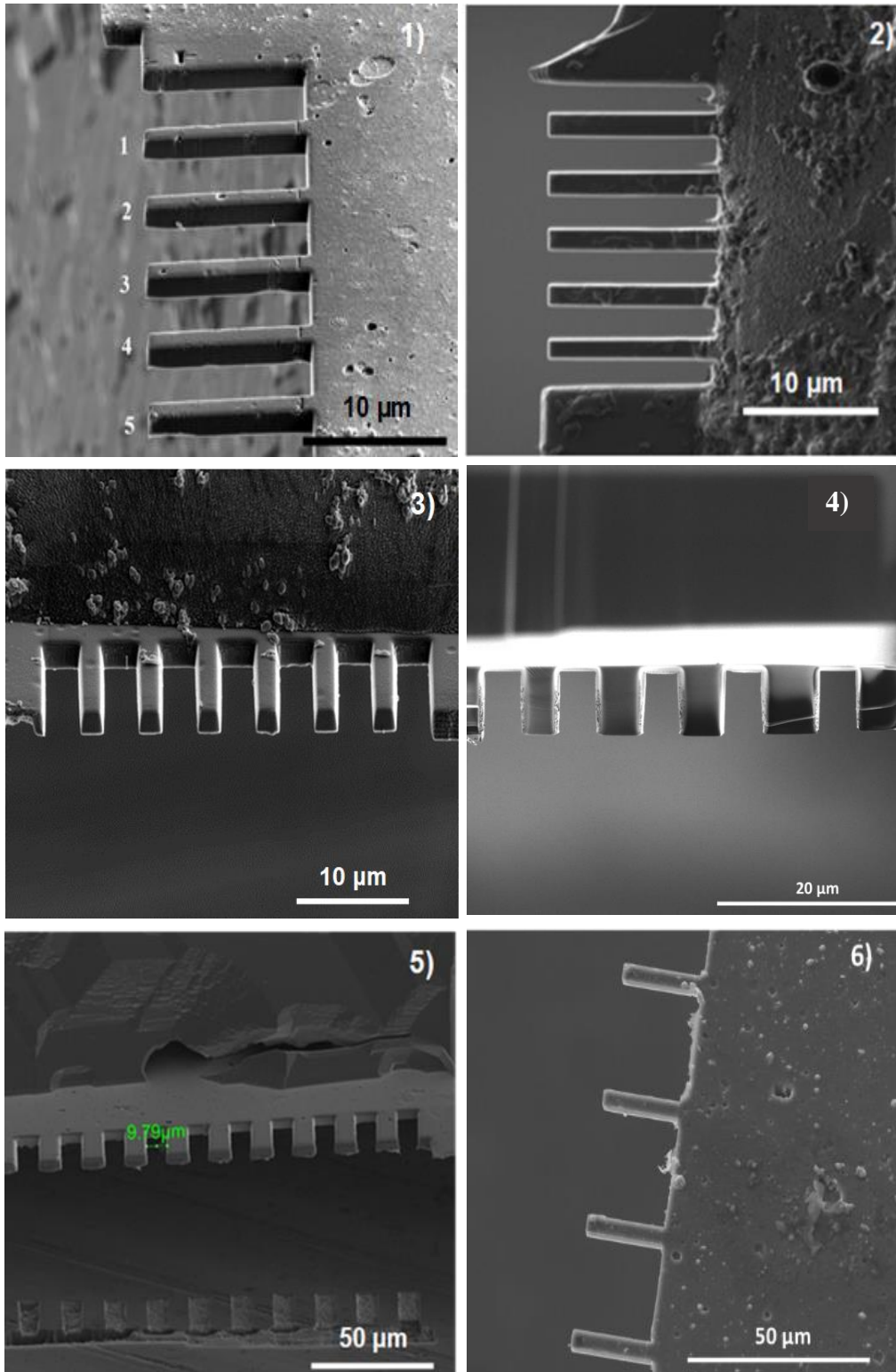


Figure 32. SEM images of prepared microcantilevers using FIB milling.

Equations 2 and 3 mentioned in chapter 1 were used to understand the fracture toughness of the hard coatings. Additionally, analyzing the linear part before proceeding to fracture toughness calculation will give preliminary information to confirm the accuracy of the results. The geometry in this scope corresponds to the loading made on the end of a rectangular cantilever structure. The displacement resulting from this loading can be written with the assumptions of linear elastic behavior and small displacement as follow:

$$\delta_{\max} = \frac{Pl^3}{3EI} \quad (6)$$

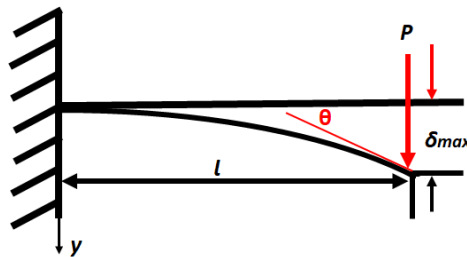


Figure 33. Schematic representation of beam bending (Beam Deflection Formulas, n.d.).

In equation (6),  $\delta_{\max}$  is the displacement at the free end,  $P$  is the load,  $l$  is the cantilever length,  $E$  is the modulus of elasticity, and  $I$  is the moment of inertia. SEM and the elastic modulus determined the relevant dimensions of the microbeams within the scope of nanoindentation measurements.

The FIB milling and testing of microcantilevers were very challenging experiments, and sometimes the specimens were not tested due to some difficulties. In light of all previous FIB and bending test experiments, these paths have been followed:

1. The device was used with the expert with special permission from UNAM management (external users are still not acceptable to the center due to the Pandemic).
2. Large gaps (25  $\mu\text{m}$ ) are left between samples to allow the diamond tip to test one cantilever at a time.
3. The sample sizes have been increased to see the samples more clearly in the nanoindentation device microscope.
4. While the sample is being shipped to Koç University, protective barriers were attached to the side of the sample so that they could be removed later (it is not possible to use the indenter device in the presence of such protrusions, protective barriers have been designed so that they could be removed without any damage to the sample)
5. To minimize the progress of the diamond tip after the sudden breaking of the beam, a displacement-controlled method code was prepared by connecting to the device at Koç University remotely, and the experiments were carried out with the remote-control method (Teamviewer software) with the support of the expert in Koç University.

### **3.1.3.3 Ball-on Disc Test**

The tribological behavior of the hard coatings can be analyzed using ball-on-disc or pin-on-disc tests at room and elevated temperatures. In this study, the pins and the discs were manufactured by Turkish Aerospace Industry A.Ş.(TUSAŞ), and alumina balls (10 mm diameter) were ordered from Antoon-Paar (Austria). High-Speed Steel (HSS) was used to be the material of pins and discs. Pin-on and ball-on discs tests were aimed first; however, the pin-on-disc test did not apply due to a flaw on the head of the pins from production problems. HSS discs were coated by Ionbond

Turkey company for tests at the same batch with the production of hard coatings on Si(100) substrates. All tribology tests were done in İTU. Figure 34 shows produced HSS pins and discs for tribology tests. 440C Stainless steel balls were also used to compare the behavior of coatings against the inert material (Alumina) and noninert material (440C SS). Table 12 shows the experiments' details for tribology tests.

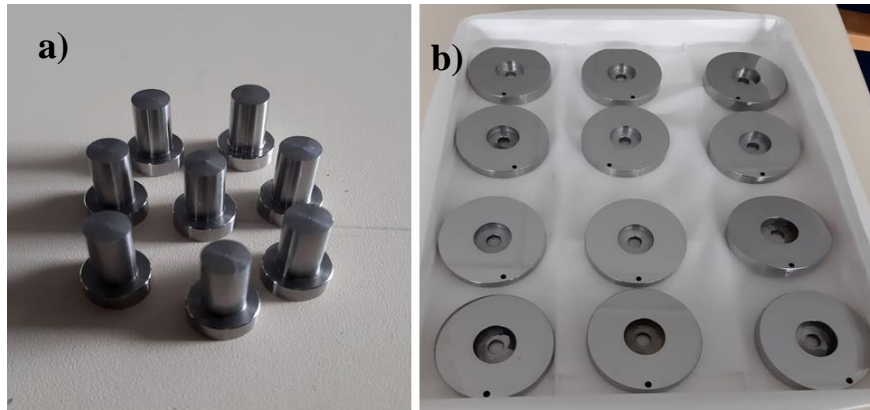


Figure 34. Produced HSS a) pins and b) discs for tribology tests.

Table 12. Details of the ball-on-disc test.

Device	CSM Tribometer
Temperature (°C)	25
Atmosphere	Air
humidity	%50
Load (N)	5
Velocity (cm/s)	3
Track radius (mm)	16
Ball diameter (mm)	10
Ball material	Al <sub>2</sub> O <sub>3</sub> and 440C SS

Wear rate calculated by using the following formula:

$$W = \frac{V}{LF_p} \quad (7)$$

As the volume loss  $V$  (mm<sup>3</sup>) per distance  $L$ (m) and the applied load  $F_p$  (N). Calculated wear rate values were listed in the results and discussion parts (Hagarová et al., 2018).

#### **3.1.3.4 Drilling Tests**

The turning and milling processes are the most used machining processes; however, the drilling process is quite relevant for the machining industry. These tests create the need for process improvement by reducing machining times, improving tool life, or applying new machining methods. Focusing on the tool-life or tool performance directly influences machining's productivity and cost (Sousa et al., 2021).

An essential part of today's machining operations is hole drilling operations. One of the most important targets of hole drilling is lower cost and better hole quality. Drill geometry, drilling speed, properties of the drilled material affect the results.

6mm HSS drilling tools (Makine Takım Endüstrisi A.Ş.) were used for real performance of the metal nitrides. These cutting tools were coated by Ionbond Turkey company. Yeter Savunma ve Havacılık company (Ostim,Ankara) helped us and Spinner MVC 1000 vertical machining center was used to test.1600 rpm spindle speed and 80 mm/min feed were test parameters. AISI 4140 Steel was used to be a drilling material. AISI 4140 Steel has high hardness and toughness. The cutting performance of HSS tools without any coating is low against AISI 4140 Steel. Therefore, coated tools were expected to show better performance during drilling. The thickness of the drilling material was 50 mm. Peck drilling method was applied

for tests. Seventy-five holes were opened for every drilling tool, and 375 cm of metal was drilled. SEM was used to see tools after 25 holes. Figure 35 shows a real image of the vertical machining center and drilling material.

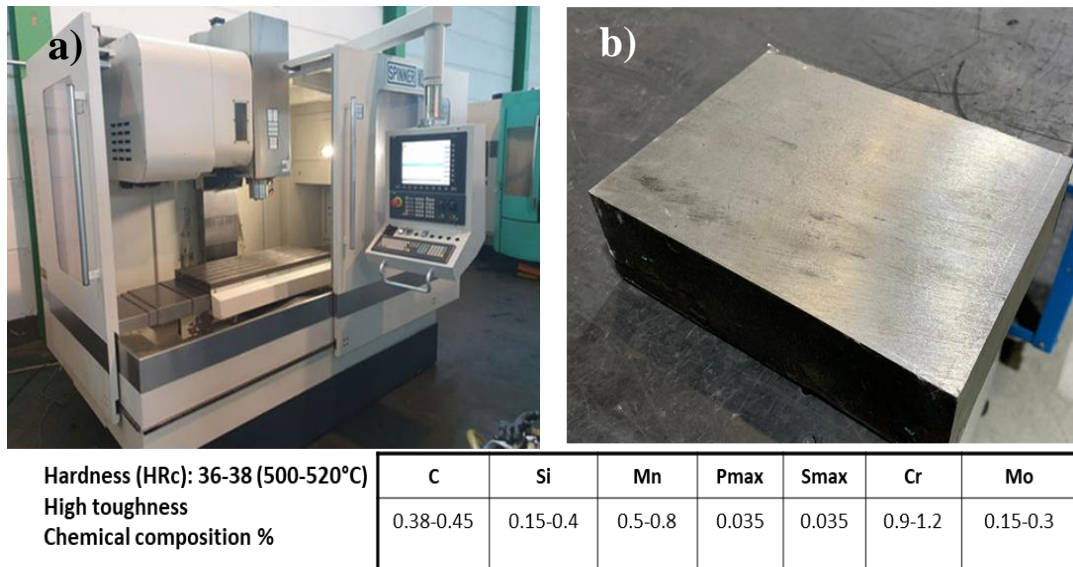


Figure 35. a) Vertical machining center, b) image and properties of AISI 4140 Steel during the test.

## 3.2 Results and Discussion

### 3.2.1 Microstructure

All samples were firstly characterized structurally by XRD and SEM&EDS techniques. The details of the experiments were mentioned in this part. All structural characterization was done at Central Laboratory in METU.

Figures 36 and 37 show XRD data of the AlTi based and AlCr based routine hard coatings, respectively. Step scanning was 1 °/min, and scans were run between 20°

to 90°. Structure data obtained by previous experimental were taken from the Inorganic crystal structure database (ICSD), and they were compared with the literature. Scherrer equation was applied by Jade MDI software to approximate the average crystal size in the films. The wavelength for Cu  $K\alpha$  is 1.5418 Å at 22.85°C. The glancing angle mode where the angle between the incoming beam and the sample surface was 1°. At. % of W and other elements were mentioned in EDS results which were below. Figure 38 shows example XRD patterns for AlTiN and AlCrN hard coatings produced by the same method. (Fan et al., 2017; Joo et al., 2009). Samples produced under different coating systems use different parameters during coating (details cannot be shared since they are commercial information) did not show additional data in the XRD results. Additionally, it can be said that the samples with high Al content have an amorphous structure. Finally, it was understood that the hexagonal AlN phase also appears with the increase in the Al ratio in the structure (Bobzin, 2017). It can be said that XRD patterns of AlTi based routine coatings were agreement in literature.

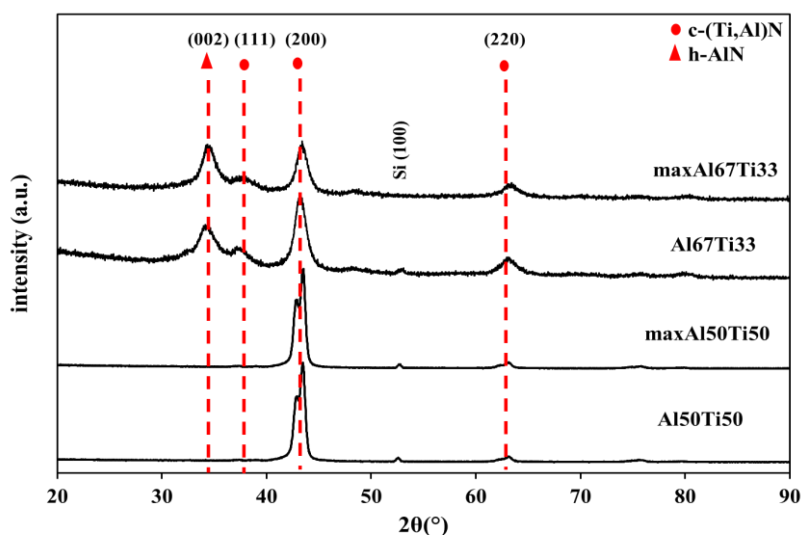


Figure 36. XRD results of AlTi based routine hard coatings.



The AlCr based coating, in addition to the nitride peaks, has a peak at  $55^\circ$ , and it belongs to aluminum oxide ( $\text{Al}_2\text{O}_3$ ). It is known that such partial oxidation increases the wear resistance of AlCrN coatings by increasing their hardness. (Chawla, 2013).

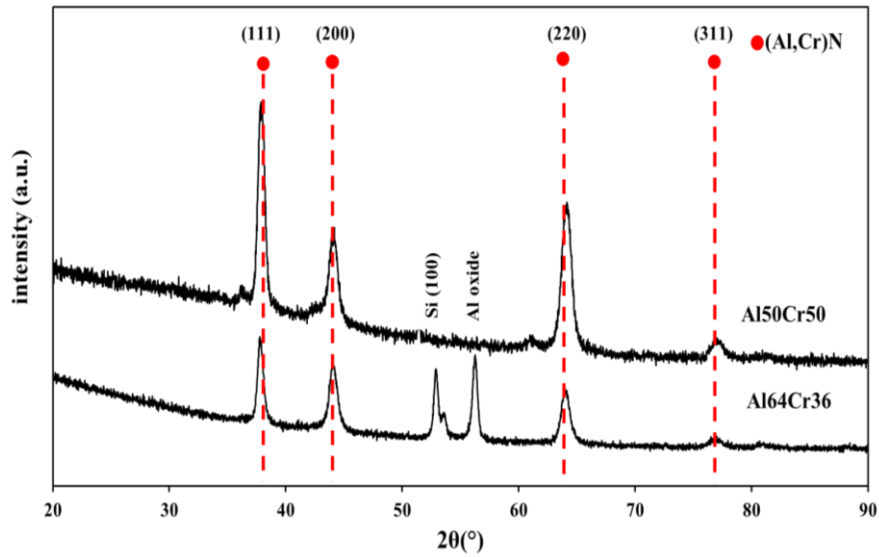


Figure 37. XRD results of AlCr based routine hard coatings.

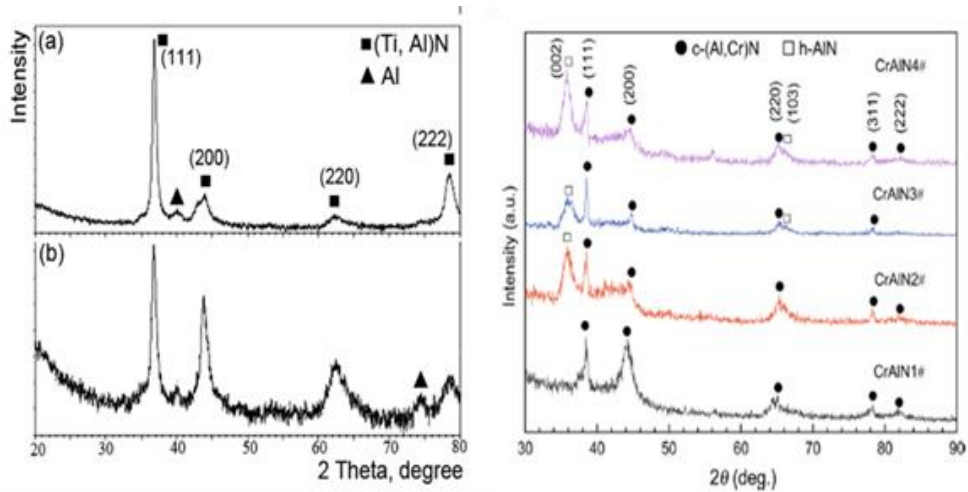


Figure 38. Example XRD data from the literature (Fan et al., 2017; Joo et al., 2009).

Figures 39 and 40 show XRD patterns of W-added and Mo-added AlTi based on routine hard coatings. With the addition of W and Mo to the AlTiN coatings, there was no significant change in the XRD patterns. There were very small shifts in the peak angles due to the variation in the mean interatomic distance experienced due to the different sizes of Mo and W atoms compared to Ti and Al atoms. Metallic W and Mo showed a small peak at  $40^\circ$ , and we can say that a small amount of tungsten was added to the structure as metallic.

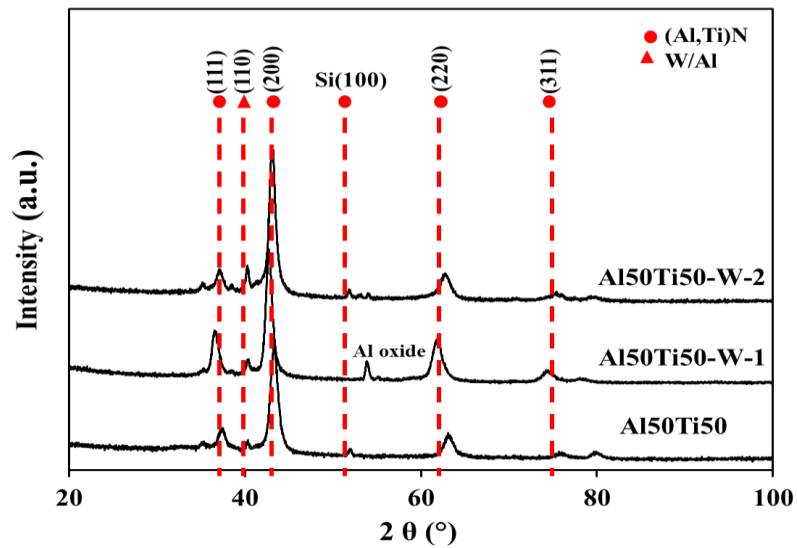


Figure 39. XRD Results of W- added AlTi based hard coatings.

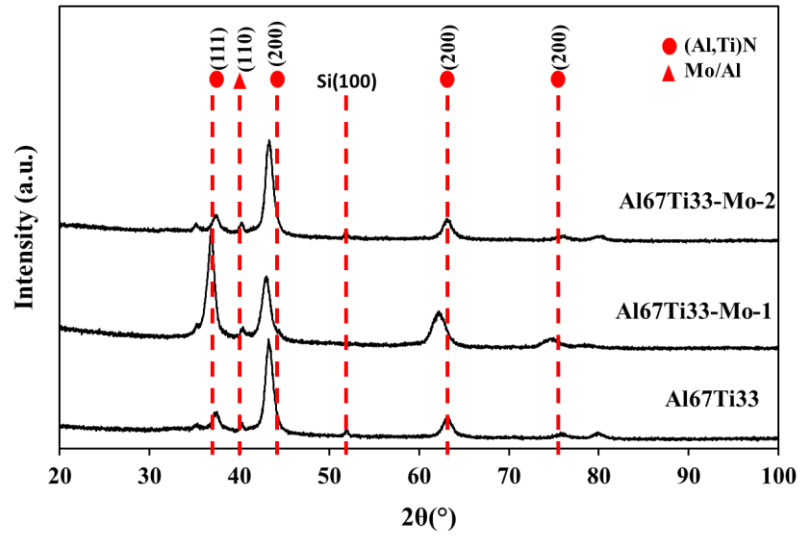


Figure 40. XRD patterns of Mo-added AlTi based hard coatings.

Figure 41 shows XRD patterns of AlCr based nonroutine hard coatings. Mo addition did not change the crystal structure of the coatings. Al<sub>64</sub>Cr<sub>36</sub>-Mo-2 sample has high Mo content, and this sample showed more amorphous peaks than others, and there was no metallic Mo in the structure.

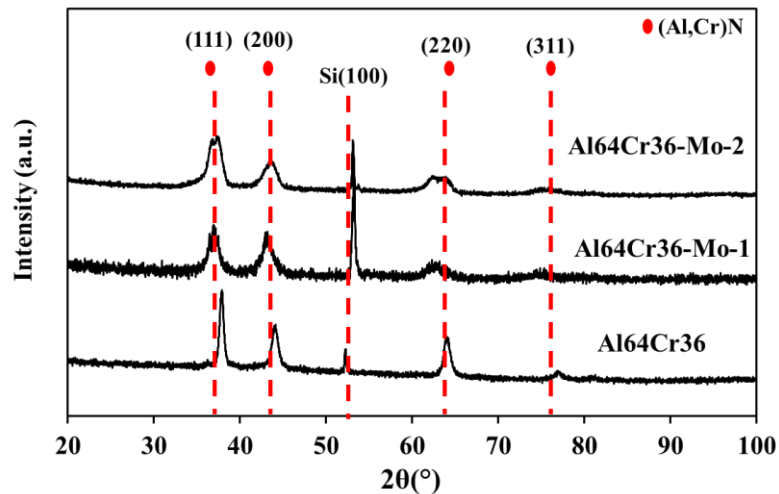


Figure 41. XRD results of Mo-added AlCr based hard coatings.

X-ray peak broadening analysis was used to evaluate the crystalline sizes and lattice strain by the Williamson-Hall (W-H) analysis (eq. 9). Scherrer Equation (eq. 5) was used to modify this formula. When Scherrer Eq. was used, the grain size was obtained smaller than 20 nm; however, the W-H plot or strain-size plot showed the grain sizes were larger than 20 nm. Figure 42 shows an example of XRD data taken from MDI Jade software and a strain-size plot. Tables 13 and 14 show the crystal size of the highest peaks for every sample for Scherrer eq. The average crystalline size for all peaks for the W-H equation. The typical crystal size in the literature is 5-15 nm (Sanchette et al., 2011). This difference could come due to internal stress in the materials, and the broadening of peaks could be affected by this stress. The relationship between grain size and mechanical properties were mentioned followed parts. Generally, the grain size of the routine and nonroutine hard coatings were close to each other. High Al included samples have a smaller crystalline size than the Al<sub>50</sub>Ti<sub>50</sub> based samples. When cathodic arc evaporation samples are compared with the magnetron sputtering samples, the higher hardness of CAE samples can be explained due to smaller grain sizes.

$$\beta_T = B + \beta_e \quad (8)$$

$$\beta_D = \frac{K\lambda}{D\cos\theta} \quad (5)$$

$$\beta_e = 4\varepsilon\tan\theta \quad (9)$$

$$\beta_T = \frac{K\lambda}{D\cos\theta} + 4\varepsilon\tan\theta \quad (10)$$

Where  $\beta_T$  is the total broadening,  $B$  is related to the peak broadening for Scherrer Eq.,  $\beta_e$  is strain broadening,  $\varepsilon$  is strain and  $\theta$  is peak angle ( $^\circ$ ).

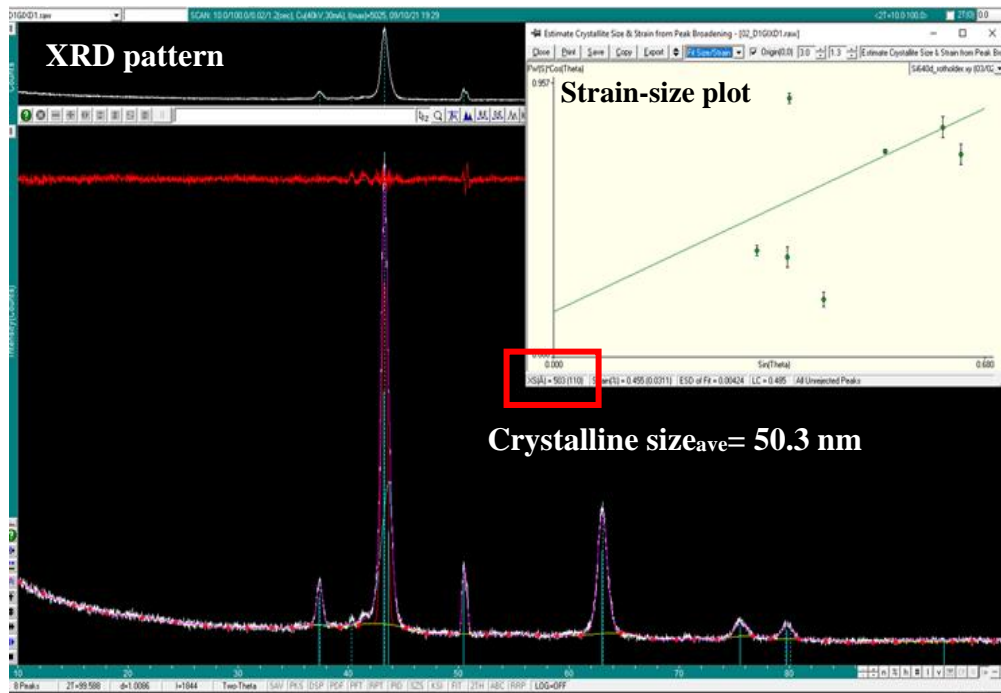


Figure 42. An example XRD pattern and strain-size plot for Al<sub>50</sub>Ti<sub>50</sub>-W-1 sample.

Table 13. Calculated grain size values of routine hard coatings.

Sample Name	Crystal size (nm)	
	Scherrer Equation (from highest peak)	W-H Equation (from every peak)
Al50Ti50	8.7	55.5
maxAl50Ti50	7.2	43.6
Al67Ti33	6.4	35.3
maxAl67Ti33	5.9	33.9
Al50Cr50	15.3	70.2
Al64Cr36	6.5	37.1

According to Table 14, Addition W increased the grain size for Al<sub>50</sub>Ti<sub>50</sub> based samples. However, for high Al included Al<sub>67</sub>Ti<sub>33</sub> and Al<sub>64</sub>Cr<sub>36</sub> based samples, the refractory element added a reversed effect on grain size. W-H Analysis gives more reliable data than Scherrer Equation for thin films with internal stress in the material. It was mentioned before, the film-substrate structure is a composite structure, and if they produced unstable systems such as CAE, they might be a stress interface between film and substrate. In this situation, the results of Scherrer may be affected by stress, and they might be less reliable.

Table 14. Calculated crystalline size of nonroutine hard coatings.

Sample Name	Crystal size (nm)	
	Scherrer Equation (from highest peak)	W-H Equation (from every peak)
Al <sub>50</sub> Ti <sub>50</sub>	8.3	45
Al <sub>50</sub> Ti <sub>50</sub> -W-1	10.8	50.3
Al <sub>50</sub> Ti <sub>50</sub> -W-2	10.4	48.2
Al <sub>67</sub> Ti <sub>33</sub>	10.1	52.1
Al <sub>67</sub> Ti <sub>33</sub> -Mo-1	7.8	40
Al <sub>67</sub> Ti <sub>33</sub> -Mo-2	5.9	30.3
Al <sub>64</sub> Cr <sub>36</sub>	15.9	63
Al <sub>64</sub> Cr <sub>36</sub> -Mo-1	4.9	28.9
Al <sub>64</sub> Cr <sub>36</sub> -Mo-2	8.5	39.7

The surface and thickness of the samples were analyzed under SEM. Figures 43 and 44 show the cross-section view and surface of some routine hard coatings. There was no evidence of the adhesion problem of coating on the substrate surface. However, surface roughness was higher than other samples produced by magnetron sputtering. We know the surface quality of cathodic arc evaporation thin films are worse than

magnetron sputtering. This worse surface quality affected the reliability of the mechanical results. It was also difficult to see cracks at the corner of the indents after the nanoindentation test under SEM. Droplets, textures on the surface made difficult the SEM analysis. Film thicknesses were measured by SEM and were listed in Table 8. These routine coatings thicknesses were more suitable than the nonroutine ones to make cantilever bending tests due to being thicker.

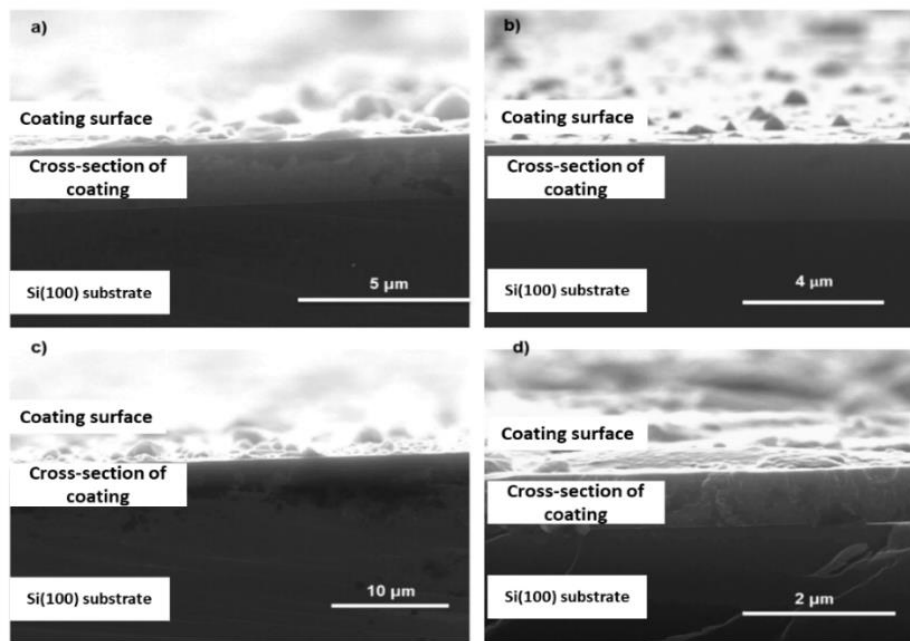


Figure 43. Cross-section SEM images of a)  $\text{Al}_{50}\text{Ti}_{50}$ , b)  $\text{maxAl}_{50}\text{Ti}_{50}$ , c)  $\text{maxAl}_{67}\text{Ti}_{33}$  and d)  $\text{Al}_{64}\text{Cr}_{36}$  routine hard coatings.

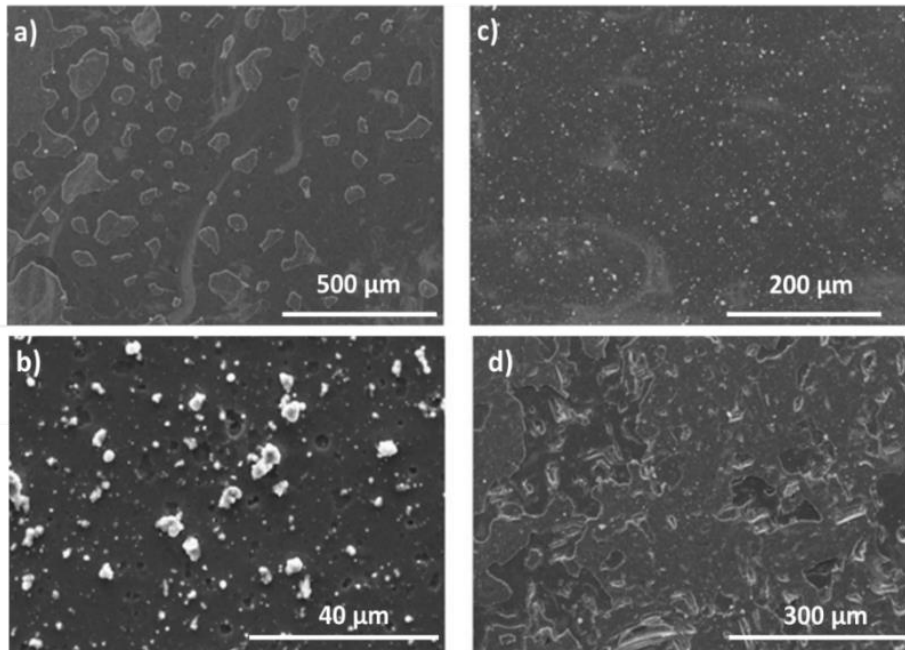


Figure 44. Surface SEM images of a)  $\text{Al}_{50}\text{Ti}_{50}$ , b)  $\text{maxAl}_{50}\text{Ti}_{50}$ , c)  $\text{maxAl}_{67}\text{Ti}_{33}$  and d)  $\text{Al}_{64}\text{Cr}_{36}$  routine hard coatings.

Figure 45 shows SEM images of nonroutine hard coatings. According to SEM images, the surface of hard coatings was rougher than hard coatings, produced by magnetron sputtering. This rough surface morphology is frequently observed in coatings obtained by the cathodic arc deposition method. The surface should be cleaner for nanoindentation, and surface roughness should be low to obtain reliable results. Surface roughness also complicates the measurement of crack dimensions with the microscope to calculate fracture toughness. Therefore, crack measurements with SEM have been tried repeatedly to calculate fracture toughness of nonroutine coating tried.

Coating thicknesses were between 1 and 2.5 μm. Coating thicknesses varied due to various difficulties in the production of coatings containing W and Mo. These low thicknesses affected the mechanical evaluation.



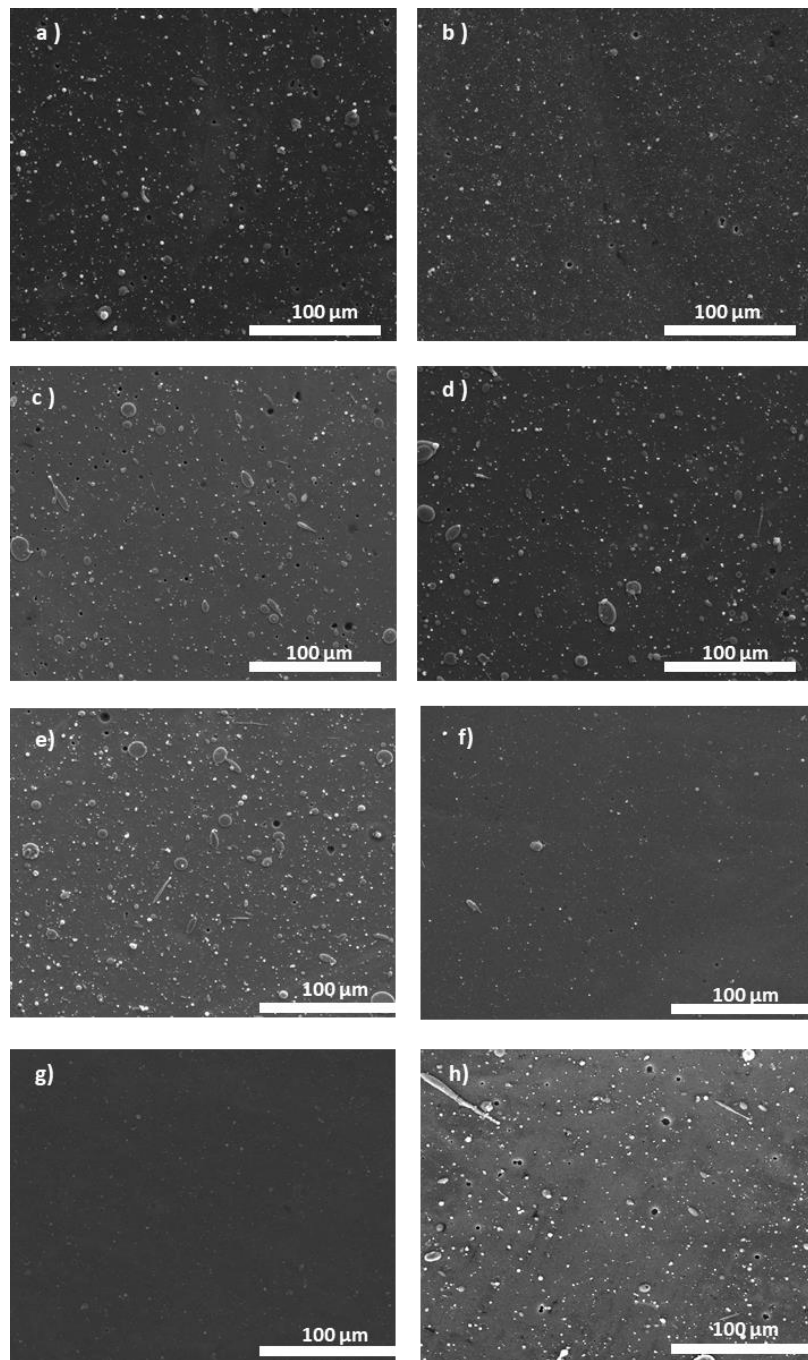


Figure 45. SEM images of nonroutine hard coatings. a)  $\text{Al}_{50}\text{Ti}_{50}$ , b)  $\text{Al}_{50}\text{Ti}_{50}\text{-W-1}$ , c)  $\text{Al}_{50}\text{Ti}_{50}\text{-W-2}$ , d)  $\text{Al}_{67}\text{Ti}_{33}$ , e)  $\text{Al}_{67}\text{Ti}_{33}\text{-Mo-1}$ , f)  $\text{Al}_{67}\text{Ti}_{33}\text{-Mo-2}$ , g)  $\text{Al}_{64}\text{Cr}_{36}$ , h)  $\text{Al}_{64}\text{Cr}_{36}\text{-Mo-1}$ .

Table 15 shows the EDS results of routine commercial hard coatings. Nitrogen amounts are 50%, and we can say there was no problem with nitriding. These fully nitrided hard coatings showed higher hardness values which will be mentioned in mechanical characterization results.

Table 15. EDS results of routine hard coatings.

Sample Name	Atomic %		
	Al	Ti/Cr	N
Al50Ti50	24.1	24.6	51.3
maxAl50Ti50	24.5	26.3	49.3
Al67Ti33	34.6	15.1	50.3
maxAl67Ti33	34.8	17.2	47.9
Al50Cr50	24.5	26.3	49.3
Al64Cr36	36.1	15.6	48.3

Table 16 shows the EDS results of the nonroutine hard coatings. Raw EDS data indicated nitrogen ratios around 50%. This result shows that the obtained coatings are nitrided close to 100%. According to the EDS results, W and Mo amounts could not be obtained as desired due to technical problems at the coating systems. W and Mo have high evaporation temperatures, and there was a need high current to evaporate these elements. The cathode surface area was lower than the commercial coating systems. The current/surface area ratio was higher for nonroutine coating systems. This high ratio caused technical problems in the coating systems, and the power supply system automatically stopped the coating process.

Table 16. EDS result of nonroutine hard coatings.

Sample Name	composition	Atomic %			
		Al	Ti / Cr	W/Mo	N
Al50Ti50	Al <sub>25</sub> Ti <sub>25</sub> N	25	25	-	50
Al50Ti50-W-1	Al <sub>20</sub> Ti <sub>20</sub> W <sub>10</sub> N	20	20	10	50
Al50Ti50-W-2	Al <sub>17</sub> Ti <sub>19</sub> W <sub>14</sub> N	17	19	14	50
Al67Ti33	Al <sub>32</sub> Ti <sub>18</sub> N	32	18	-	50
Al67Ti33-Mo-1	Al <sub>24</sub> Ti <sub>20</sub> Mo <sub>4</sub> N	24	20	4	50
Al67Ti33-Mo-2	Al <sub>24</sub> Ti <sub>18</sub> Mo <sub>8</sub> N	24	18	8	50
Al64Cr36	Al <sub>30</sub> Cr <sub>20</sub> N	30	20	-	50
Al64Cr36-Mo-1	Al <sub>31</sub> Cr <sub>19</sub> N	31	19	-	50
Al64Cr36-Mo-2	Al <sub>25</sub> Ti <sub>21</sub> Mo <sub>4</sub> N	25	21	4	50

EDS gives an idea about the elements and ratio of these elements in the structure, but it does not provide any information about the chemical state of these atoms in the structure. XPS measurements were made to obtain more detailed information on the chemical state of the atoms for selected samples produced both by magnetron sputtering and cathodic arc evaporation techniques. Figure 46 shows XPS spectrums of selected samples. Figure 46(a) belonged to Al50Ti50 routine hard coating, which was produced by the typical procedure of cathodic arc evaporation in Ionbond Turkey Company, and Figure 46(b) belonged to 5050-ref. sample, which was produced by magnetron sputtering. The composition of these samples was (Al<sub>50</sub>Ti<sub>50</sub>)N. XPS results again indicated that the nitrogen ratio was lower than the

aimed one for magnetron sputtering samples. In additional information, XPS results showed oxidization in the structure, unlike EDS and WDS.

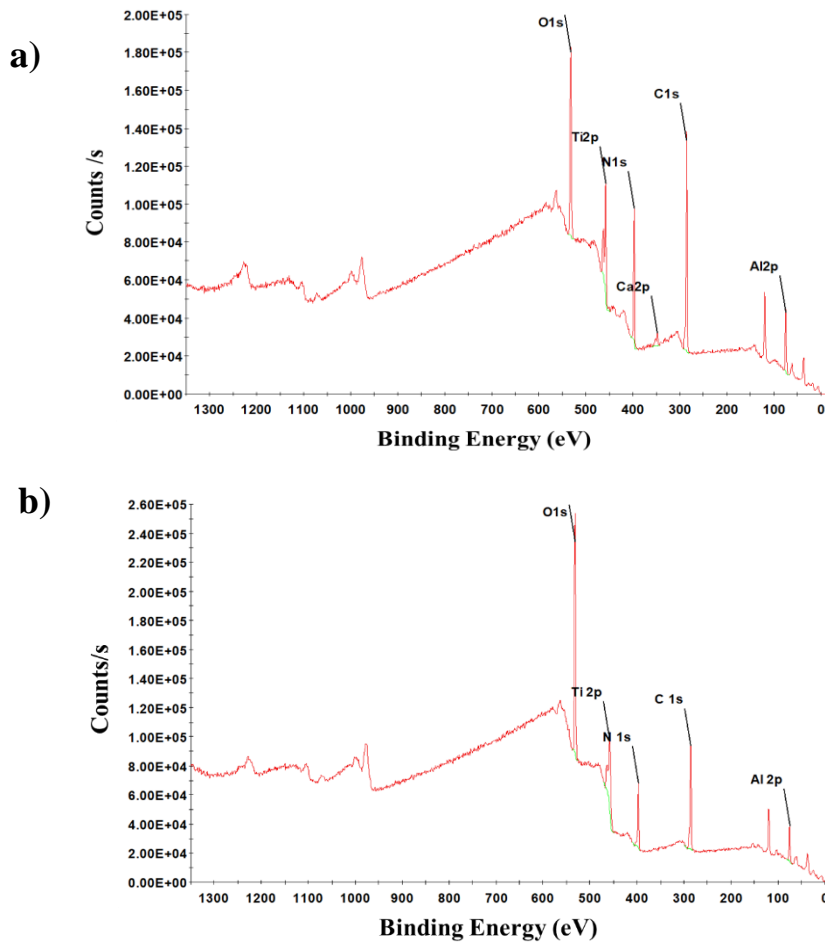


Figure 46. XPS results of a)  $\text{Al}_{50}\text{Ti}_{50}$  routine (cathodic arc evaporation) and b) 5050-ref. (magnetron sputtering) samples. Both of them have  $(\text{Al}_{50}\text{Ti}_{50})\text{N}$  composition.

Table 17 shows the XPS results of samples that were mentioned in the previous paragraph. XPS analysis also gives information about the bonds formed by the

elements. To understand the problem in more detail, atomic ratios have been calculated for Al 2p, Ti 2p, N 1s, and C 1s bonds. The table summarizes the related results. Magnetron sputtering and cathodic arc evaporation hard coatings were similar in terms of binding energies. However, considering the atomic ratios of the said bonds, CAE samples present a nitrogen ratio of up to 44%, while this ratio is only 20% in MS samples. As a result, the nitriding problem has been confirmed by these studies for MS samples. In addition, it has been determined that this nitriding problem is related to the undesired oxidation level. This different composition of all elements affected the mechanical results of the samples. The relationship between mechanical evaluation and structural characterization will be mentioned in Mechanical Characterization Results 3.2.2.

Table 17. XPS results of selected MS and CAE hard coatings. (MS: 5050-ref., CAE: Al<sub>50</sub>Ti<sub>50</sub> samples).

Atom / Orbital	Binding Energy(eV)		Atomic %	
	MS	CAE	MS	CAE
Al 2p	74.51	74.67	24.7	30.9
Ti 2p	456.45	456.78	16.5	15.4
<b>N 1s</b>	397.33	397.45	<b>21.9</b>	<b>43.7</b>
C 1s	279.67	285.01	7.0	4.3
O 1s	532.11	531.56	29.9	5.5

### 3.2.2 Mechanical Characterization

After microstructure analysis, mechanical properties were analyzed by the nanoindentation method. Nanoindentation data were measured with the Agilent G200 NanoIndenter device located in Koç University Surface Technologies Research Center (KUYTAM). All experimental details were explained in experimental parts.

Table 18 shows the nanoindentation results of routine hard coatings. Generally, the thicker coatings showed higher hardness, except AlCr based coatings. The highest H/E ratio gives an idea about the wear performance of the coatings belonged to thicker (Al<sub>67</sub>Ti<sub>33</sub>)N, called maxAl67Ti33 samples. It can also be related to its smallest grain size. (Al<sub>64</sub>Cr<sub>36</sub>)N showed lower hardness but higher H/E value than (Al<sub>50</sub>Cr<sub>50</sub>)N due to lower elastic modulus, although smaller grain size. This situation should be investigated in detail. Elastic modulus showed strange behavior than the hardness. The most significant difference was observed between both AlCr based samples. When H<sup>3</sup>/E<sup>2</sup> ratios were examined, it was seen that the highest values belonged to thicker AlTi based coatings. This ratio gives an idea about the resistance to plastic deformation. Higher hardness values supported this situation.

Table 18. Summary of mechanical evaluation of routine hard coatings.

Sample Name	Thickness (μm)	Grain size (nm)	H (GPa)	E (GPa)	H/E	H <sup>3</sup> /E <sup>2</sup>
Al50Ti50	3	8.7	20	460	0.0435	0.0378
maxAl50Ti50	3.5	7.2	33	506	0.0652	0.1404
Al67Ti33	3	6.4	25	420	0.0595	0.0886
maxAl67Ti33	3.5	5.9	27	380	0.0711	0.1363
Al50Cr50	3	15.3	22.2	450	0.0493	0.0540
Al64Cr36	2.5	6.5	16	280	0.0571	0.0522

Nanoindentation results for all nonroutine were shown in Table 19. Generally, hardness values were 15-25 GPa as expected from fully nitrided hard coatings. Hardness values were increased due to the addition of W/Mo for AlTi-based

coatings. However, for AlCr-based coatings, reversed results were observed. Elastic modulus of AlTi-based hard coatings was increased almost 50%, while Elastic modulus of AlCr-based hard coatings was decreased. The H/E ratio gives an idea about the wear performance of nitride coatings (Leyland & Matthews, 2004). According to the H/E, the best wear resistance belonged to sample Al<sub>67</sub>Ti<sub>33</sub>, and it was reduced due to the addition of W and Mo. The addition of Mo increased this ratio for AlCr-based coatings. H<sup>3</sup>/E<sup>2</sup> values also supported these results. Hardness values were higher than the previous samples produced by magnetron sputtering and agree with the literature.

Table 19. Nanoindentation results for all nonroutine Ionbond Samples.

Sample Name	At.% W /Mo	Grain size	Thickness ( $\mu\text{m}$ )	H(GPa)	E.M. (GPa)	H/E	H <sup>3</sup> /E <sup>2</sup>
Al50Ti50	-	8.3	2.5	20	460	0.0435	0.0378
Al50Ti50-W-1	10	10.8	1	22	410	0.0537	0.0633
Al50Ti50-W-2	14	10.4	1	20.1	370	0.0543	0.0593
Al67Ti33	-	10.1	2.5	20.4	246.5	0.0828	0.140
Al67Ti33-Mo-1	4	7.8	1.3	25.2	480	0.0525	0.0694
Al67Ti33-Mo-2	8	5.9	1.5	27	410	0.0659	0.1171
Al64Cr36	-	15.9	1.5	24.2	488	0.0496	0.0595
Al64Cr36-Mo-1	-	4.9	1.3	21	385	0.0545	0.0625
Al64Cr36-Mo-2	4	8.5	1	22.2	338.3	0.0656	0.0956

Nanoindentation was also used to obtain the fracture toughness of the coatings. Fracture toughness values and used properties for routine hard coatings were listed in Table 20. Firstly, the Al<sub>64</sub>Cr<sub>36</sub> named sample did not show any crack after nanoindentation of Berkovich and Cube corner tips. The highest fracture toughness value belonged to the maxAl<sub>67</sub>Ti<sub>33</sub> sample. The thicker coatings showed higher hardness and smaller crack sizes. Figure 47 shows SEM images for the calculation of fracture toughness of these routine hard coatings. AlCr based surfaces were not smooth as other surfaces, and cracks were not stable.

Table 20. Calculated fracture toughness for routine hard coatings.

<b>Sample Name</b>	<b>H (GPa)</b>	<b>E (GPa)</b>	<b>E/H</b>	<b>C (μm)</b>	<b>K<sub>IC</sub> (MPa√m)</b>
Al50Ti50	20	460	23	3.22	6.6
maxAl50Ti50	33	506	15.3	2.85	6.5
Al67Ti33	25	420	16.8	4.15	3.9
maxAl67Ti33	27	380	14.1	1.18	23.4
Al50Cr50	22.2	450	20.3	2.89	9.4
Al64Cr36	16	280	17.5	No crack	-



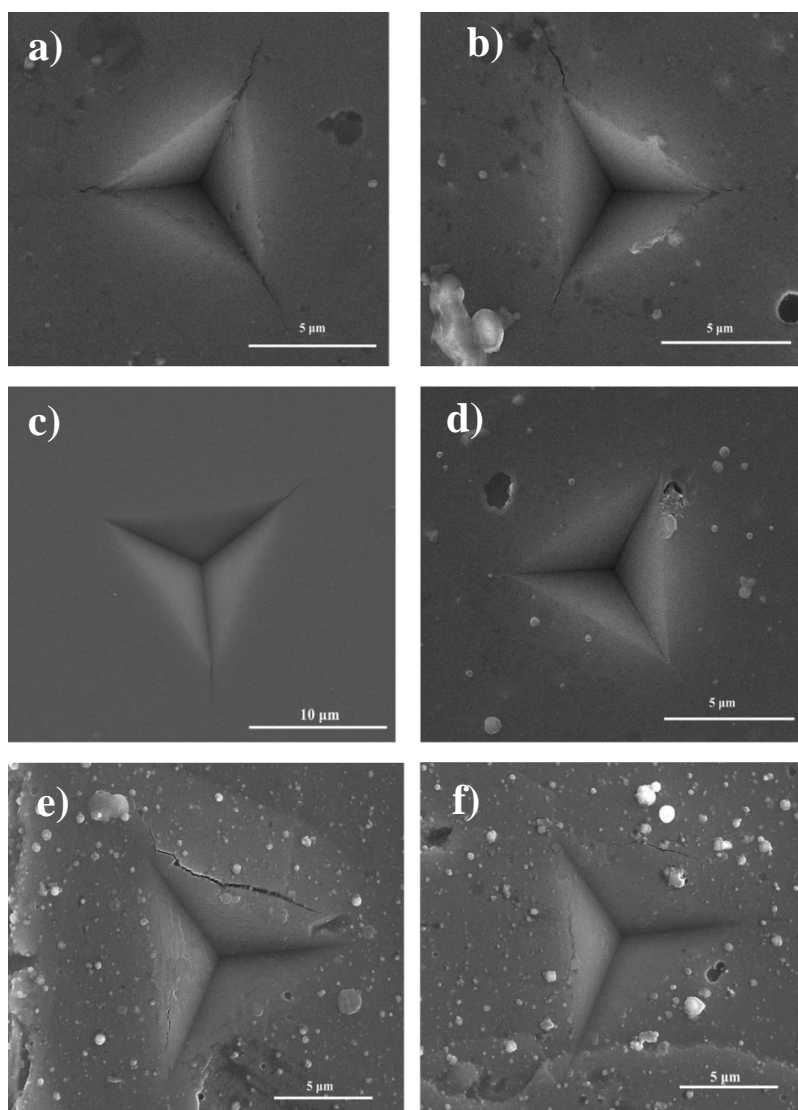


Figure 47. SEM images of routine hard coatings after nanoindentation. a)  $\text{Al}_{50}\text{Ti}_{50}$ , b)  $\text{maxAl}_{50}\text{Ti}_{50}$ , c)  $\text{Al}_{67}\text{Ti}_{33}$ , d)  $\text{maxAl}_{67}\text{Ti}_{33}$ , d)  $\text{Al}_{50}\text{Cr}_{50}$ , e)  $\text{Al}_{64}\text{Cr}_{36}$ .

Fracture toughness was also calculated for nonroutine hard coatings after nanoindentation. Nanoindentation results in Table 19 were obtained using the Berkovich tip. However, cracks were not observed under SEM to calculate the fracture toughness of these coatings. Cube corner tip was used to get cracks at the corner of the coatings after nanoindentation. Figure 48 shows SEM images of nonroutine hard coatings after cube-corner nanoindentation. There were tiny cracks

at the corner of the indents. It can be seen that the surface quality is too bad for AlCr based, and also, there was no crack after the test. However, AlTi based coatings showed some small cracks. Reference samples, Al<sub>50</sub>Ti<sub>50</sub>, and Al<sub>67</sub>Ti<sub>33</sub> had higher cracks than W or Mo added ones.

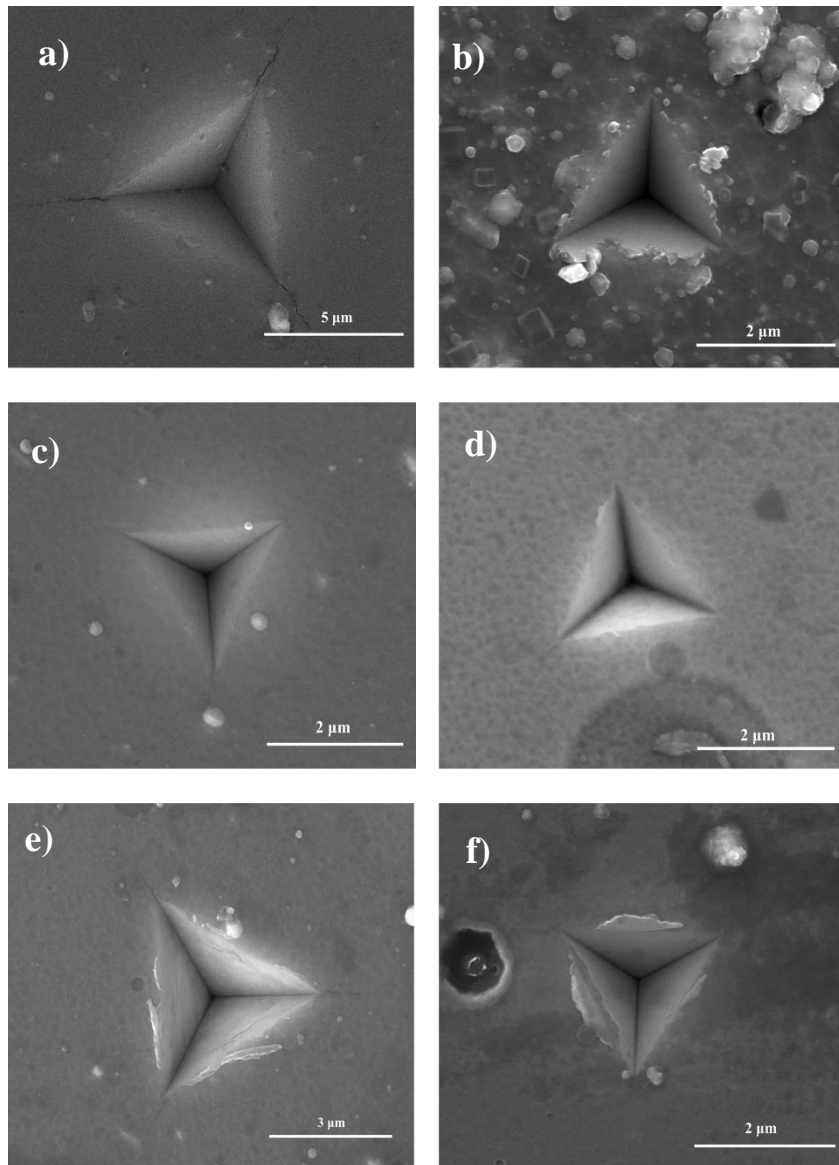


Figure 48. SEM images after cube corner nanoindentation a) Al<sub>67</sub>Ti<sub>33</sub>, b) Al<sub>64</sub>Cr<sub>36</sub>, c) Al<sub>50</sub>Ti<sub>50</sub>-W-1, d) Al<sub>50</sub>Ti<sub>50</sub>-W-2, e) Al<sub>67</sub>Ti<sub>33</sub>-Mo-1, f) Al<sub>67</sub>Ti<sub>33</sub>-Mo-2.

Table 21 shows the calculated fracture toughness of nonroutine hard coatings. AlCr based samples could not be tested systematically. Al<sub>64</sub>Cr<sub>36</sub> named sample had no crack after Berkovich and Cube corner nanoindentation. Al<sub>64</sub>Cr<sub>36</sub>-Mo-1 did not test with cube-corner due to not including Mo, and Al<sub>64</sub>Cr<sub>36</sub>-Mo-2 named sample had rough surface and cracks did not find under SEM. Al<sub>50</sub>Ti<sub>50</sub> named sample has very low fracture toughness and 10 at.% W adding increased fracture toughness almost 20 times and 14 at.% W adding increased it 30 times. These results were remarkable. The same behavior can be seen for Al<sub>67</sub>Ti<sub>33</sub> and Mo-added ones. Figure 49 shows the effect of W and Mo addition on fracture toughness of the nonroutine hard coatings.

Table 21. Calculated fracture toughness of nonroutine hard coatings.

Sample name	E (GPa)	H (GPa)	E/H	C <sub>ave</sub> (μm)	K <sub>IC</sub> (MPa√m)
Al <sub>50</sub> Ti <sub>50</sub>	490	34.4	14.24	4.11	0.94
Al <sub>50</sub> Ti <sub>50</sub> -W-1	423.9	36.4	11.65	0.38	22.14
Al <sub>50</sub> Ti <sub>50</sub> -W-2	447.7	33	13.57	0.35	31.21
Al <sub>67</sub> Ti <sub>33</sub>	426.4	37.3	11.43	3.12	1.28
Al <sub>67</sub> Ti <sub>33</sub> -Mo-1	375.3	35.3	10.63	1.37	3.25
Al <sub>67</sub> Ti <sub>33</sub> -Mo-2	445.7	45.7	9.75	0.31	37.63
Al <sub>64</sub> Cr <sub>36</sub>	536.8	37.6	14.28	No crack	-
Al <sub>64</sub> Cr <sub>36</sub> -Mo-1	No results with cube-corner				
Al <sub>64</sub> Cr <sub>36</sub> -Mo-2	445.6	27.6	16.14	No data	*

\*No crack under SEM due to high surface roughness

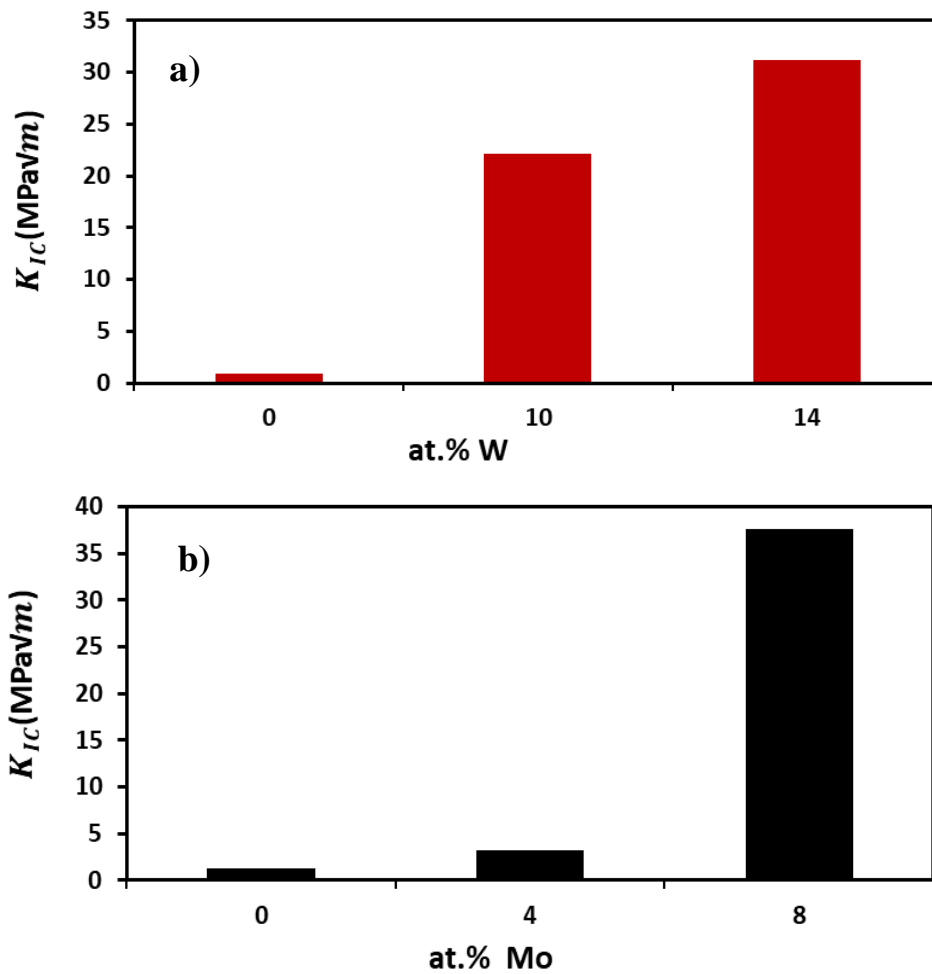


Figure 49. a)  $K_{IC}$  vs. at.% W and b)  $K_{IC}$  vs. at.% Mo.

Another critical part of this thesis was micro-cantilever bending. Calculation and comparison of fracture toughness results were desired for all samples. However, a comparison could be made for only one type of coatings due to the following reasons. Manufacturing steps of micro-cantilevers were used to prepare new cantilevers. W-added coatings were etched with Si(100) wafer at the same time during the etching procedure. Different etching parameters such as temperature and duration were tried, but the problem could not be solved. There is a need to develop a new etching procedure for W added ones.

The routine hard coating, which was  $\text{Al}_{50}\text{Ti}_{50}$ , was prepared for the micro-cantilever bending test. Berkovich tip and 1000 nm/min loading rate are used to test. Figure 50 shows the load-displacement curve of cantilever No.1. First, there was a linear increase in load and displacement, and a sudden drop was observed. In the fracture mechanics experiment, only the part up to the beginning of this sudden drop was important. The decreasing load and increasing displacement in the continuation of the data are due to the nanoindentation device's inability to immediately respond to sudden braking and the diamond tip to advance further.

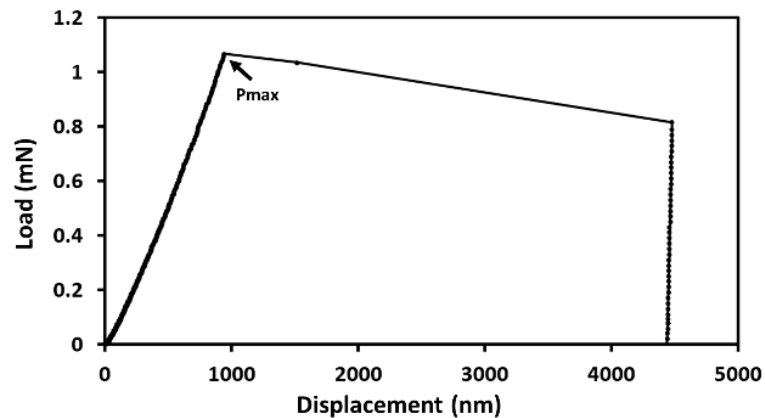


Figure 50. The load-displacement curve of cantilever no.1.

The relevant dimensions of the microbeams were determined by SEM and the elastic modulus within the scope of nanoindentation measurements, as explained in the previous sections. For example, for micro-cantilever number 1, the length was 21.5  $\mu\text{m}$  (the distance from the loading point to the notch), the thickness was 3.1  $\mu\text{m}$ , the width was 4.4  $\mu\text{m}$ , and the elastic modulus was 491 GPa. Figure 51 shows the results obtained by applying these values to Equation (4) with a dashed line and the measurement results in red. Although the load prediction of the linear elastic displacement equation is higher than the test results, it is at a similar level in order.

The main reason for the lower level of the experimental result is the additional flexibility created by the notch in the sample. Another reason for the difference between experiment and theory is that there is a deformation beyond the small strain condition, which is one of the assumptions of Equation (6). Since the main purpose of this simple analysis is to confirm that reasonable values have been measured, a more detailed analysis has not been done at this stage.

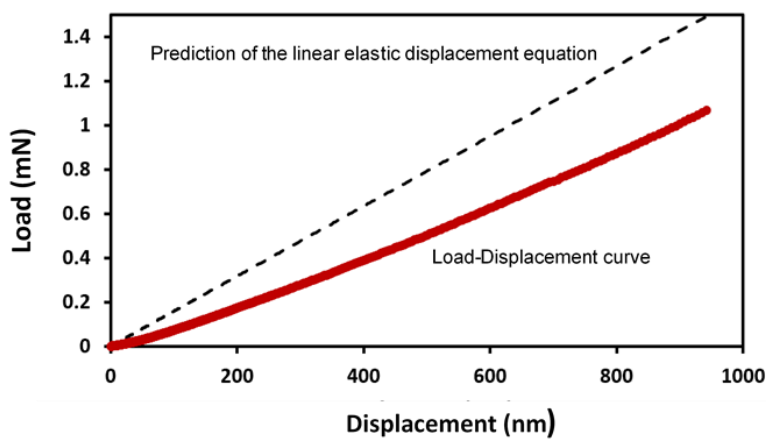


Figure 51. Load-Displacement measurement and prediction of linear elastic displacement equation for Cantilever No.1

Table 22 shows the fracture toughness calculation results.  $K_{IC\ average}$  was  $4.85\ \text{MPa}\sqrt{\text{m}}$ . However, the repeatability of results should be improved due to changing between 4 to  $6.5\ \text{MPa}\sqrt{\text{m}}$ . Table 23 compares the fracture toughness of AlTi based coatings for both micro-cantilever bending and nanoindentation based. These two coatings were produced using the cathodic arc evaporation technique. The first one was routine Al50Ti50, and the second one was nonroutine Al50Ti50. It can be said that the results were not so close but also not so far from each other.

Table 22. Micro-cantilever bending results.

#of cantilever	$P_{max}$ (mN)	b ( $\mu\text{m}$ )	a ( $\mu\text{m}$ )	w ( $\mu\text{m}$ )	L ( $\mu\text{m}$ )	$K_{Ic}$ ( $\text{MPa}\sqrt{\text{m}}$ )
1	1.07	4.44	1	3.08	21.3	6.68
2	0.55	4.45			20	3.19
3	0.85	4.45			22.5	5.58
4	0.63	4.44			21.5	3.93

Table 23. Comparison of calculated fracture toughness using two different methods.

Coating	Fracture toughness calculation method	$K_{Ic}$ ( $\text{MPa}\sqrt{\text{m}}$ )
Al50Ti50 routine	Cantilever bending	4.8
Al50Ti50 routine	Nanoindentation	6.6

Notch depth is the most critical parameter for fracture toughness measurement. The fracture region was analyzed more sensitively with SEM for getting a better result. It is important to examine the fracture region with SEM and verify the notch depth from the contrast difference between the notch and the fractured region to obtain more reliable results. From the measurements on the SEM images presented in Figure 52, it is concluded that the predicted depth and the actual depth were compatible with the notch opening with the focused ion beam.

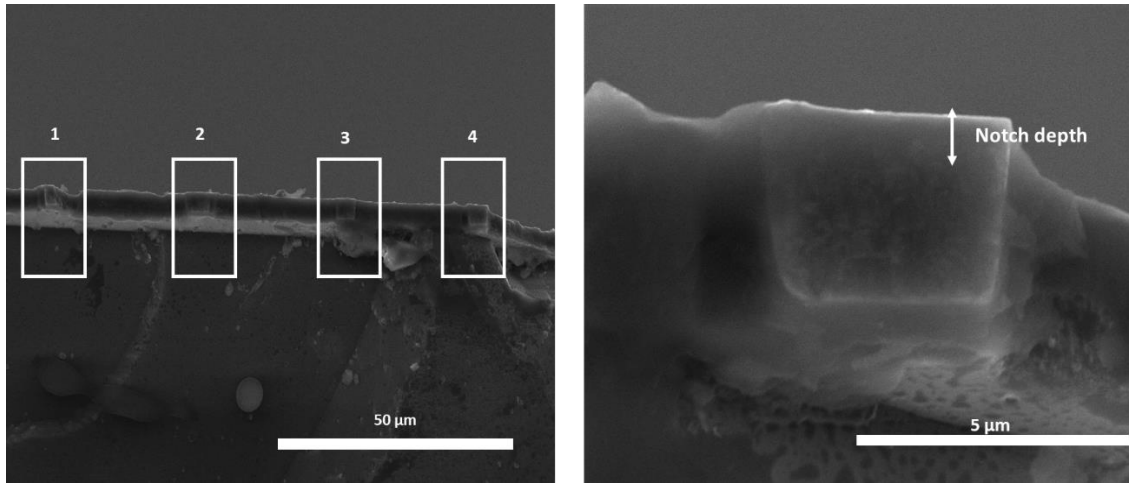


Figure 52. SEM images of example fracture surfaces after cantilever bending test.

After evaluating fracture toughness of the hard coatings, wear CSM Tribometer Device did resistance tests in Prof. Dr. Kürşat Kazmalı's Laboratory in İTÜ. Table 24 shows wear test details. Pin-on-disk and ball-on disk tests were wanted to do, but only ball-on disc tests were done. High-speed steel was as substrate material, and all discs were polished before coating. Coating parameters were the same as parameters that were explained before.

Figure 53 shows the friction coefficient and friction distance of coatings against the 440C SS ball. Fluctuation of friction coefficient can be seen due to droplets on the surface. Additionally, it can be seen due to the removal of coatings and friction between steel-steel. Results showed that as the surface roughness increases the friction coefficient.



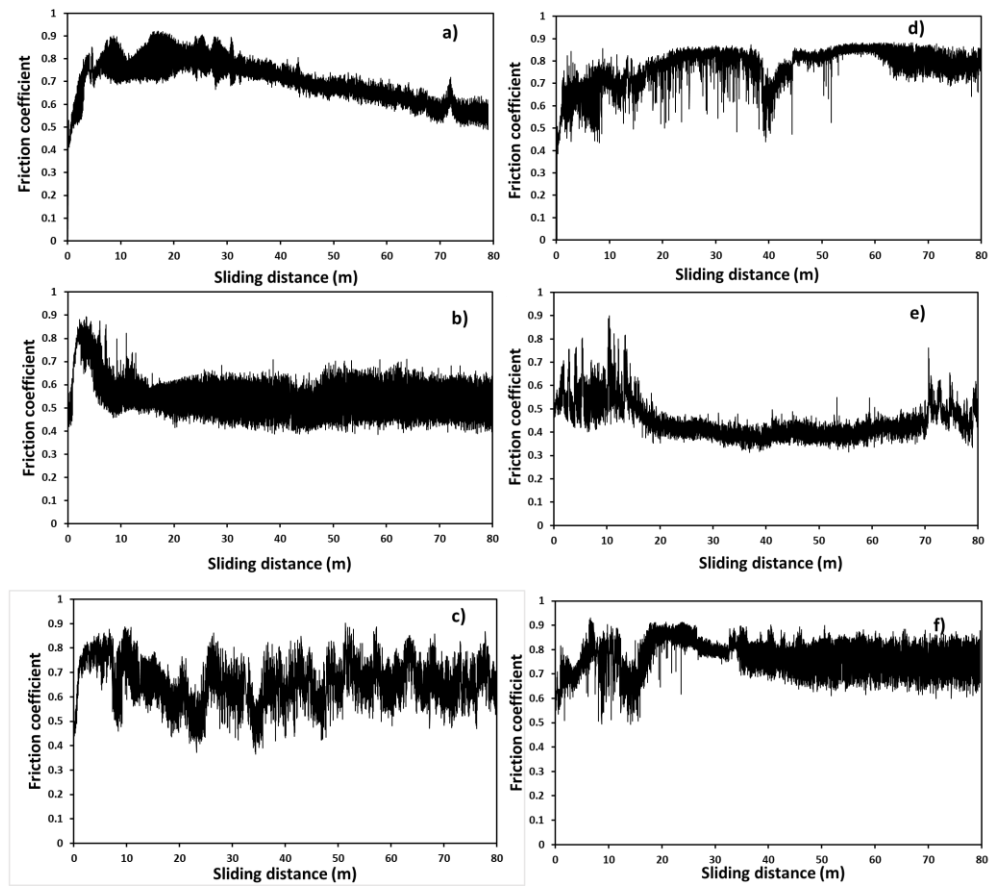


Figure 53. The friction coefficient of a)  $\text{Al}_{67}\text{Ti}_{33}$ , b)  $\text{Al}_{64}\text{Cr}_{36}$ , c)  $\text{Al}_{50}\text{Ti}_{50}\text{W}-1$ , d)  $\text{Al}_{50}\text{Ti}_{50}\text{W}-2$ , e)  $\text{Al}_{67}\text{Ti}_{33}\text{Mo}-1$ , f)  $\text{Al}_{64}\text{Cr}_{36}\text{Mo}-1$  against 440C SS ball.

Figure 54 shows the friction coefficient and friction distance of coatings against the Alumina ball. Fluctuation of friction coefficient can be seen for this part, too. However, it was less than the experiments against stainless steel balls. The friction coefficient was lower than the tests against the steel ball. Since there was no significant wear in the alumina balls, wear rates were not measured.

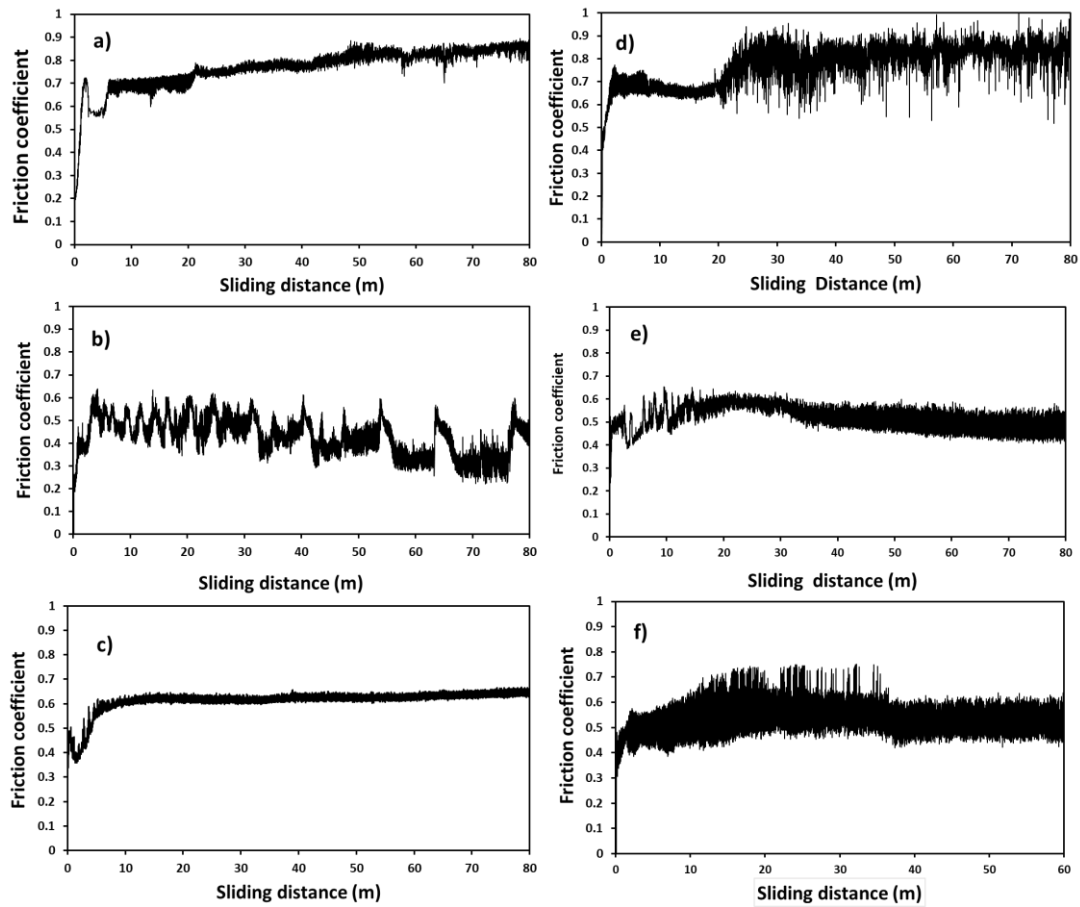


Figure 54. The Friction coefficient of a)  $Al_{67}Ti_{33}$ , b)  $Al_{64}Cr_{36}$ , c)  $Al_{50}Ti_{50}W-1$ , d)  $Al_{50}Ti_{50}W-2$ , e)  $Al_{67}Ti_{33}Mo-1$ , f)  $Al_{64}Cr_{36}Mo-2$  against Alumina ball.

The friction coefficients of the coatings tested against the inert surface, i.e., Alumina ball, and against the non-inert surface, i.e., 440C stainless steel ball were summarized in Table 24.

Table 24. The friction coefficient of nonroutine coatings.

Sample Name	Friction Coefficient	
	Against 440C SS ball	Against Alumina ball
Al67Ti33	0.69	0.77
Al64Cr36	0.54	0.42
Al50Ti50-W-1	0.77	0.77
Al50Ti50-W-2	0.65	0.61
Al67Ti33-Mo-1	0.76	0.52
Al64Cr36-Mo-2	0.45	0.52

Considering the wear rates of the 440C steel balls against the coated samples in the wear tests (Figure 55), it was seen that the lowest wear rate was obtained in the case of friction against Al<sub>50</sub>Ti<sub>50</sub>W-2 and Al<sub>67</sub>Ti<sub>33</sub>Mo-1 samples. The ball wear rates against the Al<sub>50</sub>Ti<sub>50</sub>W-2 sample were low due to the high wear of this coating. This coating has 2 layers (AlTiN+AlTiWN); there should be low adhesion between these two layers. It can explain why the wear of this coating was low. The wear rate of 440C SS balls against the Al<sub>67</sub>Ti<sub>33</sub>Mo-1 coating was also low. Mo element formed an oxide phase, which behaved as lubricant material between coated surface and ball. MoO<sub>3</sub> behaves as a lubricant material, and it can reduce wear and friction (Tang et al., 2018).

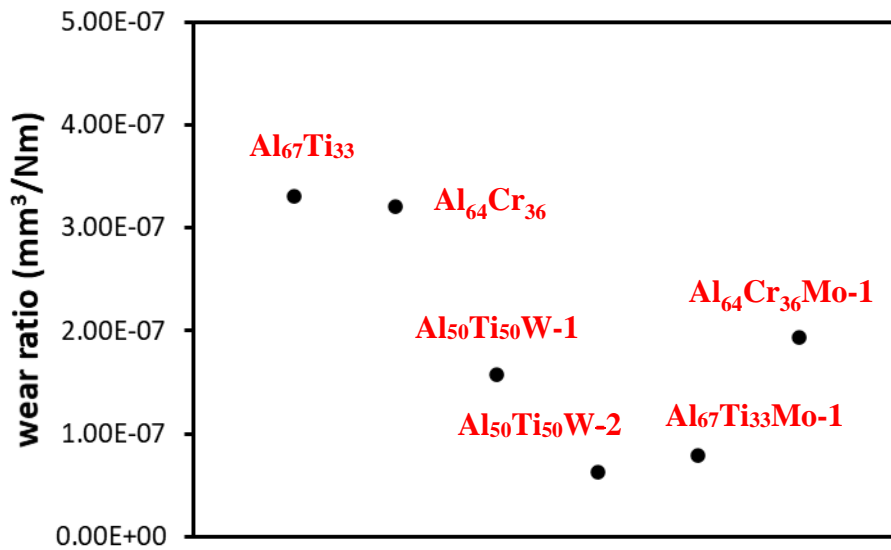


Figure 55. Wear ratio of samples.

After wear tests, SEM and 3D profilometry were used to understand changing of disc surfaces. Figure 56-62 shows some examples of 2D, 3D profilometry, and SEM results. Generally, wear profiles of uncoated discs showed similar behavior as Al<sub>50</sub>Ti<sub>50</sub>W-2 (2 layered). Although the wear marks in the steel ball tests were less than the alumina ball, it was understood that this wear mark is quite high, considering that the hardness of the steel ball is much less than that of alumina. When the wear profiles of the other samples were examined, it was seen that there were elevations within the wear trace. This situation was easily seen, especially in 2D profiles. These elevations were due to wear products adhering to the surface. This adhesive wear behavior in Al<sub>50</sub>Ti<sub>50</sub>W-2, where the adhesion was not good, caused the soft character 440C steel to erode the surface, which was harder than itself. In other samples, there was no wear on the coatings due to good adhesion. Two-dimensional profiles clearly show this situation. Figure 56 shows uncoated discs results after the ball-on disc test. There was massive removal against the Alumina balls and 440C balls; red particles showed considerable removal, especially against the Alumina balls.

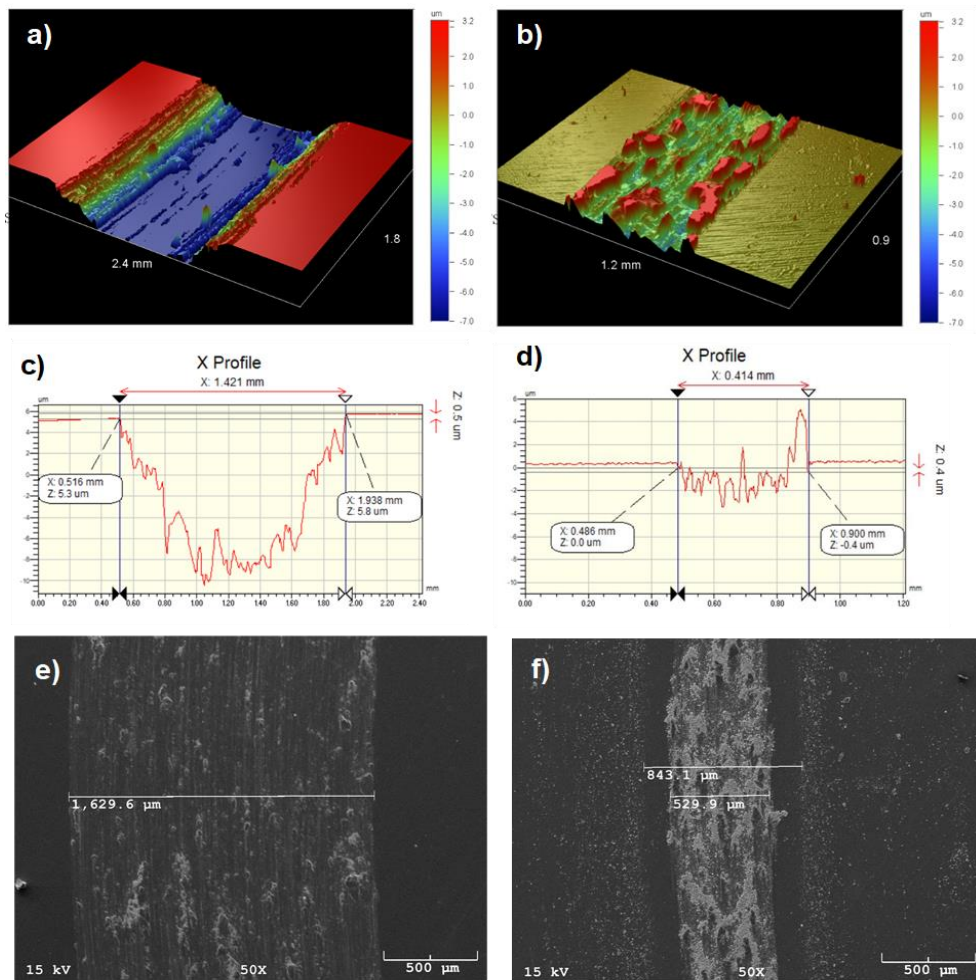


Figure 56. Analysis of uncoated disc after test: a) 3D profile against Al<sub>2</sub>O<sub>3</sub> balls, b) 3D profile against 440C SS balls, c) 2D profile against Al<sub>2</sub>O<sub>3</sub> balls, d) 2D profile against 440C SS balls, e) SEM images of uncoated discs against Al<sub>2</sub>O<sub>3</sub> balls. f) SEM images of uncoated discs against 440C SS balls.

Figure 57 shows Al<sub>67</sub>Ti<sub>33</sub> results after the ball-on disc test. There was no removal against the Alumina balls, but red particles showed a small amount of removal against the 440C SS balls.

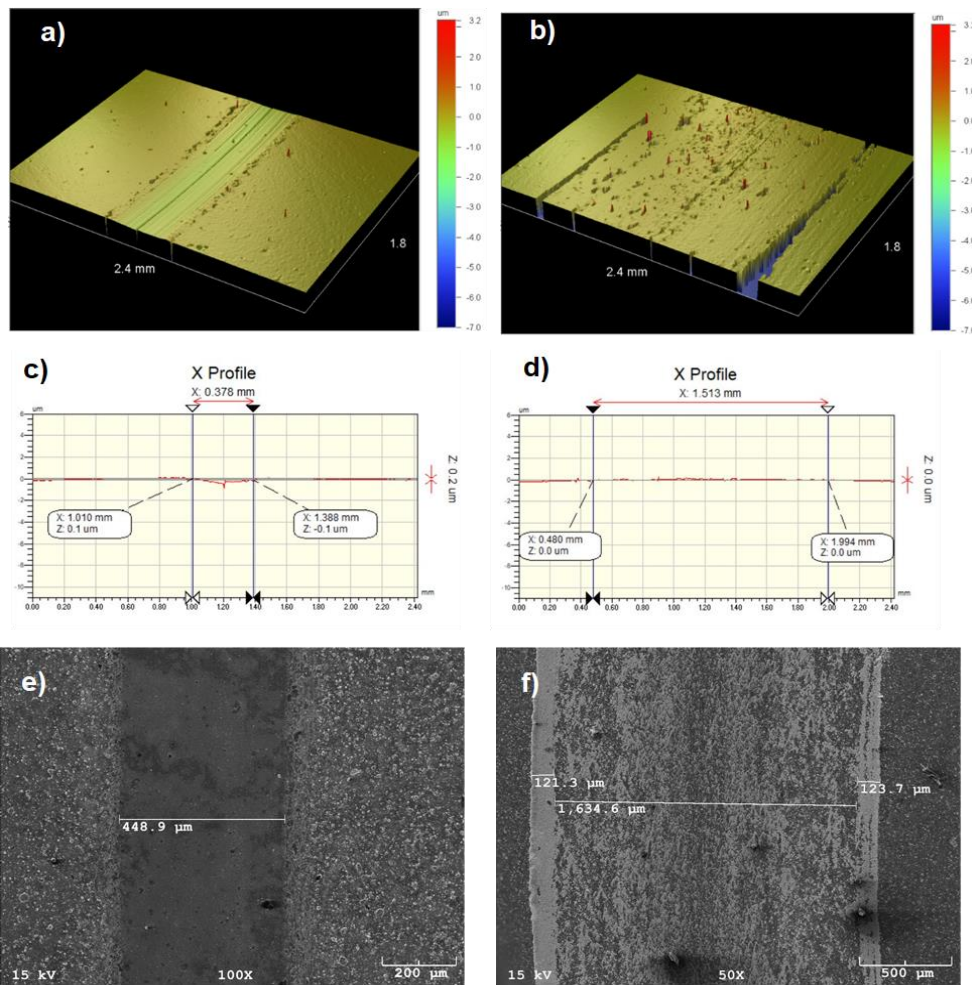


Figure 57. Analysis of  $\text{Al}_{67}\text{Ti}_{33}$  coated disc after test: a) 3D profile against  $\text{Al}_2\text{O}_3$  balls, b) 3D profile against 440C SS balls, c) 2D profile against  $\text{Al}_2\text{O}_3$  balls, d) 2D profile against 440C SS balls, e) SEM images of  $\text{Al}_{67}\text{Ti}_{33}$  coated discs against  $\text{Al}_2\text{O}_3$  balls. f) SEM images of  $\text{Al}_{67}\text{Ti}_{33}$  coated discs against 440C SS balls.

Figure 58 shows the wear test of  $\text{Al}_{64}\text{Cr}_{36}$  coated discs against Alumina and 440C SS balls. There was no removal against the Alumina balls, but red particles showed a large amount of removal against the 440C SS balls.

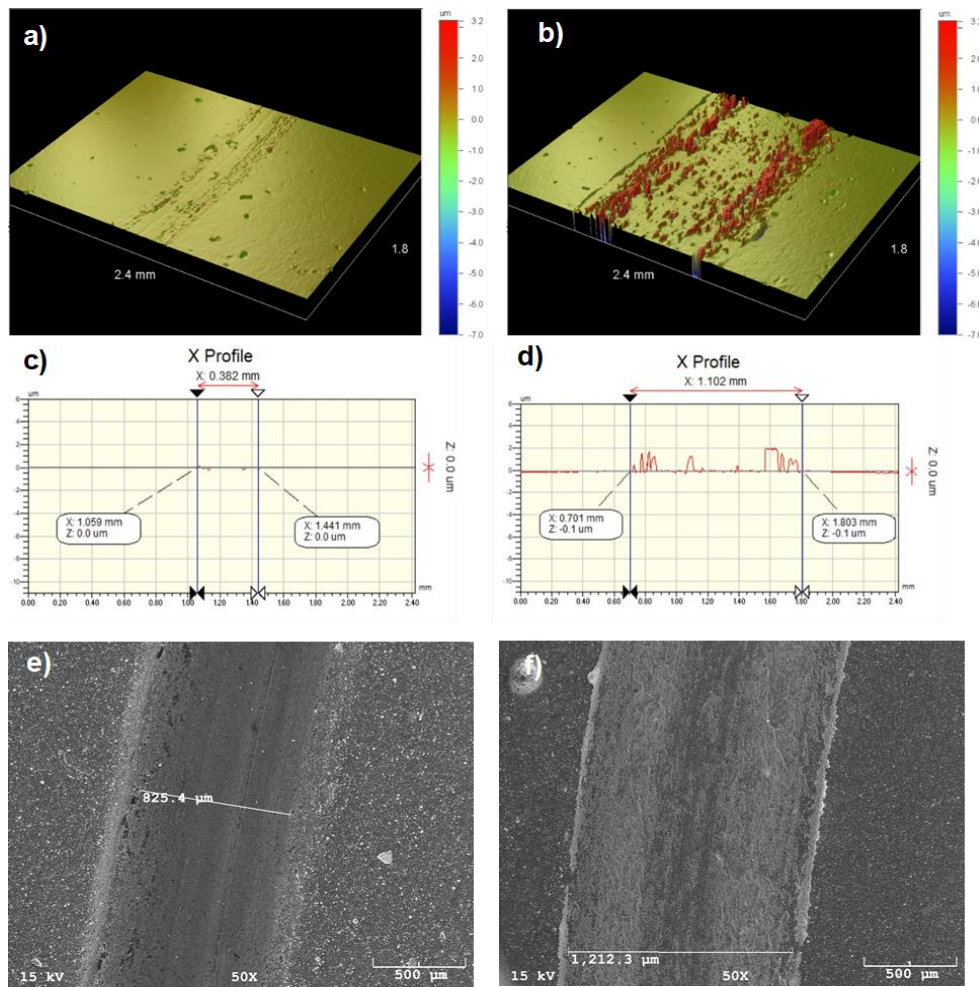


Figure 58. Analysis of  $\text{Al}_{64}\text{Cr}_{36}$  coated disc after test: a) 3D profile against  $\text{Al}_2\text{O}_3$  balls, b) 3D profile against 440C SS balls, c) 2D profile against  $\text{Al}_2\text{O}_3$  balls, d) 2D profile against 440C SS balls, e) SEM images of  $\text{Al}_{64}\text{Cr}_{36}$  coated discs against  $\text{Al}_2\text{O}_3$  balls. f) SEM images of  $\text{Al}_{64}\text{Cr}_{36}$  coated discs against 440C SS balls.

Figure 59 shows the wear test of  $\text{Al}_{50}\text{Ti}_{50}\text{-W-1}$  (at.% 10 W) coated discs against Alumina and 440C SS balls. There was no removal against the Alumina balls, but red particles showed limited removal against the 440C SS balls.

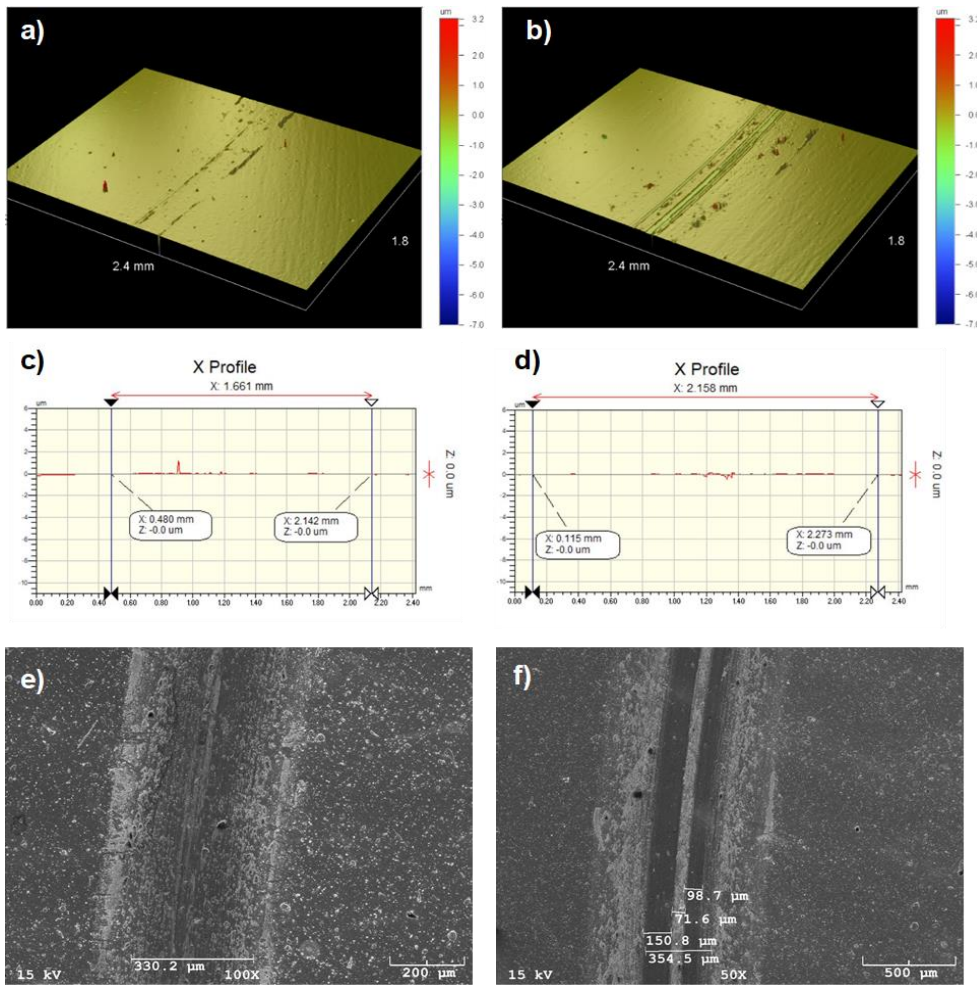


Figure 59. Analysis of Al<sub>50</sub>Ti<sub>50</sub>-W-1 coated disc after test: a) 3D profile against Al<sub>2</sub>O<sub>3</sub> balls, b) 3D profile against 440C SS balls, c) 2D profile against Al<sub>2</sub>O<sub>3</sub> balls, d) 2D profile against 440C SS balls, e) SEM images of Al<sub>50</sub>Ti<sub>50</sub>-W-1 coated discs against Al<sub>2</sub>O<sub>3</sub> balls. f) SEM images of Al<sub>50</sub>Ti<sub>50</sub>-W-1 coated discs against 440C SS balls.

Figure 60 shows the wear test of Al<sub>50</sub>Ti<sub>50</sub>-W-2 coated discs against Alumina and 440C SS balls. There was no removal against the Alumina balls, but red particles showed a large amount of removal against the 440C SS balls. The highest wear belonged to this coating for both Alumina and 440C SS balls. This coating has two layers, and low adhesion between these two layers caused the low wear performance.



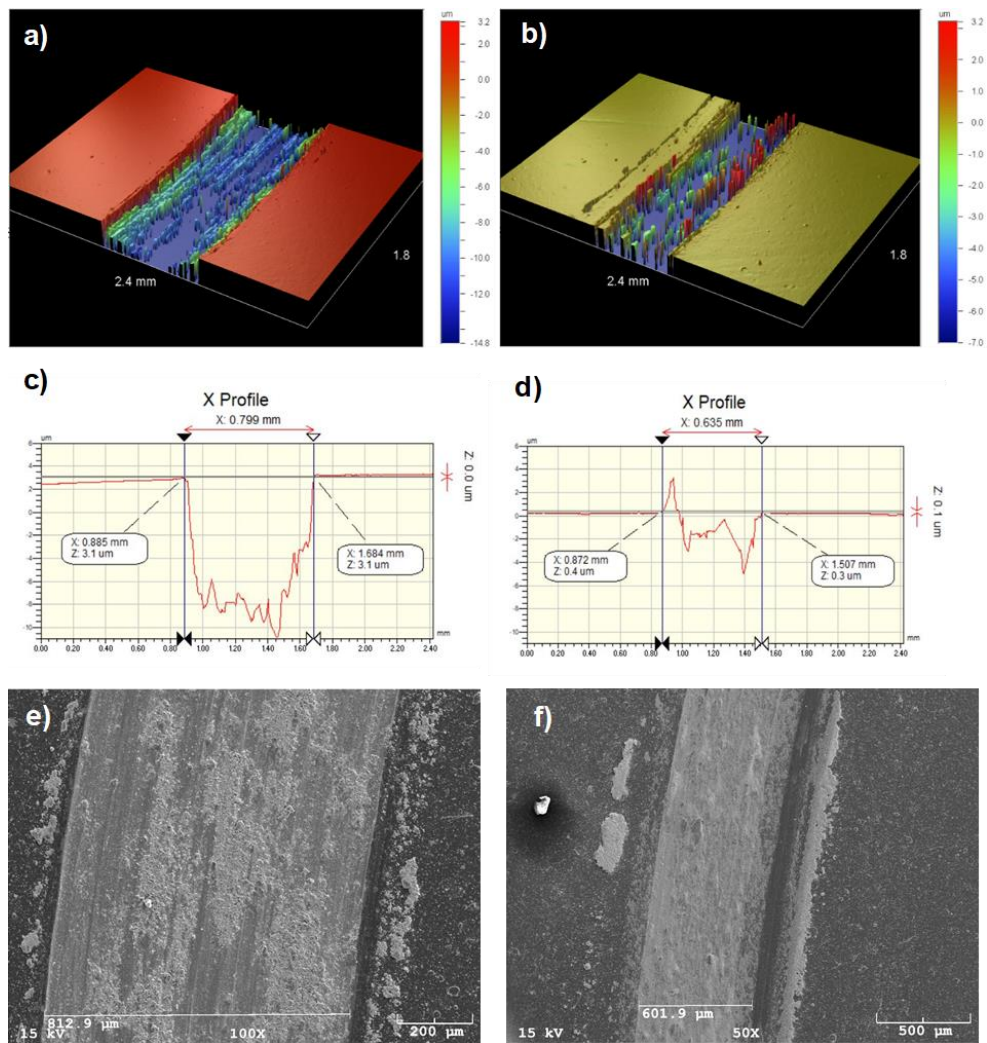


Figure 60. Analysis of  $Al_{50}Ti_{50}-W-2$  coated disc after test: a) 3D profile against  $Al_2O_3$  balls, b) 3D profile against 440C SS balls, c) 2D profile against  $Al_2O_3$  balls, d) 2D profile against 440C SS balls, e) SEM images of  $Al_{50}Ti_{50}-W-2$  coated discs against  $Al_2O_3$  balls. f) SEM images of  $Al_{50}Ti_{50}-W-2$  coated discs against 440C SS balls.

Figure 61 presents the surface profile and images of the  $Al_{67}Ti_{33}-Mo-1$  coating after wear tests. While there was no removal in the coating in the test against alumina balls, as can be seen from the red particles, there is a small amount of lift in the coatings in the test conducted against 440C steel.

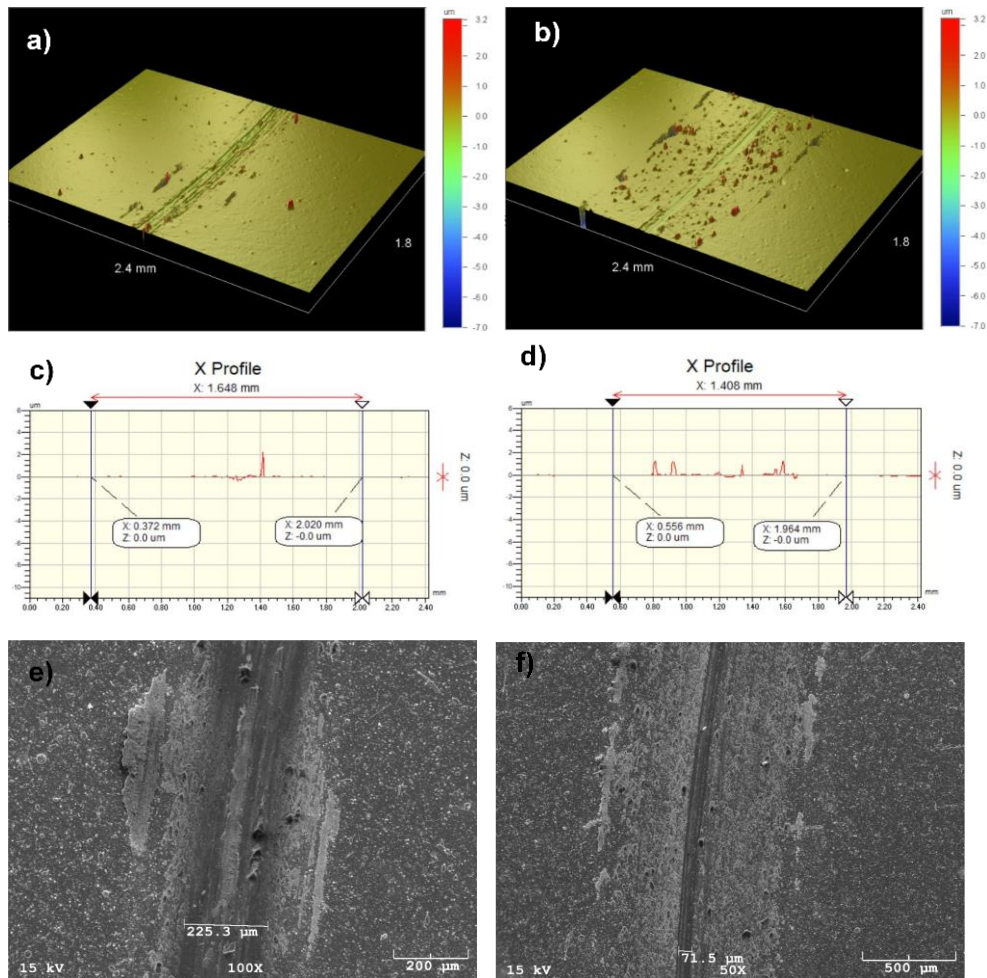


Figure 61. Analysis of  $\text{Al}_{67}\text{Ti}_{33}\text{-Mo-1}$  coated disc after test. a) 3D profile against  $\text{Al}_2\text{O}_3$  balls, b) 3D profile against 440C SS balls, c) 2D profile against  $\text{Al}_2\text{O}_3$  balls, d) 2D profile against 440C SS balls, e) SEM images of  $\text{Al}_{67}\text{Ti}_{33}\text{-Mo-1}$  coated discs against  $\text{Al}_2\text{O}_3$  balls. f) SEM images of  $\text{Al}_{67}\text{Ti}_{33}\text{-Mo-1}$  coated discs against 440C SS balls.

Figure 62 presents the surface profile and images of the  $\text{Al}_{64}\text{Cr}_{36}\text{-Mo-2}$  coating after wear tests. While there is no removal in the test against alumina balls, as can be

understand from the red particles. In addition, after the #4 Al<sub>2</sub>O<sub>3</sub>-W-2 coating, the most wear was seen in this coating.

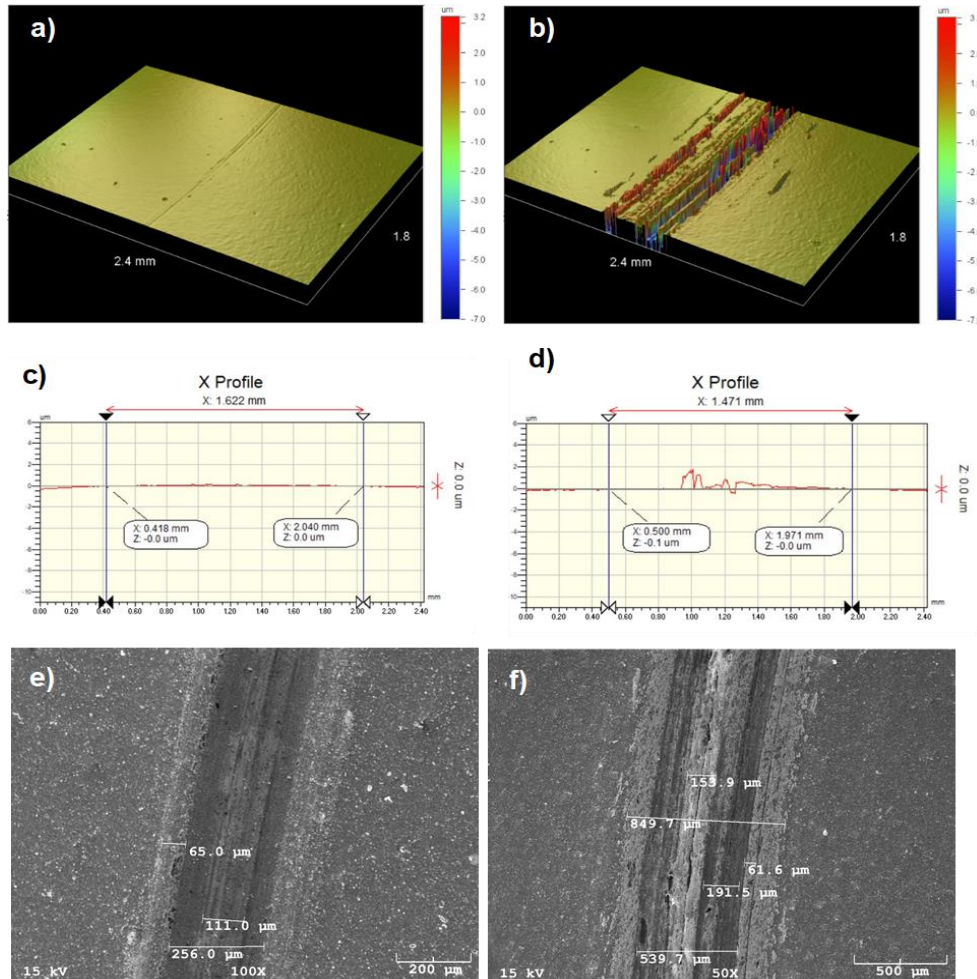


Figure 62. Analysis of Al<sub>64</sub>Cr<sub>36</sub>-Mo-1 coated disc after test: a) 3D profile against Al<sub>2</sub>O<sub>3</sub> balls, b) 3D profile against 440C SS balls, c) 2D profile against Al<sub>2</sub>O<sub>3</sub> balls, d) 2D profile against 440C SS balls, e) SEM images of Al<sub>64</sub>Cr<sub>36</sub>-Mo-1 coated discs against Al<sub>2</sub>O<sub>3</sub> balls. f) SEM images of Al<sub>64</sub>Cr<sub>36</sub>-Mo-1 coated discs against 440C SS balls.

As a result, adhesive wear can be seen clearly against the 440C SS balls. Droplets on the surfaces supported this kind of wear. Tribo-chemical products have soft nature. Generally, wear on Alumina balls was very limited. Especially, sticking of 2 layered W nitride on the surface of balls was observed. The highest wear was observed for this sample, and the lowest wear on SS balls can be seen for this sample, too. The other samples did not show any wear against the alumina balls. Mo included samples that had lower friction due to  $\text{MoO}_3$ , which behaves as a lubricant.

After the wear test, a drilling test was applied to understand the metal cutting performance of the coatings. All drilling tools coated with the cathodic arc evaporation method in Ionbond Turkey company. Coating parameters and other details were mentioned in the experimental parts.

Figure 63 shows high-resolution macro-objective images of eroded tools during the respective performance experiments. Each row has different coatings. Some photos have never been used in each row from left to right, and after processing 25 holes, 50 holes, and 75 holes.

The findings show that the  $\text{Al}_{50}\text{Ti}_{50}\text{-W-2}$  and  $\text{Al}_{64}\text{Cr}_{36}\text{-Mo-1}$  coatings shown in Figure 63 (d) and (f) showed the lowest wear. Therefore, it has been revealed that W and Mo additions are practical on wear resistance, which was one of the most important objectives of the project.  $\text{Al}_{50}\text{Ti}_{50}\text{-W-2}$  coating was two-layered: 1.  $\text{Al}_{50}\text{Ti}_{50}\text{N}$  and 2.  $\text{Al}_{50}\text{Ti}_{50}\text{WN}$ . Adhesion between these two layers affected the wear performance of the coatings, and most probably, it was lower than expected, so the wear of the coatings was low.



Figure 63. High resolution macro-objective images of a)  $Al_{67}Ti_{33}$ , b)  $Al_{64}Cr_{36}$ , c)  $Al_{50}Ti_{50}W-1$ , d)  $Al_{50}Ti_{50}W-2$ , e)  $Al_{67}Ti_{33}-Mo-1$ , f)  $Al_{64}Cr_{36}-Mo-1$ , g)  $Al_{67}Ti_{33}-Mo-2$ , and h)  $Al_{64}Cr_{36}-Mo-2$ .

After 75 holes, cutting tools were used to open another 25 holes. Sample 1 was broken firstly (58 holes), and then sample 2 was broken at 88th hole. Additionally, sample 8 was not tested after 75 holes. The other coated cutting tools were tested. In addition, the superior performance of the coatings developed through optical microscopy and SEM imaging of the inserts was demonstrated in more detail. Figure 64 shows several opened holes of samples. Uncoated High-speed steel cutting tools drilled only 20 holes, while the  $Al_{67}Ti_{33}$  reference material drilled almost 3 times as many holes. Other coatings with W and Mo added have drilled 5 times more holes and were still not broken. The developed coatings increased the metal cutting performance more than 5 times.

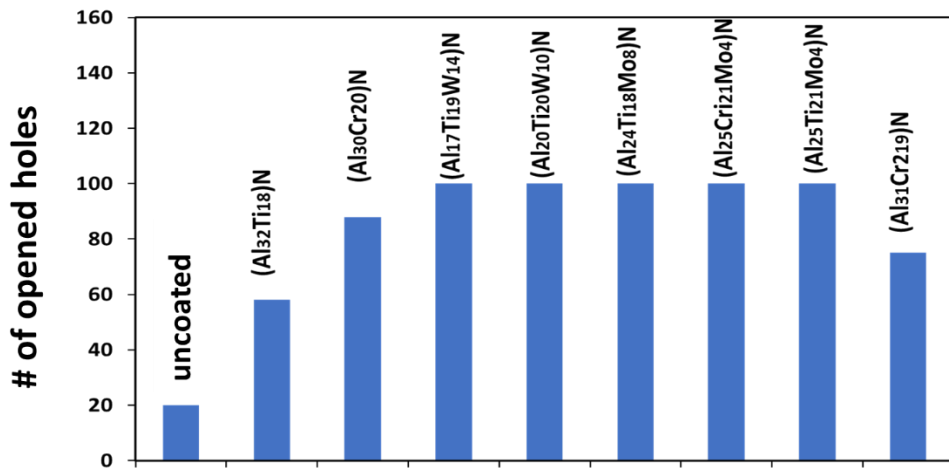


Figure 64. The number of drilled holes before failure for each coating scenario.

To examine in more detail, the details of the test were in Figure 65. In addition to the technical details were given in a table and workpiece material after the test was shown to understand the drilling process and the regularity and structure of the drilled holes. Due to the regularity of the holes, it can be said that there is no vibration

in the vertical machining center and that there is no accumulation or chips on the edges of the holes, the chips that come out during the test were removed.

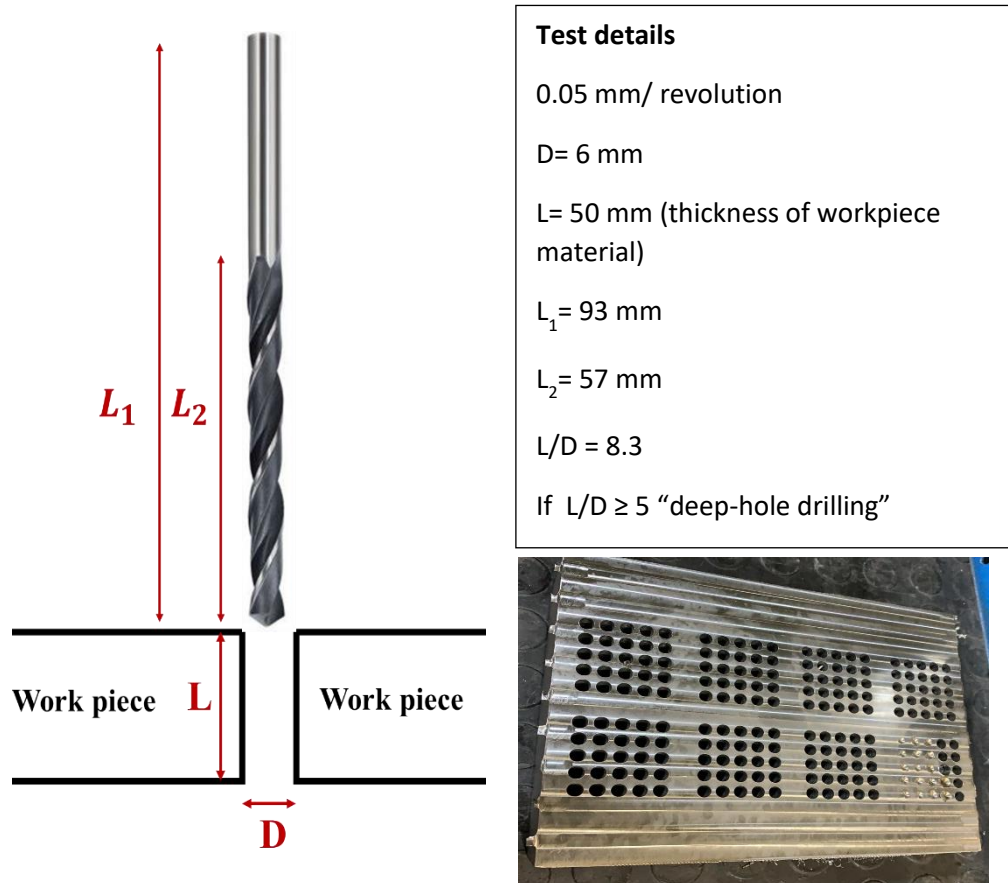


Figure 65. Dimension of cutting tool, test details, and workpiece material after the test.

The surfaces of the drills were examined in detail using SEM. Figure 66 presents the SEM images of the samples and details of the analysis. After opening the holes, the "built-up edge" (BUE) can be seen due to low spindle speed (tools were tested at 1600 rpm). In other words, chips were stuck on the surface of the tools from the workpiece material, and the actual performance of the cutting tools could be affected.

At the same time, line EDS analysis was performed from the head of cutting tools to the end of the blades, and secondary electron (SE) and backscatter electron (BSE) SEM images were taken. Figure 66 shows the SEM images and EDS results of Al<sub>50</sub>Ti<sub>50</sub>-W-2 containing 14% W. Figure 66(a) shows the BSE image of the head of the cutting tool, and in b) the middle part was zoomed. BUE structures were also seen in this part. In c), an EDS result was taken from 185 points along the 2mm line on the blade part. According to the EDS result, Ti, Al, Fe, C, and W (very low) varies from place to place. Since Al and Ti are the main elements in the coating, so they could be taken from the coating, and Fe could come from the substrate material, which was HSS, and C could be taken from the workpiece material. In this case, SEM images and EDS results showed consistency. The last EDS table was generally taken from the head of the cutting tools, and according to the EDS analysis Ti, Al, N, and W are the coating elements, while Fe, Cr, Mn, and C are the elements of the workpiece material. Oxygen shows that there is oxidation in the places where the coating was removed.



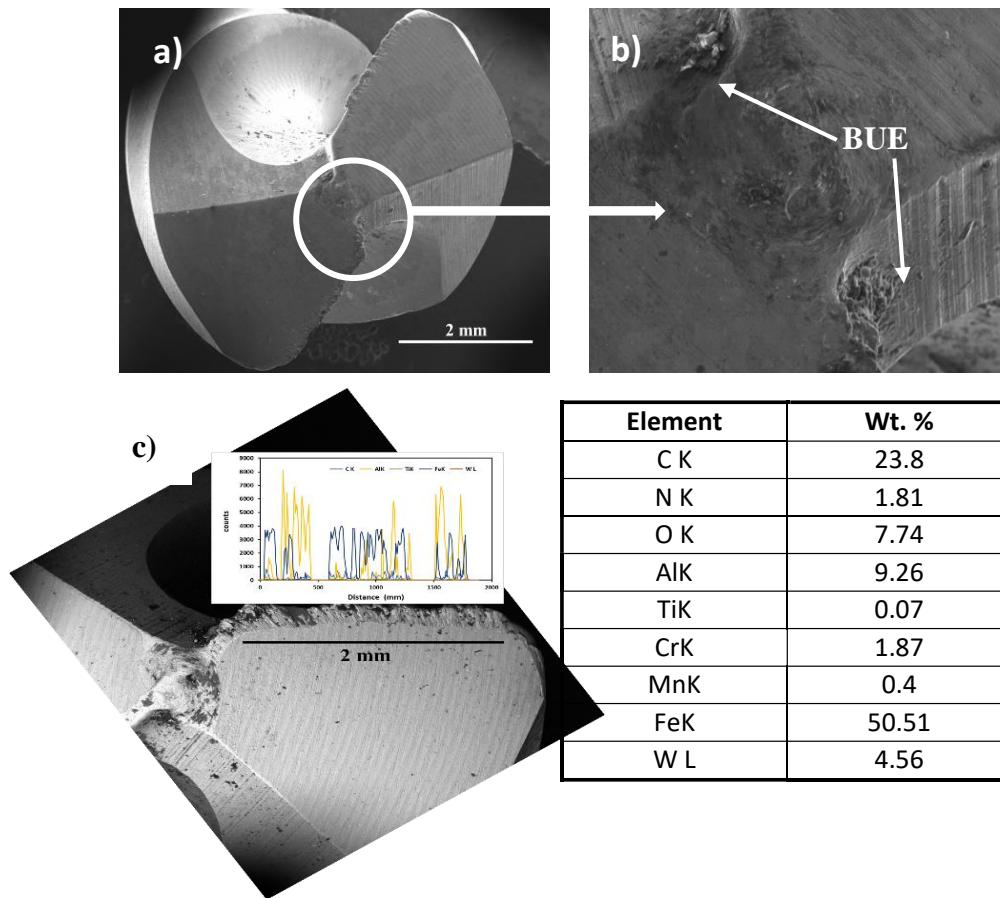


Figure 66. SEM and EDS analyzes of Al<sub>50</sub>Ti<sub>50</sub>-W-2 coated cutting tools after opening of 100 holes.

Figure 67 shows SEM images of the final versions of the other coated cutting tools. In the SEM images in a, b, c, the blade edges were worn, and also fracture could be observed after 100 holes. It can be seen for Al<sub>64</sub>Cr<sub>36</sub>-Mo-1 sample showed the lowest wear 75 holes. However, for 100 holes, the better results belonged to Al<sub>67</sub>Ti<sub>33</sub>-Mo-2 (included high Mo). It can be said that Mo addition improved the wear performance of the hard coatings due to formation of Mo oxides.

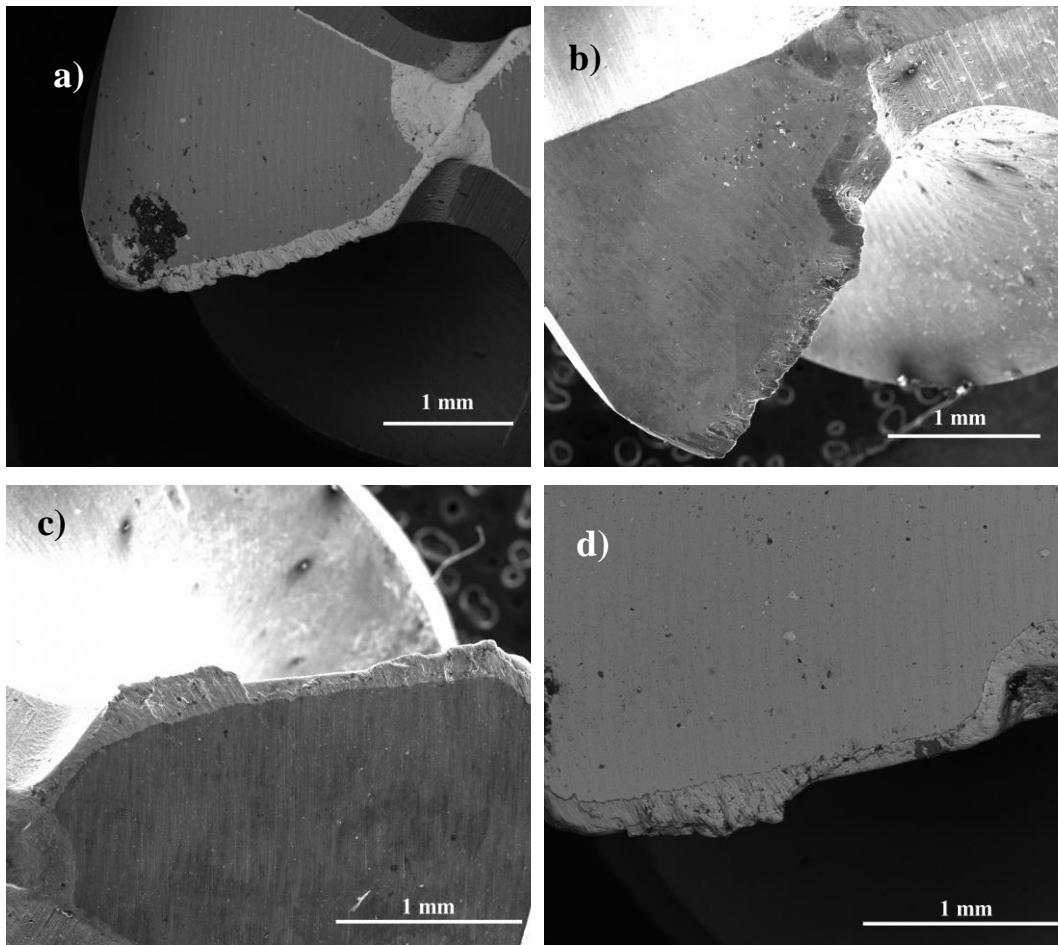


Figure 67. SEM images of coated cutting tools after 100 holes a) Al<sub>67</sub>Ti<sub>33</sub>-Mo-1, b) Al<sub>64</sub>Cr<sub>36</sub>-Mo-1, c) Al<sub>67</sub>Ti<sub>33</sub>-Mo-2, and d) Al<sub>64</sub>Cr<sub>36</sub>-Mo-2.

### 3.3 Conclusions

This study explained the production of hard coatings using cathodic arc evaporation and characterization of these thin films, both structural and mechanical. One of the main research topics is this thesis fracture toughness improvement of refractory element (W or Mo) added hard coatings that produced cathodic arc evaporation.

Nitride formation is an essential parameter of the mechanical properties of hard coating materials. In this study, hard coatings were fully nitrided because of the commercial coating systems. However, it has been found that refractory element added coatings did not have added elements with the desired amount. Although the content of elements was lower, the nanoindentation results of some nitrided samples showed improved mechanical behavior, as expected.

Routine, or commercial coatings, showed expected results such as high hardness and high elastic modulus. Additionally, these coatings' thickness was suitable to prepare micro-cantilevers, and  $\text{Al}_{50}\text{Ti}_{50}$  based coatings can be tested by this new and novel technique. This micro-cantilever bending test is an important part of this study, and it was done successfully, although the manufacturing steps were challenging. Additionally, fracture toughness of  $\text{Al}_{50}\text{Ti}_{50}$  routine coatings were compared as a result of nanoindentation and cantilever bending test. These two results were compatible with each other.

10-14 at.% W alloyed  $\text{Al}_{50}\text{Ti}_{50}$  based hard coating showed consistent results with the DFT studies, which are theoretical ones.. 4-8 at.% Mo alloyed  $\text{Al}_{67}\text{Ti}_{33}$  based hard coatings showed better results than  $\text{Al}_{50}\text{Ti}_{50}$  based coatings. Both the hardness and elastic modulus of these coatings were improved as the content of Mo increases. Interestingly,  $\text{Al}_{50}\text{Cr}_{50}$  based material showed reversed results than the expected ones. Mo addition did not improve hardness and elastic modulus.

The wear performance of all nonroutine coatings was analyzed using the ball-on disc test and drilling test. 2-layered 14 at.% of W added  $\text{Al}_{50}\text{Ti}_{50}$  based nitride showed the worst results due to worst adhesion between two layers.



## CHAPTER 4

### CONCLUSIONS AND FUTURE WORK

In this thesis, important findings were obtained to better understand the mechanical properties of both laboratory scale and industrial scale hard coatings with an emphasis on the effect of W and Mo. Listed below are the key results.

1. There have been difficulties in the laboratory-scale production of W-added nitride coatings by magnetron sputtering. In industrial-scale cathodic arc coatings, production difficulties were more easily overcome.
2. With W and Mo added to the structure, the material's microstructure has not changed significantly, and the refractory element atoms have mostly got dissolved in the crystal structure.
3. On the other hand, the addition of refractory elements significantly changed the mechanical properties. As a result of W additions, fracture toughness increases up to 25 times compared to conventional coatings. On the other hand, as the Mo element was added to the structure, the hardness values did not change, while the modulus of elasticity decreased. Thus, a coating with a superior H/E ratio was obtained, promising in terms of wear resistance performance.
4. A recently developed microcantilever bending test to measure the fracture toughness of thin films was successfully applied.
5. Fracture toughness results using nanoindentation method and micro-cantilever bending were compared for Al50Ti50 standard hard coatings, and the results were found to be mostly in agreement.
6. The evaluations of the developed coatings through drilling and wear experiments provided preliminary evidence that W and Mo added coatings provide a much longer lifetime than the standard nitride coatings.

In this thesis, the production of refractory element added-hard coatings was challenging due to the high evaporation current and deposition conditions. As a result, the Mo and W content was lower than expected. Future studies should focus on the utilization of cathodic arc evaporation systems with higher capacity to more clearly assess the effect of high Mo and W content on the mechanical properties.

An important aspect of the thesis was fracture toughness measurements through two different techniques. Among these, the nanoindentation-based approach is easier to apply compared to the microcantilever bending method. However, some of the associated data had inconsistencies, which might be due to some additional cracking at the interface that is not visible at first glance. Furthermore, such nanoindentation-based fracture toughness measurements are directly affected by film stress and surface roughness. The results showed that care should be taken when evaluating the outcomes of such measurements. On the other hand, micro-cantilever bending tests were much more difficult to perform. It took much more time and effort to produce the microcantilevers. In addition, maintaining dimensional consistency has been challenging. There were also problems such as W added-ALTiN coatings being dissolved in the KOH. The overall outcome of these challenges was a limited number of specimens for each case, which reduced the statistical significance of the data. Future work in this field should focus on the fabrication of microcantilevers in series through photolithography, in ways analogous to MEMS and atomic force microscopy probe production techniques. This way, it will be possible to produce hundreds of cantilevers at once, which will enable more consistent and statistically significant results.

The findings of this thesis have been directly related to the activities of a TÜBİTAK 1001 project (grant #118M201), and the future goal after the completion of this project will be higher TRL activities towards the commercialization of these coatings.

## REFERENCES

- Abboud, M. (2018). *Micromechanical characterization of metallic glass-Crystalline nanocomposite coatings*. <https://open.metu.edu.tr/handle/11511/27942>
- Allsopp, D. N., & Hutchings, I. M. (2001). Micro-scale abrasion and scratch response of PVD coatings at elevated temperatures. *Wear*, *251*(1), 1308–1314. [https://doi.org/10.1016/S0043-1648\(01\)00755-4](https://doi.org/10.1016/S0043-1648(01)00755-4)
- Ast, J., Ghidelli, M., Durst, K., Göken, M., Sebastiani, M., & Korsunsky, A. M. (2019). A review of experimental approaches to fracture toughness evaluation at the micro-scale. *Materials & Design*, *173*, 107762. <https://doi.org/10.1016/j.matdes.2019.107762>
- Aydın, M., Gavas, M., Yaşar, M., & Altunpak, Y. (2012). *Üretim yöntemleri ve imalat teknolojileri*. Seçkin.
- Bobzin, K. (2017). High-performance coatings for cutting tools. *CIRP Journal of Manufacturing Science and Technology*, *18*, 1–9. <https://doi.org/10.1016/j.cirpj.2016.11.004>
- Bobzin, K., Lugscheider, E., Nickel, R., Bağcivan, N., & Krämer, A. (2007). Wear behavior of Cr<sub>1-x</sub>Al<sub>x</sub>N PVD-coatings in dry running conditions. *Wear*, *263*(7), 1274–1280. <https://doi.org/10.1016/j.wear.2007.01.118>
- Bouzakis, K.-D., Michailidis, N., Skordaris, G., Bouzakis, E., Biermann, D., & M'Saoubi, R. (2012a). Cutting with coated tools: Coating technologies, characterization methods and performance optimization. *CIRP Annals*, *61*(2), 703–723. <https://doi.org/10.1016/j.cirp.2012.05.006>
- Bouzakis, K.-D., Michailidis, N., Skordaris, G., Bouzakis, E., Biermann, D., & M'Saoubi, R. (2012b). Cutting with coated tools: Coating technologies, characterization methods and performance optimization. *CIRP Annals*, *61*(2), 703–723. <https://doi.org/10.1016/j.cirp.2012.05.006>

- Brabazon, D., & Raffer, A. (2015). Chapter 3-Advanced characterization techniques for nanostructures. In W. Ahmed & M. J. Jackson (Eds.), *Emerging Nanotechnologies for Manufacturing (Second Edition)* (pp. 53–85). William Andrew Publishing. <https://doi.org/10.1016/B978-0-323-28990-0.00003-8>
- Chauhan, K. V., & Rawal, S. K. (2014). A Review Paper on Tribological and Mechanical Properties of Ternary Nitride based Coatings. *Procedia Technology*, *14*, 430–437. <https://doi.org/10.1016/j.protcy.2014.08.055>
- Chawla, V. (2013). Microstructural Characteristics and Mechanical Properties of Nanostructured and Conventional TiAlN and AlCrN Coatings on ASTM-SA210 Grade A-1 Boiler Steel. *ISRN Corrosion*, *2013*. <https://doi.org/10.1155/2013/231035>
- Chen, L., Holec, D., Du, Y., & Mayrhofer, P. H. (2011). Influence of Zr on structure, mechanical and thermal properties of Ti–Al–N. *Thin Solid Films*, *519*(16), 5503–5510. <https://doi.org/10.1016/j.tsf.2011.03.139>
- Chen, S., Liu, L., & Wang, T. (2005). Investigation of the mechanical properties of thin films by nanoindentation, considering the effects of thickness and different coating–substrate combinations. *Surface and Coatings Technology*, *191*(1), 25–32. <https://doi.org/10.1016/j.surfcoat.2004.03.037>
- Cremer, R., & Neuschütz, D. (2001). A combinatorial approach to the optimization of metastable multicomponent hard coatings. *Surface and Coatings Technology*, *146–147*, 229–236. [https://doi.org/10.1016/S0257-8972\(01\)01472-4](https://doi.org/10.1016/S0257-8972(01)01472-4)
- Deng, Y., Chen, W., Li, B., Wang, C., Kuang, T., & Li, Y. (2020). Physical vapor deposition technology for coated cutting tools: A review. *Ceramics International*, *46*(11, Part B), 18373–18390. <https://doi.org/10.1016/j.ceramint.2020.04.168>
- Dolinšek, S., Šuštaršič, B., & Kopač, J. (2001). Wear mechanisms of cutting tools in high-speed cutting processes. *Wear*, *250*(1), 349–356. [https://doi.org/10.1016/S0043-1648\(01\)00620-2](https://doi.org/10.1016/S0043-1648(01)00620-2)



- Fan, Q.-X., Zhang, J.-J., Wu, Z.-H., Liu, Y.-M., Zhang, T., Yan, B., & Wang, T.-G. (2017). Influence of Al Content on the Microstructure and Properties of the CrAlN Coatings Deposited by Arc Ion Plating. *Acta Metallurgica Sinica (English Letters)*, *30*(12), 1221–1230. <https://doi.org/10.1007/s40195-017-0656-6>
- Fischer-Cripps, A. C. (2002). Nanoindentation Testing. In A. C. Fischer-Cripps (Ed.), *Nanoindentation* (pp. 20–35). Springer. [https://doi.org/10.1007/978-0-387-22462-6\\_2](https://doi.org/10.1007/978-0-387-22462-6_2)
- Flink, A., Andersson, J. M., Alling, B., Daniel, R., Sjöln, J., Karlsson, L., & Hultman, L. (2008). Structure and thermal stability of arc evaporated (Ti<sub>0.33</sub>Al<sub>0.67</sub>)<sub>1-x</sub>Si<sub>x</sub>N thin films. *Thin Solid Films*, *517*(2), 714–721. <https://doi.org/10.1016/j.tsf.2008.08.126>
- Gamonpilas, C., & Busso, E. P. (2004). On the effect of substrate properties on the indentation behavior of coated systems. *Materials Science and Engineering: A*, *380*(1–2), 52–61. <https://doi.org/10.1016/j.msea.2004.04.038>
- García-González, L., Garnica-Romo, M. G., Hernández-Torres, J., & Espinoza-Beltrán, F. J. (2007). A study of TiAlN coatings prepared by rf co-sputtering. *Brazilian Journal of Chemical Engineering*, *24*, 249–257. <https://doi.org/10.1590/S0104-66322007000200009>
- Glatz, S. A., Bolvardi, H., Kolozsvári, S., Koller, C. M., Riedl, H., & Mayrhofer, P. H. (2017). Arc evaporated W-alloyed Ti-Al-N coatings for improved thermal stability, mechanical and tribological properties. *Surface and Coatings Technology*, *332*, 275–282. <https://doi.org/10.1016/j.surfcoat.2017.05.097>
- Glatz, S. A., Koller, C. M., Bolvardi, H., Kolozsvári, S., Riedl, H., & Mayrhofer, P. H. (2017). Influence of Mo on the structure and the tribomechanical properties of arc evaporated Ti-Al-N. *Surface and Coatings Technology*, *311*, 330–336. <https://doi.org/10.1016/j.surfcoat.2017.01.001>
- Goldstein, J., Newbury, D. E., Echlin, P., Joy, D. C., Jr, A. D. R., Lyman, C. E., Fiori, C., & Lifshin, E. (1992). *Scanning Electron Microscopy and X-Ray Microanalysis: A Text for Biologists, Materials Scientists, and Geologists* (2nd ed.). Springer US. <https://doi.org/10.1007/978-1-4613-0491-3>

- Greczynski, G., Lu, J., Tengstrand, O., Petrov, I., Greene, J. E., & Hultman, L. (2016). Nitrogen-doped bcc-Cr films: Combining ceramic hardness with metallic toughness and conductivity. *Scripta Materialia*, *122*, 40–44. <https://doi.org/10.1016/j.scriptamat.2016.05.011>
- Hagarová, M., Jakubéczyová, D., Fides, M., Vojtko, M., & Savková, J. (2018). *Pin-on-Disc Study of Tribological Performance of PVD Coatings*. <https://doi.org/10.4236/JSEMAT.2018.81002>
- Hahn, H., Mondal, P., & Padmanabhan, K. A. (1997). Plastic deformation of nanocrystalline materials. *Nanostructured Materials*, *9*(1), 603–606. [https://doi.org/10.1016/S0965-9773\(97\)00135-9](https://doi.org/10.1016/S0965-9773(97)00135-9)
- Hahn, R., Bartosik, M., Soler, R., Kirchlechner, C., Dehm, G., & Mayrhofer, P. H. (2016). Superlattice effect for enhanced fracture toughness of hard coatings. *Scripta Materialia*, *124*, 67–70. <https://doi.org/10.1016/j.scriptamat.2016.06.030>
- Hörling, A., Hultman, L., Odén, M., Sjöln, J., & Karlsson, L. (2005). Mechanical properties and machining performance of Ti<sub>1-x</sub>Al<sub>x</sub>N-coated cutting tools. *Surface and Coatings Technology*, *191*(2–3), 384–392. <https://doi.org/10.1016/j.surfcoat.2004.04.056>
- Ingham, B., & Toney, M. F. (2014). X-ray diffraction for characterizing metallic films. In *Metallic Films for Electronic, Optical and Magnetic Applications* (pp. 3–38). Elsevier. <https://doi.org/10.1533/9780857096296.1.3>
- Jaya, B. N., Kirchlechner, C., & Dehm, G. (2015). Can microscale fracture tests provide reliable fracture toughness values? A case study in silicon. *Journal of Materials Research*, *30*(5), 686–698. <https://doi.org/10.1557/jmr.2015.2>
- Joo, Y., Shi-Hong, Z., Yoon, jae-hong, & Tong-Yul, C. (2009). Optimization of the Adhesion Strength of Arc Ion Plating TiAlN Films by the Taguchi Method. *Materials*, *2*. <https://doi.org/10.3390/ma2020699>

- Kataria, S., Srivastava, S. K., Kumar, P., Srinivas, G., Siju, Khan, J., Rao, D. V. S., & Barshilia, H. C. (2012). Nanocrystalline TiN coatings with improved toughness deposited by pulsing the nitrogen flow rate. *Surface and Coatings Technology*, 206(19), 4279–4286. <https://doi.org/10.1016/j.surfcoat.2012.04.040>
- Kelly, P. J., & Arnell, R. D. (2000). Magnetron sputtering: A review of recent developments and applications. *Vacuum*, 56(3), 159–172. [https://doi.org/10.1016/S0042-207X\(99\)00189-X](https://doi.org/10.1016/S0042-207X(99)00189-X)
- Kindlund, H., Sangiovanni, D. G., Martínez-de-Olcoz, L., Lu, J., Jensen, J., Birch, J., Petrov, I., Greene, J. E., Chirita, V., & Hultman, L. (2013). Toughness enhancement in hard ceramic thin films by alloy design. *APL Materials*, 1(4), 042104. <https://doi.org/10.1063/1.4822440>
- Kılınc, B., Cegil, O., Sen, S., & Sen, U. (2014). Wear Behavior of TiAlN and CrAlN Coatings Deposited by TRD Process on AISI D2 Steel. *Acta Physica Polonica A*, 125(2), 362–364. <https://doi.org/10.12693/APhysPolA.125.362>
- Knotek, O., & Leyendecker, T. (1987). On the structure of (Ti, Al)N-PVD coatings. *Journal of Solid State Chemistry*, 70(2), 318–322. [https://doi.org/10.1016/0022-4596\(87\)90071-5](https://doi.org/10.1016/0022-4596(87)90071-5)
- Langford, J. I., & Wilson, A. J. C. (n.d.). *Scherrer after Sixty Years: A Survey and Some New Results in the Determination of Crystallite Size*. 12.
- Lawn, B. R., Evans, A. G., & Marshall, D. B. (1980). Elastic/Plastic Indentation Damage in Ceramics: The Median/Radial Crack System. *Journal of the American Ceramic Society*, 63(9–10), 574–581. <https://doi.org/10.1111/j.1151-2916.1980.tb10768.x>
- Leyland, A., & Matthews, A. (2000). On the significance of the H/E ratio in wear control: A nanocomposite coating approach to optimized tribological behaviour. *Wear*, 246(1), 1–11. [https://doi.org/10.1016/S0043-1648\(00\)00488-9](https://doi.org/10.1016/S0043-1648(00)00488-9)

- Leyland, A., & Matthews, A. (2004). Design criteria for wear-resistant nanostructured and glassy-metal coatings. *Surface and Coatings Technology*, 177–178, 317–324. <https://doi.org/10.1016/j.surfcoat.2003.09.011>
- Maio, D. D., & Roberts, S. G. (2005). Measuring fracture toughness of coatings using focused-ion-beam-machined microbeams. *Journal of Materials Research*, 20(2), 299–302. <https://doi.org/10.1557/JMR.2005.0048>
- Mehran, Q. M., Fazal, M. A., Bushroa, A. R., & Rubaiee, S. (2018). A Critical Review on Physical Vapor Deposition Coatings Applied on Different Engine Components. *Critical Reviews in Solid State and Materials Sciences*, 43(2), 158–175. <https://doi.org/10.1080/10408436.2017.1320648>
- Mo, J. L., & Zhu, M. H. (2008). Sliding tribological behavior of AlCrN coating. *Tribology International*, 41(12), 1161–1168. <https://doi.org/10.1016/j.triboint.2008.02.007>
- Music, D., Geyer, R. W., & Schneider, J. M. (2016). Recent progress and new directions in density functional theory based design of hard coatings. *Surface and Coatings Technology*, 286, 178–190. <https://doi.org/10.1016/j.surfcoat.2015.12.021>
- Musil, J. (2012). Hard nanocomposite coatings: Thermal stability, oxidation resistance and toughness. *Surface and Coatings Technology*, 207, 50–65. <https://doi.org/10.1016/j.surfcoat.2012.05.073>
- Nanomechanical Instruments for SEM/TEM*. (n.d.). Retrieved July 2, 2021, from <https://www.bruker.com/en/products-and-solutions/test-and-measurement/nanomechanical-instruments-for-sem-tem.html>
- Oliver, W. C., & Pharr, G. M. (1992). An improved technique for determining hardness and elastic modulus using load and displacement sensing indentation experiments. *Journal of Materials Research*, 7(6), 1564–1583. <https://doi.org/10.1557/JMR.1992.1564>
- Pettifor, D. (1992). *Theoretical predictions of structure and related properties of intermetallics*. <https://doi.org/10.1179/MST.1992.8.4.345>

- Pugh, S. F. (1954). XCII. Relations between the elastic moduli and the plastic properties of polycrystalline pure metals. *The London, Edinburgh, and Dublin Philosophical Magazine and Journal of Science*, 45(367), 823–843. <https://doi.org/10.1080/14786440808520496>
- Raider, S. I., Flitsch, R., Aboaf, J. A., & Pliskin, W. A. (1976). Surface Oxidation of Silicon Nitride Films. *Journal of The Electrochemical Society*, 123(4), 560. <https://doi.org/10.1149/1.2132877>
- Rao, A. V. N., Swarnalatha, V., & Pal, P. (2017). Etching characteristics of Si{110} in 20 wt% KOH with addition of hydroxylamine for the fabrication of bulk micromachined MEMS. *Micro and Nano Systems Letters*, 5(1), 23. <https://doi.org/10.1186/s40486-017-0057-7>
- Richard, C., Manivasagam, G., & Chen, Y.-M. (2015). *Chapter 8: Measurement of Wear and Friction Resistance of Bulk and Coated Materials*. <https://doi.org/10.1201/b19177-9>
- Riedl, A., Daniel, R., Stefenelli, M., Schöberl, T., Kolednik, O., Mitterer, C., & Keckes, J. (2012). A novel approach for determining fracture toughness of hard coatings on the micrometer scale. *Scripta Materialia*, 67(7), 708–711. <https://doi.org/10.1016/j.scriptamat.2012.06.034>
- Rieth, M. (2003). *Nano-Engineering in Science and Technology: An Introduction to the World of Nano-Design*. WORLD SCIENTIFIC. <https://doi.org/10.1142/5026>
- Rother, B., & Dietrich, D. A. (1994). Differential load feed analysis: An energy-related alternative to the interpretation of hardness indentation measurements. *Physica Status Solidi (a)*, 142(2), 389–407. <https://doi.org/10.1002/pssa.2211420212>
- Rother, B., & Kazmanli, K. M. (1998). Characterization of hard coatings by depth-sensing indentation measurements: Indenter effects. *Surface and Coatings Technology*, 99(3), 311–318. [https://doi.org/10.1016/S0257-8972\(97\)00685-3](https://doi.org/10.1016/S0257-8972(97)00685-3)

- Sanchette, F., Ducros, C., Schmitt, T., Steyer, P., & Billard, A. (2011). Nanostructured hard coatings deposited by cathodic arc deposition: From concepts to applications. *Surface and Coatings Technology*, 205(23–24), 5444–5453. <https://doi.org/10.1016/j.surfcoat.2011.06.015>
- Sangiovanni, D. G., Chirita, V., & Hultman, L. (2012). Toughness enhancement in TiAlN-based quaternary alloys. *Thin Solid Films*, 520(11), 4080–4088. <https://doi.org/10.1016/j.tsf.2012.01.030>
- Sebastiani, M., Johanns, K. E., Herbert, E. G., & Pharr, G. M. (2015). Measurement of fracture toughness by nanoindentation methods: Recent advances and future challenges. *Current Opinion in Solid State and Materials Science*, 19(6), 324–333. <https://doi.org/10.1016/j.cossms.2015.04.003>
- Seidl, W. M., Bartosik, M., Kolozsvári, S., Bolvardi, H., & Mayrhofer, P. H. (2018). Influence of Ta on the fracture toughness of arc evaporated Ti-Al-N. *Vacuum*, 150, 24–28. <https://doi.org/10.1016/j.vacuum.2018.01.028>
- Sousa, V. F. C., Da Silva, F. J. G., Pinto, G. F., Baptista, A., & Alexandre, R. (2021). Characteristics and Wear Mechanisms of TiAlN-Based Coatings for Machining Applications: A Comprehensive Review. *Metals*, 11(2), 260. <https://doi.org/10.3390/met11020260>
- Sveen, S., Andersson, J. M., M'Saoubi, R., & Olsson, M. (2013). Scratch adhesion characteristics of PVD TiAlN deposited on high speed steel, cemented carbide and PCBN substrates. *Wear*, 308(1), 133–141. <https://doi.org/10.1016/j.wear.2013.08.025>
- Tang, W., Liu, R., Lu, X., Zhang, S., & Liu, S. (2018). Tribological Behavior of Lamellar Molybdenum Trioxide as a Lubricant Additive. *Materials*, 11(12), 2427. <https://doi.org/10.3390/ma11122427>
- tribonet. (2019, February 24). *Pin on Disk Test | Tribology | Tribonet*. <https://www.tribonet.org/wiki/pin-on-disk-test/>

- Tsui, T. Y., Vlassak, J., & Nix, W. D. (1999). Indentation plastic displacement field: Part II. The case of hard films on soft substrates. *Journal of Materials Research, 14*(6), 2204–2209. <https://doi.org/10.1557/JMR.1999.0296>
- Wei, R., Vajo, J. J., Matossian, J. N., & Gardos, M. N. (2002). Aspects of plasma-enhanced magnetron-sputtered deposition of hard coatings on cutting tools. *Surface and Coatings Technology, 158–159*, 465–472. [https://doi.org/10.1016/S0257-8972\(02\)00289-X](https://doi.org/10.1016/S0257-8972(02)00289-X)
- Xu, Y. X., Chen, L., Yang, B., Peng, Y. B., Du, Y., Feng, J. C., & Pei, F. (2013). Effect of CrN addition on the structure, mechanical and thermal properties of Ti-Al-N coating. *Surface and Coatings Technology, 235*, 506–512. <https://doi.org/10.1016/j.surfcoat.2013.08.010>
- Xu, Y. X., Hu, C., Chen, L., Pei, F., & Du, Y. (2018). Effect of V-addition on the thermal stability and oxidation resistance of CrAlN coatings. *Ceramics International, 44*(6), 7013–7019. <https://doi.org/10.1016/j.ceramint.2018.01.135>
- Xu, Y. X., Riedl, H., Holec, D., Chen, L., Du, Y., & Mayrhofer, P. H. (2017). Thermal stability and oxidation resistance of sputtered TiAlCrN hard coatings. *Surface and Coatings Technology, 324*, 48–56. <https://doi.org/10.1016/j.surfcoat.2017.05.053>
- Yang, W., Fu, G., & Li, C.-Q. (2017). Elastic Fracture Toughness of Ductile Materials. *Journal of Engineering Mechanics, 143*(9), 04017111. [https://doi.org/10.1061/\(ASCE\)EM.1943-7889.0001321](https://doi.org/10.1061/(ASCE)EM.1943-7889.0001321)
- Yousaf, M. I., Pelenovich, V. O., Yang, B., Liu, C. S., & Fu, D. J. (2015). Effect of bilayer period on structural and mechanical properties of nanocomposite TiAlN/MoN multilayer films synthesized by cathodic arc ion-plating. *Surface and Coatings Technology, 282*, 94–102. <https://doi.org/10.1016/j.surfcoat.2015.10.018>
- Zawada-Michałowska, M., Pieśko, P., & Józwick, J. (2020). Tribological Aspects of Cutting Tool Wear during the Turning of Stainless Steels. *Materials, 13*(1), 123. <https://doi.org/10.3390/ma13010123>





## CURRICULUM VITAE

### PERSONAL INFORMATION

Surname, Name: Kaygusuz, Burçin  
Nationality: Turkish (TC)  
Date and Place of Birth: 14 December 1987, Ankara  
Marital Status: Single  
Phone: 0 555 588 99 57  
email: burcin.kaygusuz@metu.edu.tr , kaygusuz.burcin@gmail.com

### EDUCATION

Degree	Institution	Year of Graduation
MS	METU Metallurgical and Materials Engineering	2016
BS	Gazi University Chemical Engineering	2013
High School	Çankaya Anadolu High School, Ankara	2006

### WORK EXPERIENCE

Year	Place	Enrollment
2017-2021	METU Dept. of Mechanical Eng.- Nanomechanics Lab.	Tübitak 1001 Project Assistant
2014-2016	METU Dept. of Met. And Mat. Eng.- Energy Storage and Batteries Lab.	Tübitak 2210-C Project Assistant
2012 July	TUSAŞ, Process Control Lab.	Intern Eng. Student
2011 July	TUSAŞ, Dep. Of Material & Process	Intern Eng. Student

### FOREIGN LANGUAGES

Advanced English, Preliminary German

### PUBLICATIONS

1. **Kaygusuz B.**, Motallabzadeh A., Karadayı Ö.D., Kazmanlı M.K., Özerinç S., Microscale Fracture Toughness Testing on Hard Coatings, 20th International Metallurgy & Materials Congress 2021.

2. Özerinç S., **Kaygusuz B.**, Kaş M., Motallebzadeh A., Nesli Ş., Duygulu Ö., Yılmaz O., (2021) Micromechanical characterization of additively manufactured Ti-6Al-4V parts produced by electron beam melting, J. of the Minerals, Metals and Materials Society. <https://doi.org/10.1007/s11837-021-04804-w>.
3. Okuyucu C., **Kaygusuz B.**, Işıksaçan C., Meydanoğlu O., Motallabzadeh A., Özerinç S., Kalay Y.E., (2021) Al-Sm Alloys Under Far-From-Equilibrium Conditions. In: Perander L. (eds) Light Metals. The Minerals, Metals & Materials Series. Springer, Cham. [https://doi.org/10.1007/978-3-030-65396-5\\_13](https://doi.org/10.1007/978-3-030-65396-5_13).
4. **Kaygusuz B.**, Özerinç S., (2019) Improving the ductility of polylactic acid parts produced by fused deposition modeling through polyhydroxyalkanoate additions, J. of Applied Polymer Science. <https://doi.org/10.1002/app.48154>
5. **Kaygusuz B.**, Özerinç S., (2018) 3 boyutlu yazıcı ile üretilen PLA bazlı yapıların mekanik özelliklerinin incelenmesi, Matim.
6. **Kaygusuz B.**, Nigar B., Ünlüsoy L., Çöker D., Özerinç S., Mechanical and Microstructural Evolution of Solid Graphite Rocket Nozzle Throats in Extreme Temperature and Pressure Conditions, 19<sup>th</sup> International Metallurgy & Materials Congress 2018.
7. **Kaygusuz B.**, Özerinç S., Mechanical Properties of PLA/PHA Blends for Fused Deposition Modelling Applications, 1<sup>st</sup> International Conference on Advances in Mechanical and Mechatronics Engineering 2018.